7. SITE 1068[1]

Shipboard Scientific Party[2]

HOLE 1068A

Position: 40° 40.955'N, 11° 36.720'W

Start hole: 1815 hr, 10 May 1997

End hole: 0530 hr, 22 May 1997

Time on hole: 275.25 hr (11.5 days)

Seafloor (drill pipe measurement from rig floor, mbrf): 5055.0

Total depth (drill pipe measurement from rig floor, mbrf): 6010.8

Distance between rig floor and sea level (m): 11.1

Water depth (drill pipe measurement from sea level, m): 5043.9

Penetration (mbsf): 955.8

Coring totals:

Type: RCB; Number: 29; Cored: 244.5 m; Recovered: 180.59 m; Average recovery: 73.9%

Sedimentary sequence:

Unit IIB: (711.3–733.55 mbsf): calcareous claystone, claystone, and calcareous siltstone (middle to early Eocene)

Unit IIC: (733.55–853.02 mbsf): claystone, calcareous claystone, nannofossil chalk, and calcareous sandy siltstone (early Eocene to Maastrichtian)

Acoustic basement:

Unit IVA: (853.02–865.6 mbsf): matrix-supported breccia with calcareous matrix; clasts of weakly to strongly foliated amphibolite, meta-anorthosites, and meta-gabbro; Early Cretaceous nannofossils in calcareous matrix

Unit IVB: (865.6–884.9 mbsf): clast-supported breccia with matrix of sand- and silt-sized grains of clast material encased in calcite and Fe-oxyhydroxide; clasts are dominantly amphibolite; matrix is barren of nannofossils

Unit IVC: (884.9–893.13 mbsf): cataclastic breccia with matrix of calcite, chlorite, albite, and Fe-oxyhydroxide; clasts of meta-anorthosite and metagabbro; matrix is barren of nannofossils

Crystalline basement:

Unit 1: (893.13–955.8 mbsf): serpentinite and serpentinized plagioclase peridotite

Principal results: Site 1068 lies near the southern edge of the Iberia Abyssal Plain. The primary objective at this site was to sample the crystalline basement just to the west of where a strong east-dipping intrabasement seismic reflector, interpreted as a major synrift tectonic contact, intersects the top of the acoustic basement (i.e., to sample the lower plate of this contact). The site, located on the west flank of the same north-south–trending basement high as Sites 1067 and 900 (600 and 1400 m to the east, respectively), was chosen after technical problems prevented us from reaching the reflector and underlying terrane at Site 1067.

The principal achievement at this site was finding mantle rocks. These rocks lie beneath the intrabasement reflector that is overlain by metagabbros, amphibolites, and intrusive tonalite gneisses and meta-anorthosites that were sampled at Sites 1067 and 900. Because serpentinized peridotites were also cored directly under the sediments at Site 897, located 80 km further west, this result indicates that mantle rocks occur, at least as isolated outcrops in basement, over a broad region in the ocean/continent transition (OCT).

Two lithostratigraphic subunits are recognized in the 139-m-thick sedimentary succession cored in Hole 1068A, both of which show gently inclined bedding dips (~5°). Subunit IIB consists of upward-darkening sequences, 3–15 cm thick. These consist of a lower turbiditic calcareous sandy siltstone and calcareous claystone capped by a hemipelagic claystone. In Subunit IIC the upward-darkening sequences are up to 45 cm thick and are largely dominated by nannofossil claystones and nannofossil chalks. Occasional laminated calcareous sandstones up to 15 cm thick occur within otherwise continuous claystone intervals, and are interpreted as lag deposits resulting from winnowing by contour currents.

Biostratigraphic evidence indicates that deposition of the two lithostratigraphic subunits at Site 1068 was essentially continuous and that their age ranges from middle Eocene to Maastrichtian. Calcareous microfossils are common and generally well preserved at the tops of both the Eocene and Paleocene sections, but become less so toward the bottoms of those intervals, which were deposited as microfossiliferous turbidites emplaced below the carbonate compensation depth (CCD). Planktonic foraminifers are variable in preservation and abundance. They indicate an early Eocene (Zone P9) to late Paleocene (Zone P4) age. All Cenozoic Okada and Bukry (1980) calcareous nannofossil zones are present from Subzone CP12a (Zone NP14 of Martini, 1971) to CP1a (NP1a). An intact Cretaceous/Tertiary (K/T) boundary was not recovered, as it has apparently been eroded away completely and/or thoroughly mixed within the bioturbated turbidites. *Micula prinsii* and *M. murus* in Section 173-1068A-14R-1 help to delineate the K/T transition there.

The 42-m-thick sedimentary breccias drilled at Site 1068 are assigned to lithostratigraphic Unit IV to conform with the lithostratigraphic scheme devised during Leg 149. Subunit IVA (<14 m) consists of matrix-supported breccias, in which a few Tithonian–Lower Cretaceous calpionellid limestone clasts occur, and in which the matrix consists of carbonate mudstone yielding Early Cretaceous (Berriasian to early Aptian) nannofossils. It is interpreted to have been deposited by at least three separate debris flows. Subunit IVB (18.8 m) consists entirely of clast-supported breccias. Subunit IVC (8.9 m) consists of clasts showing jigsaw brecciation set in a cataclasite matrix that also contains sand- and silt-sized grains of clast material. These weakly to undeformed sedimentary breccias were probably deposited as talus deposits or rock falls at the foot of a fault scarp. An unconformity may separate Subunits IVA and IVB. The dominant clast type throughout consists of angular fragments of weakly to strongly foliated amphibolites, meta-anorthosites, and meta-gabbros; the clasts are set in a calcitic matrix. These rocks experienced a retrograde metamorphic evolution and an intense deformation under conditions ranging from upper amphibolite facies to greenschist facies comparable to those of the Site 1067 amphibolites and Leg 149 Site 900 metagabbros. Preliminary geochemical data reveal a tholeiitic compositional range that is intermediate between these two types of rocks. Towards the base of Unit IV, the matrix is more chloritic and the breccias are increasingly overprinted by brittle deformation, cataclasis, and hydrothermal alteration, and rest on a tectonized contact. There is strong circumstantial evidence at this depth to suggest that the hole penetrated the seaward-dipping normal fault that bounds the basement high.

[1]Whitmarsh, R.B., Beslier, M.-O., Wallace, P.J., et al., 1998. *Proc. ODP, Init. Repts.*, 173: College Station, TX (Ocean Drilling Program).

[2]Shipboard Scientific Party is given in the list preceding the Table of Contents.

Pervasively serpentinized upper mantle peridotites (60 m recovered) constitute Unit 1, the deepest acoustic basement unit. The pervasive serpentinization of the rocks (up to 99%) has left behind only relicts of spinels rimmed by chlorite probably derived from plagioclase, and locally from clinopyroxene, which suggests that these rocks are derived from plagioclase-bearing lherzolites comparable to those cored at Site 897 (Leg 149). Headspace gas samples from the serpentinite and serpentinite breccia contain as much as 6,000 ppm methane and 1.2 ppm ethane, with no other detectable hydrocarbons. Such anomalously high methane values may be a result of the process of serpentinization itself. The uppermost part of the serpentinized peridotite is a fault breccia (Unit 1A), whereas in the lower part (Unit 1B), a high-temperature foliation is marked by elongate spinels. The paleomagnetic reorientation of several intervals (based on VRM measurements; see "Paleomagnetism" and "Structural Geology" sections, this chapter) indicates that the high-temperature foliation has a westerly dip (southwest through northwest) of 20° to 50°. This foliation is overprinted by fractures filled with serpentine and chlorite.

The physical properties of the sediments vary on a small scale according to lithology within the repetitive sequence of calcareous sandstone, calcareous claystone, and claystone. The sandstones are the most dense, least porous, and have the highest velocities. Claystones are at the opposite end of the spectrum. In general, sandstones are not as abundant as the other two lithologies and the entire sedimentary section most probably has characteristics close to that of the calcareous claystone component (velocity ~2600–2800 m/s, density ~2.3 g/cm^3). Magnetic susceptibility maxima reflect zones of abundant brown clay, while an overall decrease in natural gamma-ray activity with depth is most likely the result of increasing carbonate content in the deeper sediments. The top of acoustic basement is most likely located at the contact between Subunit IIC and Subunit IVA (~853 mbsf). The breccias have velocities almost double those of the overlying sediments (over 5000 m/s) and densities 10% to 20% greater (averaging around 2.6 g/cm^3). Below the breccia layer, velocity and density decrease at the contact with the underlying serpentinite of Unit 1A. The serpentinite has a lower density (2.3 g/cm^3) by virtue both of lower grain density and higher porosity, while velocity is almost as low as in the claystones (2700 m/s).

Shipboard paleomagnetic results indicate a number of magnetic reversals (711.3–855.9 mbsf). The combined biostratigraphic and paleomagnetic data indicate that these polarity zones span Chrons C29r to C21n. Whole-core magnetic susceptibility and intensity measurements and discrete samples reveal sharp peaks in the brown sediment of Core 173-1068A-8R (778.9–788.5 mbsf). This characteristic brown bed and the associated very narrow peaks in NRM intensity and volume susceptibility were also observed at nearby Sites 1067 and 900 and appear to provide an early Eocene stratigraphic marker for correlation between the sediments of the Iberia Abyssal Plain. The peaks appear to be caused by bioturbated laminae rich in magnetite of unknown origin. The NRM intensity and volume susceptibility of the serpentinite unit have average values consistently above 0.15 A/m and 0.002×10^{-5} SI units, respectively, suggesting that serpentinites could contribute significantly to magnetic anomalies observed over the OCT of the Iberia Abyssal Plain.

Because of bridges the hole was logged in two separate runs by the triple combination tool (5562–5169 mbrf, 507–114 mbsf; 5823–5669 mbrf, 768–614 mbsf). Although only the deepest 40 m of the logged interval was cored in Hole 1068A, the interval corresponds in depth to the sedimentary section cored and partially logged at Site 900, located 600 m to the east.

BACKGROUND AND OBJECTIVES

The general objective of Site 1068 was the same as that of Site 1067, namely to investigate the nature of the H reflector, a possible major synrift tectonic contact, that appears to intersect basement in the vicinity of the basement high on which Sites 900, 1067, and 1068 are situated. The reader is therefore referred to "Background and Objectives" section, "Site 1067" chapter, for the general background to Site 1068.

Site 1068 was drilled when it became clear that the strategy of drilling down through acoustic basement to the H reflector was no longer a viable proposition at Hole 1067A after the bottom-hole assembly was lost in the hole. This view was based not only on the time that would have been required at Site 1067 just to get back to the terminal depth of Hole 1067A but also on significant revisions that were required to the estimated depth to the H reflector and to the rate of penetration. First, shipboard laboratory measurements on the cores had revealed that a more realistic interval velocity for the basement above the H reflector was 5.5 km/s and not 4.0 km/s, as obtained from depth focusing error analysis and as used in the pre-stack depth migration of the Lusigal-12 profile across the site (Krawczyk et al., 1996). This implied that the target reflector actually lay 550 m below top basement, and not 400 m as originally expected. Second, estimates of drilling rate had been made on the assumption that acoustic basement was early synrift or prerift sediment in which the rate of penetration would be 12 m/hr, whereas drilling rate in the metamorphic rocks at Site 1067 had actually fallen off with depth from 6.7 to only 0.9 m/hr. Thus, the implication of continuing to drill at Site 1067 was that too much time would be consumed to allow occupation of the remaining planned sites for the leg. For all these reasons, the line of attack was altered and it was decided to offset the next site (Site 1068) to the west to attempt to drill into the top of acoustic basement at a structural level below the H reflector, rather than to continue with the strategy of drilling down to and through it. By this means, we hoped to acquire important information about what lies below the H reflector. We also hoped to establish whether or not it represents a tectonic contact or some other sort of interface and to establish its significance in geodynamic models of the development of the rifted margin and the ocean/continent transition. Thus, the principal objective of Site 1068 was to drill down through the postrift sediments and into the acoustic basement to sample the lower plate beneath the H reflector (Fig. 10 in "Introduction" chapter, this volume; Fig. 1 in "Background and Objectives" section, "Site 1067" chapter).

Site 1068 lies in a water depth of 5044 m near the southern edge of the Iberia Abyssal Plain (Fig. 3 in "Background and Objectives" section, "Site 1067" chapter). The contoured basement chart (Fig. 4 in "Background and Objectives" section, "Site 1067" chapter) shows that the site lies on a triangular local high situated on a more elongated ridge at least 22 km long that trends roughly north-northeast. The site is crossed by the east-west Lusigal-12 seismic reflection profile, which has been time- and depth-migrated (Fig. 10, "Introduction" chapter, this volume; Figs. 1, 2 in "Background and Objectives" section, "Site 1067" chapter); the north-south Sonne-21 line passes about 700 m east of the site (Figs. 2, 5 in "Background and Objectives" section, "Site 1067" chapter). The Lusigal-12 time-migrated section has features on the west flank of the basement high that suggest the presence of a small fault block along the main seaward-dipping normal fault scarp. To avoid the possibility of drilling through the eastern wedge-shaped tip of this block, to minimize the sediment column to be penetrated, and yet to drill at a structural level below the H reflector, the site was picked at shotpoint 3992 on profile Lusigal-12. The borehole location was shifted back (westward) along *Le Suroît*'s track by 70 m to allow for the offset between the watergun array and the ship's GPS aerial (Fig. 2 in "Background and Objectives" section, "Site 1067" chapter). On the time section at SP3992, there is 0.88 s TWT (860 m) and on the depth section there is ~880 m of postrift sediment. Therefore, we expected to encounter 860–880 m of postrift sediments (presumed to be turbidites and pelagites by analogy with Site 900, which lies 600 m to the east) before penetrating the acoustic basement at a structural level below the H reflector. It was decided to begin coring after drilling to 780 mbsf.

OPERATIONS

After finishing at Site 1067, the ship was moved in dynamic positioning (DP) mode to Site 1068 (IBERIA-09C; not in original prospectus) located ~1600 m to the west of Hole 1067A. Once on location, the vibration-isolated television camera system was deployed to >5000 m water depth to detorque the coaxial cable. During this time, the new drill collars for the bottom-hole assembly were picked up and the rotary core barrels were spaced out. A beacon was deployed at 1845 hr on 10 May 1997; however, the beacon signal became erratic. At 2100 hr that same day a second beacon was deployed.

Because of spooling problems with the coaxial winch, about 9 hr was spent with the TV system near the seafloor while trying to correct gaps between cable turns on the winch drum. No indication of subsea cables was observed during the survey.

The drill string was tripped to bottom and Hole 1068A was spudded at 1430 hr 11 May 1997. A corrected seafloor depth of 5055.0 mbrf was established. Drilling ahead with the RCB center bit assembly continued while checking the center bit approximately every 100 m beginning at 300 mbsf. Drilling proceeded until 1630 hr on 14 May 1997, when a depth of 711.3 mbsf was reached (Table 1). Originally the plan had been to drill to a depth of 780.0 mbsf before initiating coring; however, because of the maximum weight that could be placed on the bit while drilling with a center bit, the ever-decreasing penetration rate (2.8 m/hr) meant that coring would take equal or less time than drilling. Therefore, the center bit was recovered, and a core barrel was deployed. Coring with the RCB continued at an average rate of penetration (ROP) of 3.6 m/hr until basement was reached in Core 15R at a depth of 853.0 mbsf. Coring continued into the basement rocks, which included a several-meter-thick band of dark bluish black serpentinite breccia that was extremely difficult to core. This material packed very easily, jamming the core catcher and slowing the ROP to 1.0–2.0 m/hr. The formation graded downward into massive serpentinized peridotite. Coring was eventually suspended after Core 29R (Table 1) at a depth of 955.8 mbsf because of time constraints and the uncertainty of how much deeper the hole would have to progress before much less altered basement rock (peridotite) could be reached.

During the wiper trip that prepared for wireline logging, the driller noted constant 25,000-lb drag until a depth of 781.0 mbsf was reached. On the trip in, the top drive had to be picked up at a depth of 775.0 mbsf. In general, high torque was noted from 899.0 mbsf to 915.0 mbsf, and there were three exceptionally high torque tight spots that required heavy reaming at depths of 775.0 mbsf, 899.0 mbsf, and 908.0 mbsf. There was 6.0 m of fill on bottom. In preparation for logging, the hole was flushed with sepiolite mud, the bit was released, the sleeve was shifted, and another 265 bbl of sepiolite mud were pumped into the hole. The drill pipe was pulled to a logging depth of 114.0 mbsf, and at 0415 hr on 21 May 1997, the crew began rigging up for logging. Because the hole was in poor condition, particularly in the basement rocks, and because of the heavy reaming required during the wiper trip, the side entry sub was not used.

Wireline logging proceeded with the first suite of logging tools, the triple combination, consisting of HNGS/APS/HLDT/DIT/TLT. The first run had trouble passing a tight spot in the hole at 520.0 mbsf. After unsuccessfully expending some effort to pass this point, the hole was logged back up to the open-ended pipe (114.0 mbsf). After recovering the first suite of tools, the pipe was lowered across the bridge, placing the open-ended pipe at a depth of 614.0 mbsf. This was the deepest the pipe could be placed without severely jeopardizing the pipe string. The triple combination logging suite was again run in the hole, this time reaching a depth of 770.0 mbsf before again reaching an obstruction. The hole was logged up from that point, the tools recovered, and further wireline logging efforts were abandoned. Upon concluding wireline logging operations, the pipe was pulled clear of the seafloor at 2200 hr on 21 May 1997. A pipe overpull of 25,000 lb was noted on the first two stands of drill pipe. After pulling clear of the seafloor, the first beacon was commanded to release but did not surface. Once the second beacon was released and recovered at 2400 hr, the vessel began to move slowly in DP mode to Site 1069 (IBERIA-07B). The pipe trip continued during the DP move. The mechanical bit release reached the rig floor at 0530 hr on 22 May 1997, officially ending Hole 1068A.

Table 1. Site 1068 coring summary.

Core	Date (May 1997)	Time (GMT)	Interval (mbsf)	Length cored (m)	Length recovered (m)	Recovery (%)
Drilled from 0.0 to 711.3 mbsf						
173-1068A-						
1R	14	2100	711.3-720.9	9.6	8.27	86.1
2R	15	0030	720.9-730.6	9.7	6.97	71.9
3R	15	0415	730.6-740.3	9.7	9.85	101.5
4R	15	0800	740.3-749.9	9.6	8.96	93.3
5R	15	1055	749.9-759.6	9.7	7.84	80.8
6R	15	1620	759.6-769.3	9.7	9.95	102.6
7R	15	2030	769.3-778.9	9.6	7.13	74.3
8R	15	2350	778.9-788.5	9.6	9.87	102.8
9R	16	0355	788.5-798.1	9.6	9.62	100.2
10R	16	0800	798.1-807.7	9.6	4.50	46.9
11R	16	1115	807.7-817.3	9.6	7.73	80.5
12R	16	1525	817.3-826.9	9.6	9.91	103.2
13R	16	2135	826.9-836.6	9.7	8.88	91.5
14R	17	0300	836.6-846.3	9.7	9.13	94.1
15R	17	0900	846.3-855.9	9.6	6.57	68.4
16R	17	1450	855.9-865.6	9.7	6.91	71.2
17R	17	1925	865.6-869.2	3.6	4.37	121.4
18R	17	2315	869.2-875.2	6.0	4.54	75.7
19R	18	0450	875.2-884.9	9.7	6.80	70.1
20R	18	1155	884.9-894.5	9.6	8.78	91.5
21R	18	1920	894.5-904.2	9.7	1.84	19.0
22R	19	0250	904.2-913.8	9.6	2.16	22.5
23R	19	1010	913.8-923.2	9.4	2.72	28.9
24R	19	1535	923.2-932.6	9.4	1.92	20.4
25R	19	2100	932.6-937.0	4.4	3.35	76.1
26R	20	0010	937.0-941.9	4.9	3.78	77.1
27R	20	0415	941.9-946.4	4.5	1.23	27.3
28R	20	0950	946.4-951.3	4.9	4.18	85.3
29R	20	1300	951.3-955.8	4.5	2.83	62.9
			Cored totals	244.5	180.59	73.9
			Drilled	711.3		
			Total	955.8		

An expanded version of this table with individual section lengths is on the CD-ROM, back pocket, this volume.

LITHOSTRATIGRAPHY

Hole 1068A penetrated a 142-m-thick, middle Eocene to Maastrichtian sedimentary sequence, consisting of carbonate turbidites, hemipelagites, and contourites, that overlies a 41.5 m succession of breccias. A simplified summary of the lithostratigraphy cored at this site and other Leg 173 and Leg 149 sites is shown in Figure 1. The middle to lower Eocene succession cored at Site 1068 is very similar to that of the same age encountered at Site 900 (Shipboard Scientific Party, 1994c) and Site 1067 ("Site 1067" chapter, this volume), located 600 and 1400 m, respectively, to the east. Therefore, it is assigned to the lower part of Subunit IIB, as defined at Site 900. The lower Eocene to Maastrichtian succession is designated as Subunit IIC. Subunit IIC is distinguished from Subunit IIB by a higher proportion of nannofossil claystone and nannofossil chalk and the presence of beds of these lithologies up to 45 cm thick.

The breccia succession at this site is designated as Unit IV. This is because (1) it, like the olistostrome at Site 897 (Shipboard Scientific Party, 1994a; Comas et al., 1996), and the olistostrome and/or possible rock fall deposit at Site 899 (Shipboard Scientific Party, 1994b; Comas et al., 1996; Gibson et al., 1996a), is the product of

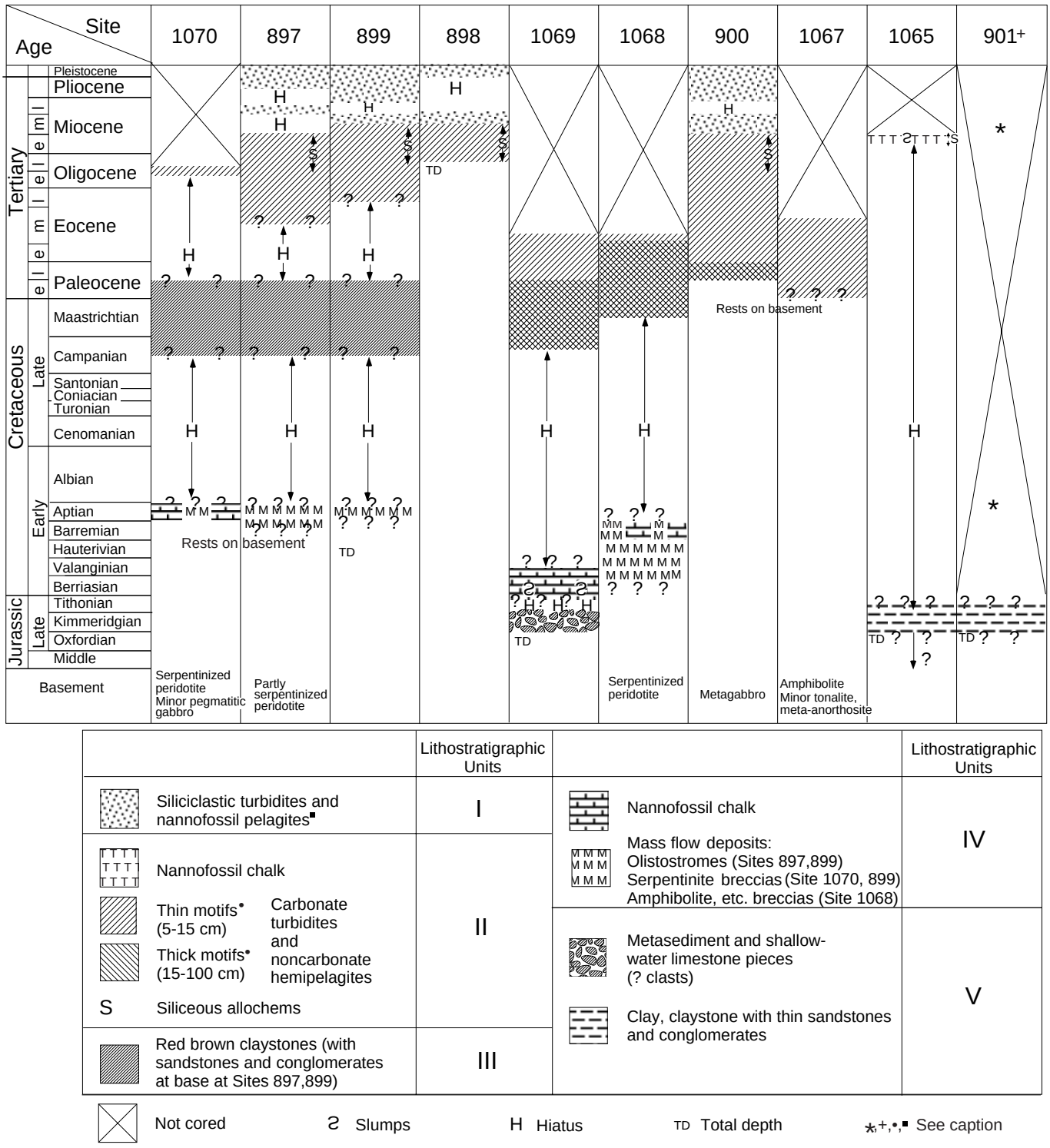

Figure 1. Simplified summaries of stratigraphic successions cored at Leg 149 and Leg 173 sites. Unit III is almost barren of fossils and so its age is very uncertain. + = Unit V as shown in Site 901 was designated by Shipboard Scientific Party (1994d) as Unit II, following the normal ODP practice of numbering units sequentially downhole; * = a washed core recovered Miocene nannofossil ooze and a 5-mm-thick layer of gray clay of Aptian age. Solid square = nannofossil pelagites dominant at Site 900. Solid circles = "motifs" referring to types of upward-darkening sequences shown in Figure 3 and in Figure 8 of the "Site 1069" chapter (this volume). The cross-hatched symbols on the summary chart indicates that both thin (Motif 2) and thick (Motif 1) sequences are present.

mass-wasting processes and is also Early Cretaceous in age, and (2) the red claystone and conglomerate successions of Unit III drilled at these Leg 149 sites were not encountered at Site 1068 (Fig. 1). Unit IV is divided into three subunits on the basis of clast and matrix compositions. In addition, the lowermost subunit exhibits a strong hydrothermal and cataclastic overprint.

Rotary coring (RCB) was employed in Hole 1068A, yielding 87% average recovery for sediments of Unit II and 85% for those of Unit IV. Coring began at 711.3 mbsf (Subunit IIB) and penetrated serpentinized mantle peridotite at 893.13 mbsf, just below the base of Subunit IVC (see "Igneous and Metamorphic Petrology" and "Structural Geology" sections, this chapter). Figure 2 summarizes the core recovery, lithologies, and ages of the lithostratigraphic units recognized in Hole 1068A. The ages, lithologic compositions, colors, facies and depositional environments, boundary depths, and cored intervals of Units II and IV are summarized in Table 2.

As in Holes 900A and 1067A, Subunit IIB in Hole 1068A is dominated by upward-darkening sequences of claystone overlying calcareous claystone, often with thin beds or laminae of calcareous siltstone at the base of individual sequences. Subunit IIC contains alternating intervals of thin- to thick-bedded claystone and calcareous claystone, and upward-darkening sequences of claystone overlying calcareous claystone, some of which are much thicker (up to 45 cm thick) than those in Subunit IIB (Figs. 3, 4). Nannofossil claystone and nannofossil chalk often occur in place of calcareous claystone in the upward-darkening sequences; thick intervals of these nannofossil-rich

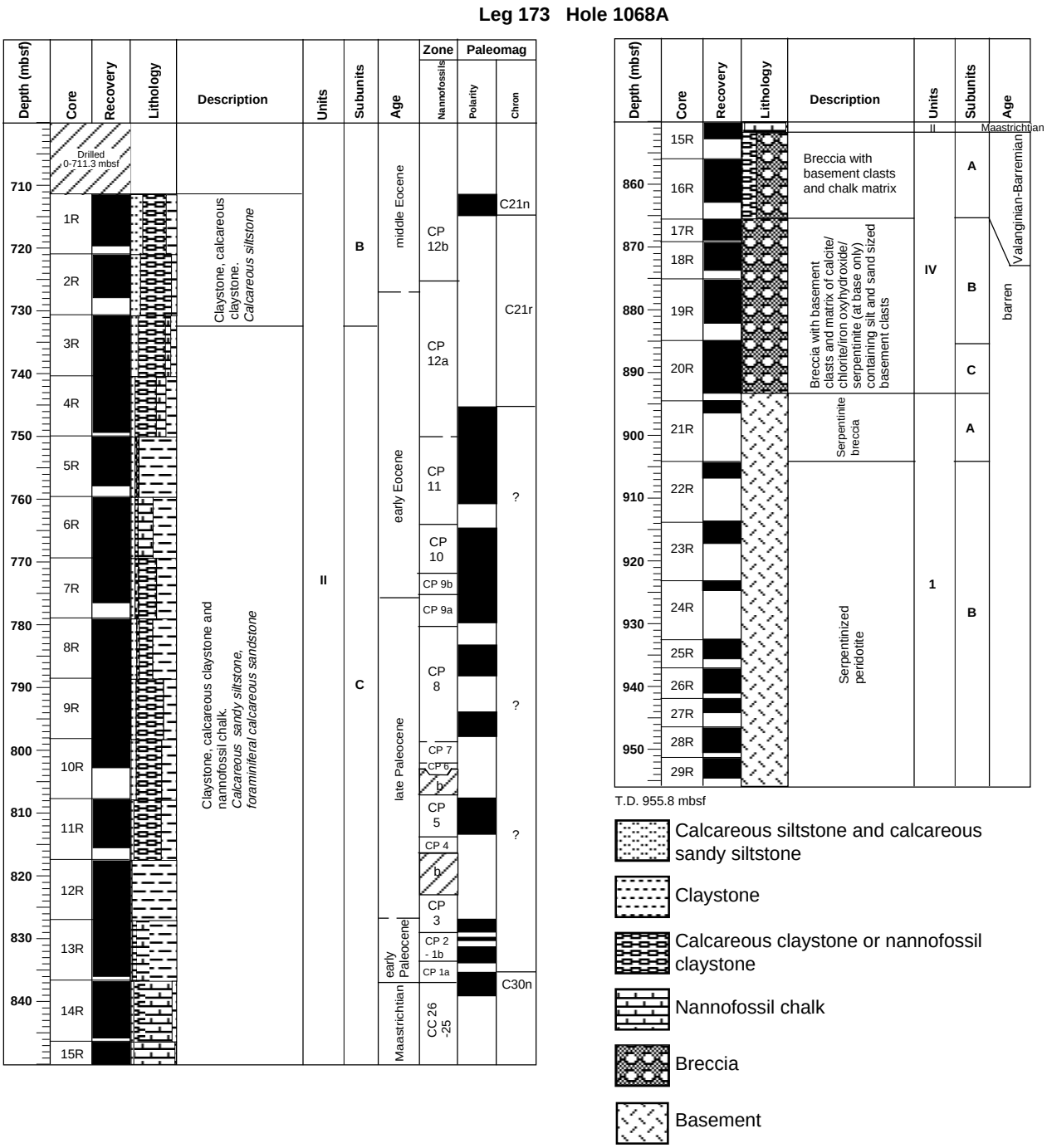

Figure 2. Summary lithostratigraphic column for Hole 1068A. Minor lithologies are listed in italics. b = cores barren of nannofossils.

Table 2. Summary of lithostratigraphic Units II and IV at Site 1068.

Lithostratigraphic unit	Age	Thickness (m)	Major lithology *Minor lithology*	Color	Facies and *environment/setting* (Total meters described)	Depth (mbsf)	Occurrence
IIB	middle–early Eocene	>22.25	Calcareous claystone 60% Claystone 30% *Calcareous siltstone 10%*	Grayish green Greenish gray Light gray	Carbonate turbidites and phyllosilicate clay hemipelagites *On west flank of basement ridge/ base of continental rise* (18.19)	Shallowest: 711.3 Base: 733.55	1R-1, 0 cm 3R-3, 45 cm
IIC	early Eocene to Maastrichtian	119.47	Claystone ~50% Calcareous claystone and nannofossil chalk ~40% *Calcareous sandy siltstone ~8%* *Foraminiferal calcareous sandstone ~2%*	Moderate brown Grayish green/light brown Light gray Light gray	Carbonate turbidites and phyllosilicate clay hemipelagites, minor contourites *On west flank of basement ridge/ base of continental rise* (106.65)	Top: 733.55 Base: 853.02	3R-3, 45 cm 15R-5, 17 cm
IVA	Early Cretaceous (Valanginian–Barremian)	12.58	Breccia with basement clasts and chalk matrix	Dark greenish gray Pale orange	Debris flow *Derived from adjacent and more distant highs* (8.61)	Top 853.02 Base: 865.60	15R-5, 17 cm 17R-1, 0 cm
IVB	Barren	19.3	Clast-supported breccia containing basement clasts in a matrix composed of sand and silt sized clasts encased in fine grained calcite and iron oxyhydroxides	Dark gray/greenish gray and grayish orange	Talus and/or rock fall(s) *Near an active fault* (24.48)	Top: 865.60 Base: 884.9	17R-1, 0 cm 20R-1, 0 cm
IVC	Barren	8.23	Breccia with basement clasts showing jig-saw brecciation, and cataclasite matrix composed of calcite, chlorite, albite, and oxyhydroxides. Matrix also contains sand- to silt-sized basement clasts.	Light greenish gray and grayish orange	Cataclasite (15.80)	Top: 884.9 Base: 893.13	20R-1, 0 cm 20R-7, 105 cm

lithologies occur only in Subunit IIC. Relatively thick intervals of calcareous sandy siltstone and foraminiferal calcareous sandstone occur as distinct minor lithologies in Subunit IIC. Sediments in both subunits are interpreted as hemipelagites and turbidites, with possibly some evidence of reworking by contour currents.

Unit IV is divided into three subunits based on matrix composition. Subunit IVA is a breccia composed of meta-igneous clasts, including amphibolite and gabbro, set in a matrix of light-colored calcareous chalk. The breccias in Subunit IVB consist of meta-igneous clasts set in a matrix of micrite and microspar containing silt- to sand-sized meta-igneous mineral and rock fragments. The breccias of Subunit IVC exhibit a significant cataclastic and hydrothermal overprint, and so are described and discussed in the "Igneous and Metamorphic Petrology" and "Structural Geology" sections in this chapter. Subunit IVA is interpreted as debris-flow deposits, and Subunit IVB as talus or rock-fall deposits.

Unit II

Interval: 173-1068A-1R-1, 0 cm, through 173-1068A-15R-5, 17 cm
Depth: 711.3–853.02 mbsf
Age: middle Eocene to Maastrichtian

General Description

Recovery of Unit II over the 142-m cored section averaged 87% and ranged from 47% to 103% (Table 2). The sediment is firm to hard, and core disturbance is generally restricted to slight fracturing.

The four lithologic motifs shown in Figure 3 are end-members of a spectrum of lithologic associations and thickness variations observed in Unit II. Motif 2 is typical of the upward-darkening sequences identified in Subunit IIB at this site, and which also occur in Subunit IIC. They occur in Subunit IIB at Sites 900 (Shipboard Scientific Party, 1994c) and 1067 (see "Lithostratigraphy" section, "Site 1067" chapter, this volume). The upward-darkening sequences, generally 3 to 15 cm thick, consist of dark claystone overlying lighter calcareous claystone, or almost white nannofossil claystone or nannofossil chalk (Fig. 4). In Cores 14R and 15R, some of the calcareous lithologies show irregularly shaped light brown bands, presumably resulting from diagenetic alteration.

Thin beds or laminae of light gray calcareous sandy siltstone typically occur at the base of the sequences, but they are sometimes absent. The calcareous siltstone bases show a variety of features including massive bedding, lenticular, planar, wavy, and cross-lamination, and bioturbation. Within a given sequence, the contact between the calcareous siltstone and overlying greenish gray calcareous claystone may be bioturbated, sharp and planar, or wavy, and may be erosional. Gradational and bioturbated contacts also occur. Within individual sequences bioturbation (*Planolites*?) typically extends downwards from the dark claystone at the top into the underlying calcareous claystones. *Chondrites* is sometimes observed in the calcareous claystone interval.

Motif 1 is similar to Motif 2, but the lowermost part of the upward-darkening sequence is much thicker (typically ≤45 cm, but as much as 1 m in rare cases) and usually composed of nannofossil or calcareous chalk (Fig. 5). These lowermost calcareous lithologies may rest directly on dark claystone. Sometimes one or two laminae of calcareous sandy silt may occur at the base, occasionally accompanied by one or two burrows, filled with this lithology, that penetrate a few millimeters below the basal contact. Thicker intervals of calcareous sandy siltstone to sandstone, or foraminiferal chalk, sometimes occupy the basal portion of Motif 1 sequences (Fig. 5). They may contain parallel, wavy, lenticular, or cross-lamination. There is often an interlaminated interval at the transition between the lower siltstone or sandstone and overlying carbonate-rich intervals. The dark claystone at the top of an individual Motif 2 sequence may (Fig.

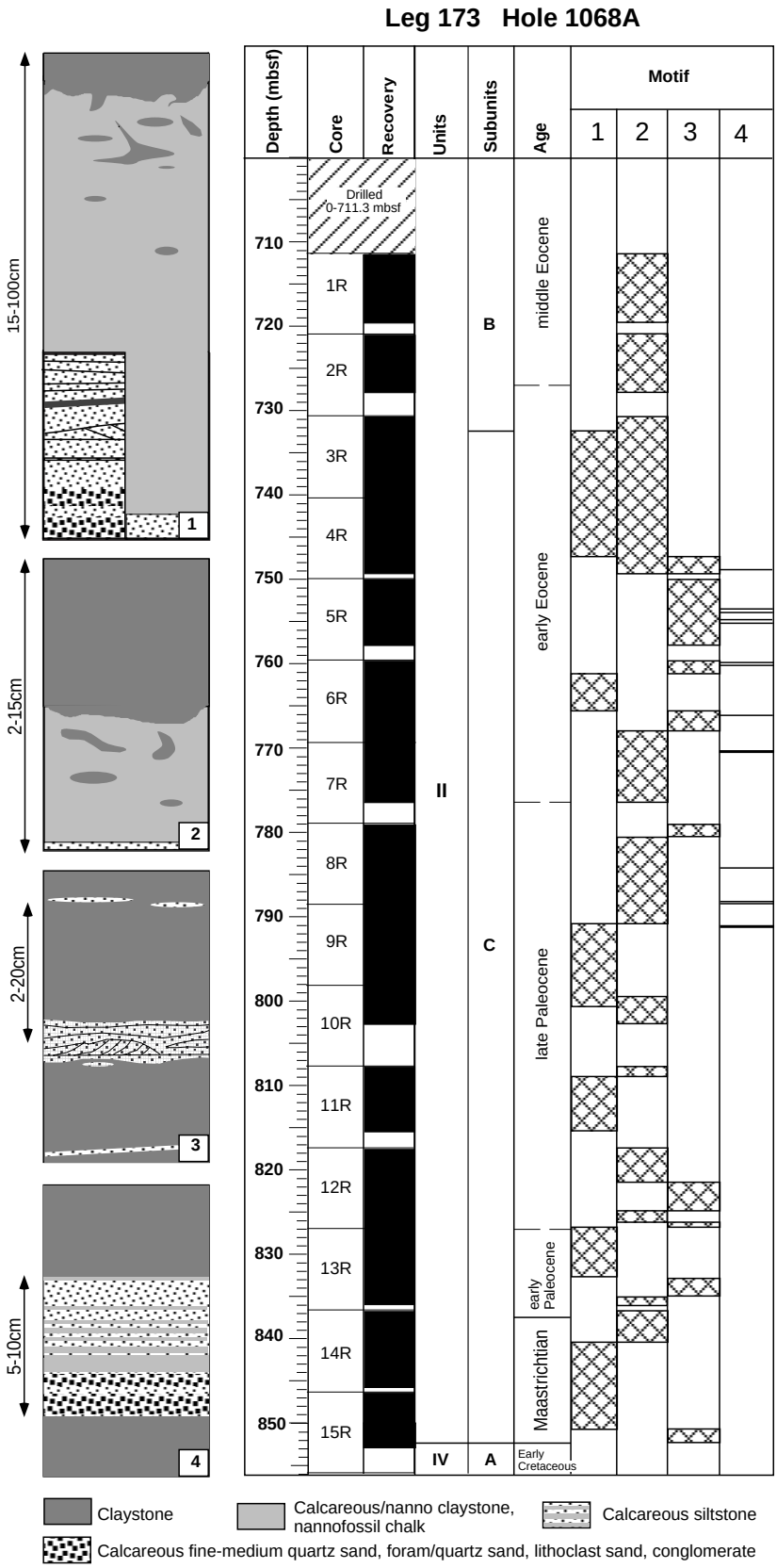

Figure 3. Lithologic motifs and their distribution in lithostratigraphic Unit II at Site 1068. The four motifs shown on the left side of the figure are idealized end-members of a spectrum of lithologic associations observed in the cores. Motifs 1 and 2 are variants of upward-darkening sequences. Motif 1 is much thicker than the others and is dominated by nannofossil chalk or nannofossil claystone. These calcareous lithologies may rest directly on the claystone of the underlying motif (Fig. 5), or be underlain by thin laminae or thin to medium beds of calcareous sandy siltstone containing parallel, wavy, lenticular, or cross laminae (Fig. 5). The uppermost claystone may be thicker than that shown (Fig. 5) or only be represented by burrow fills within nannofossil claystones and chalks (the lower part of Fig. 5B, 90–98 cm, shows an example of this feature in a Motif 2 sequence). Motif 2 sequences are up to 15 cm thick, and usually contain only thin basal intervals (<1 cm) of calcareous sandy siltstone. The claystone cap may be absent, but a record of its former presence may be preserved in burrow fills in calcareous claystone, nannofossil claystone, or nannofossil chalk. Motif 3 does not contain any fine-grained calcareous lithologies: a basal calcareous sandy siltstone interval (<2 cm thick), containing structures similar to those occurring in the same lithology in Motifs 1 and 2 (plus disrupted laminae, as shown in Fig. 6), is overlain by brown claystone. Motif 4 also consists of calcareous siltstone/sandstone (5–15 cm thick) overlain by brown claystone. The calcareous siltstone/sandstone contains similar structures to those occurring in the coarser basal parts of the other motifs, but may also be massive (lower part of Fig. 7). In addition, parallel interlaminated calcite cemented sandstones and foraminiferal micritic sandstones occur (upper part of Fig. 7). The right side of Figure 3 shows the distribution of the four motifs in the cored interval of Unit II. The sandstones of Motif 4 are shown as lines in column 4.

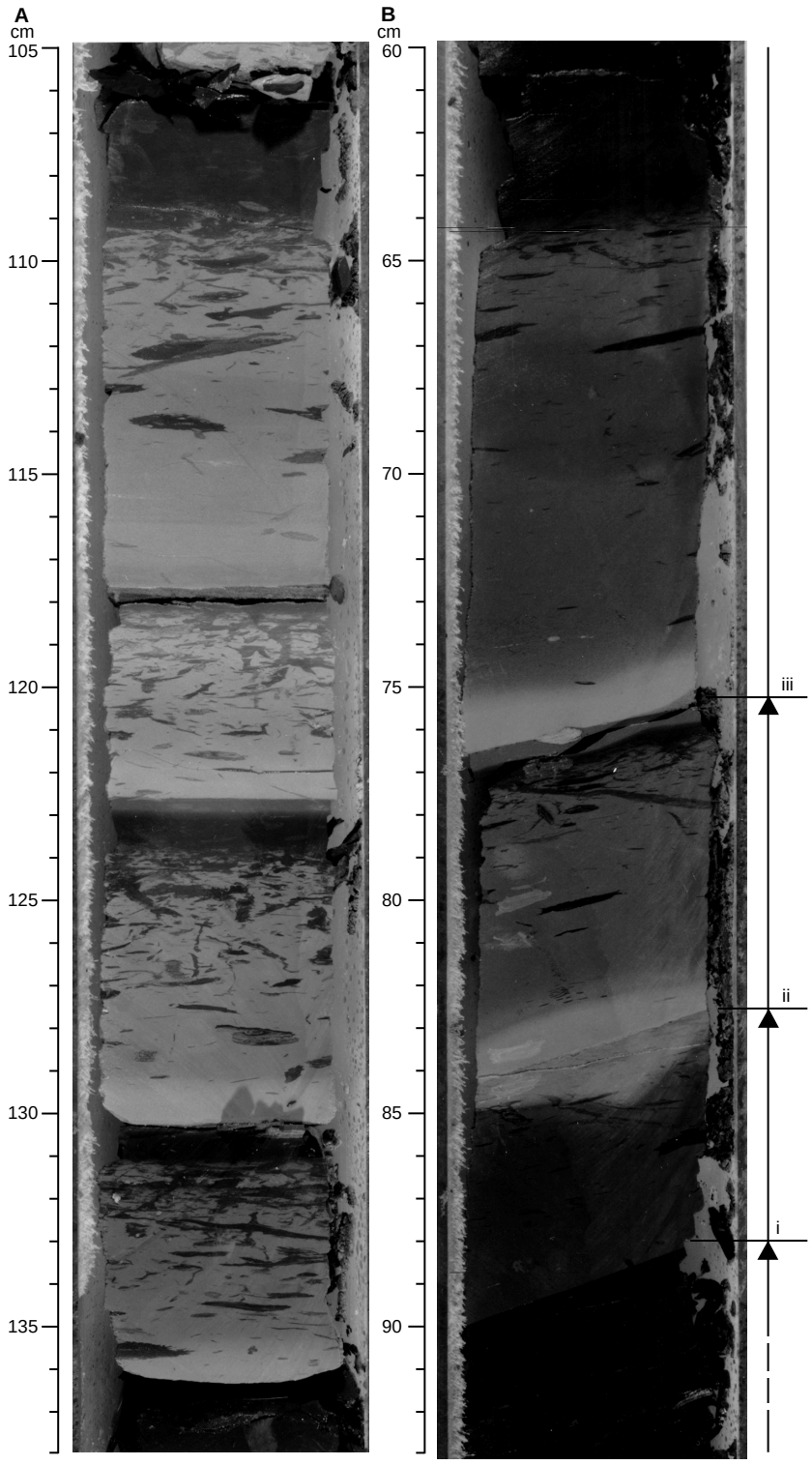

Figure 4. Motif 2 upward-darkening sequences in Core 173-1068A-13R. **A.** Interval 173-1068A-13R-2, 105–138 cm. The photo shows four sequences. The lower carbonate-rich intervals are composed entirely of nannofossil chalk (118–136.5 cm) or nannofossil claystone underlain by calcareous sandy siltstone (110–118 cm). The bases of the lower three sequences are almost white, but the upper parts are light brown. **B.** Interval 173-1068A-13R-4, 60–93 cm. The bases of upward-darkening sequences (ii) and (iii) and the top of (i) are moderate brown (darker on photograph). The lighter areas on the photograph are greenish gray, possibly indicating the diagenetic reduction of original iron oxyhydroxides. A single burrow filled with calcareous sandy siltstone occurs at the base of sequence (iii). The presence of this burrow suggests that a turbidity flow older than sequence (iii), but younger than (ii), deposited a layer of sandy silt. A later flow—probably that which deposited sequence (iii)—swept away the silt, but not before the burrow was filled with this coarser sediment.

5) or may not show comparable thickening, or may be thin or absent, save for a record of its former presence preserved as burrow fills within the calcareous lithologies (Fig. 5).

Motif 3 is characterized by thin- to medium-bedded moderate brown claystone that contains laminae and thin beds, up to 2 cm thick, of sandy siltstone (Fig. 6). Greenish gray calcareous clay may occur above, or interlaminated or interbedded, with the siltstones. Bioturbation may disrupt these lithostratigraphic contacts and internal structures, but wavy and cross laminae are sometimes present in the calcareous claystone and siltstone beds.

Motif 4 consists of calcareous sandstone and rare conglomerate beds, which exhibit sharp contacts with underlying and overlying brown claystones (Fig. 7). The coarser interval of Motif 4 is highly variable in grain size and composition, including calcareous sandy

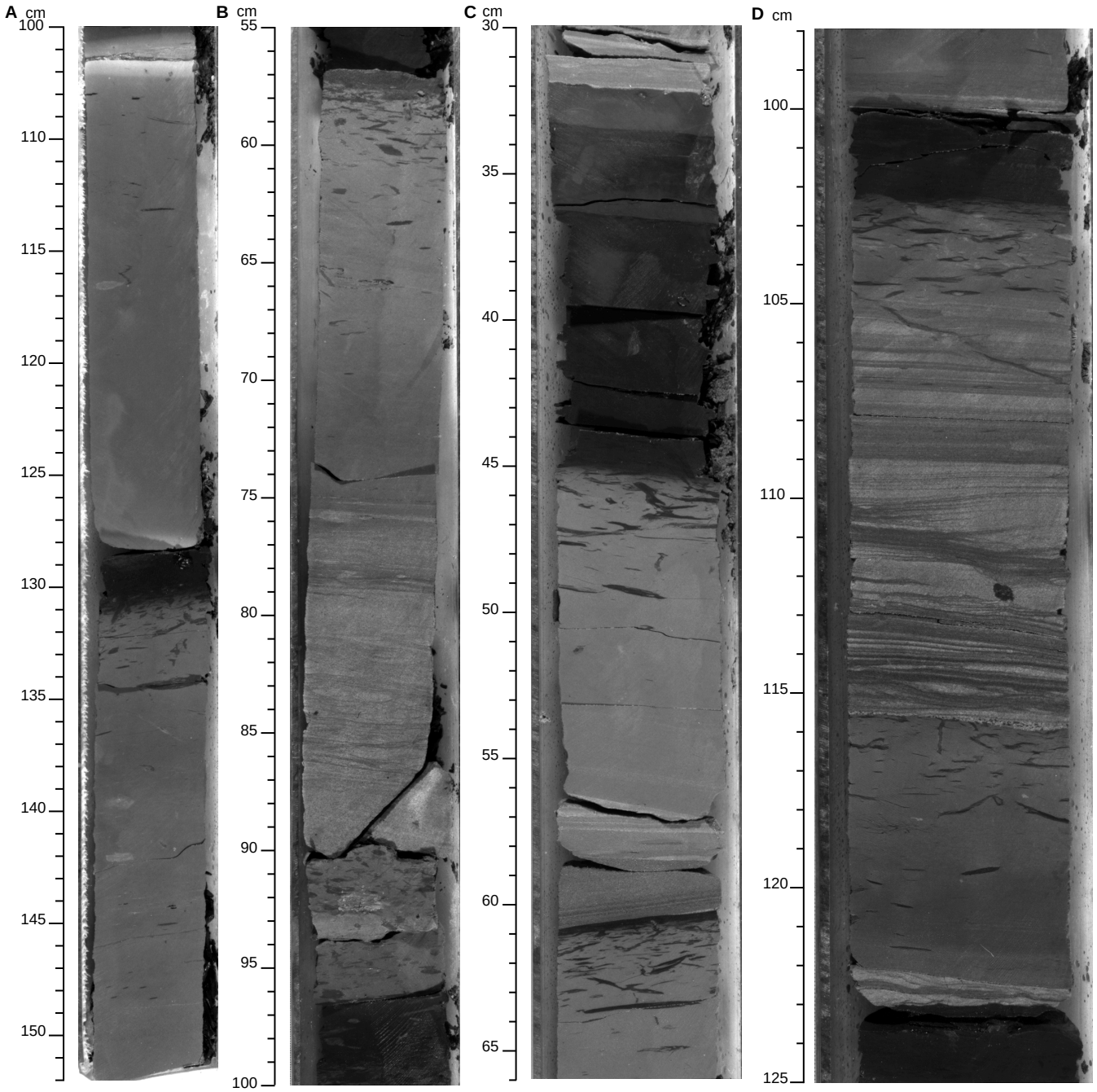

Figure 5. Core photos showing features present in examples of Motifs 1 and 2 in Hole 1068A. **A.** Interval 173-1068A-13R-4, 100–152 cm. Two thick intervals of nannofossil chalk. The lower one (of which the basal 2 cm occur in the underlying Section 5, not shown) is capped by brown claystone, but the claystone cap to the upper interval was eroded before the deposition of the overlying sediments; its former presence is revealed by a few claystone-filled burrows. **B.** Interval 173-1068A-13R-6, 55–100 cm. The nannofossil chalk lower part of a Motif 1 sequence, of which the laminated part is composed of alternations of foraminiferal chalk and nannofossil chalk. Only the basal 2 cm of the overlying claystone is shown at the top of the photograph: its total thickness is 28 cm. **C.** Interval 173-1068A-10R-1, 30–66 cm. A Motif 1 sequence containing a thick brown claystone (36–45 cm); the base is burrowed down (45–49 cm) into the underlying nannofossil claystone. The base of the motif contains interlaminated nannofossil clay and calcareous sandy siltstone (56.5–58.5 cm) and laminated calcareous sandy siltstone (58.5–61 cm), with a shallow scour at the left filled with calcareous fine-grained sandstone. The underlying motif is capped by a thin claystone. **D.** Interval 173-1068A-9R-3, 98–125 cm. Two examples of Motif 2: the upper one (between 100–115.5 cm) is dominated by interlaminated calcareous claystone and calcareous sandy siltstone containing parallel, cross, and lenticular lamination. At the base, lithoclastic sand fills a shallow scour on the right side of the core. Note that there is no single distinct boundary between the sandy siltstone and the overlying calcareous claystone; the laminae of the former gradually die out up to 105 cm. Erosion removed the claystone top from the underlying motif (115.5–123 cm); the only traces of it that remain are the darker burrow fills of claystone. (Continued next page.)

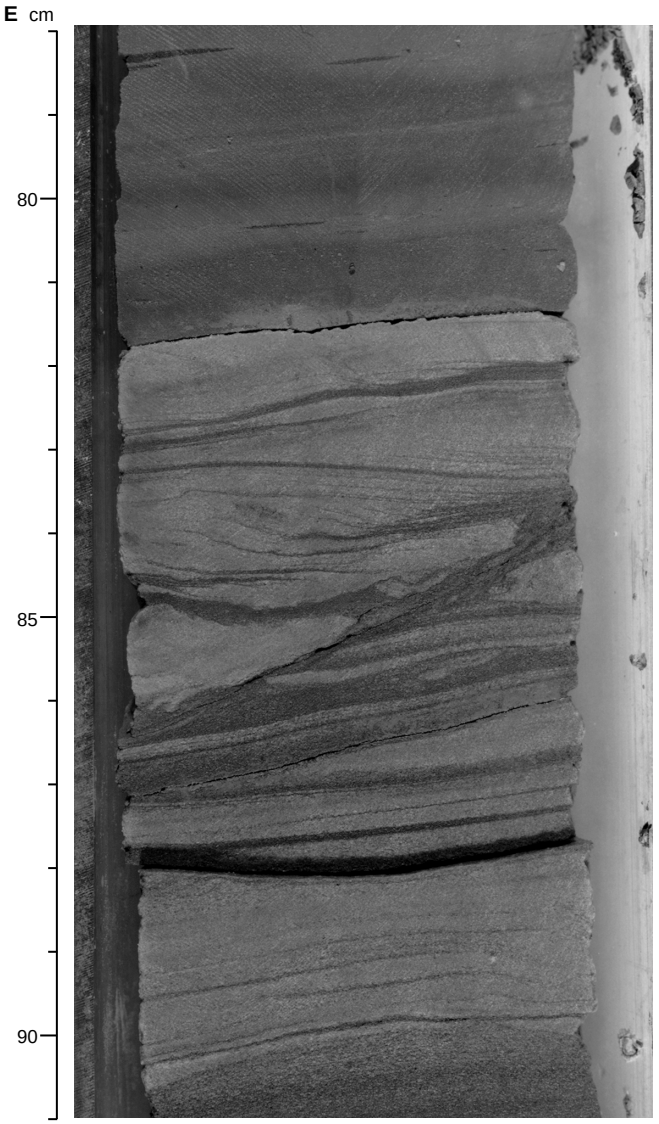

Figure 5 (continued). **E.** Interval 173-1068A-9R-5, 78–91 cm. A calcareous sandy siltstone interval at the base of a Motif 1 sequence containing parallel and cross laminae. Beneath the latter there is some disruption above a surface inclined from right to left between 84–86.5 cm, which may be a synsedimentary fault. Concave-up laminae between 89–90 cm, and a lenticular lamina at 83.5 cm (left side), suggest ripple bedforms. Note the sharp contact with the overlying calcareous claystone.

siltstone, medium-grained calcareous foraminiferal sandstone, and coarse-grained lithoclastic sandstone and conglomerate. Internal structures include parallel, wavy, lenticular, and cross-lamination.

Subunit IIB

Coring began in Subunit IIB at 711.3 mbsf. Core recovery of Subunit IIB averaged 86%. Some of the upward-darkening sequences (Motifs 1 and 2) show upward-fining, but in other cases there is no grain-size change between the lighter colored, more carbonate-rich

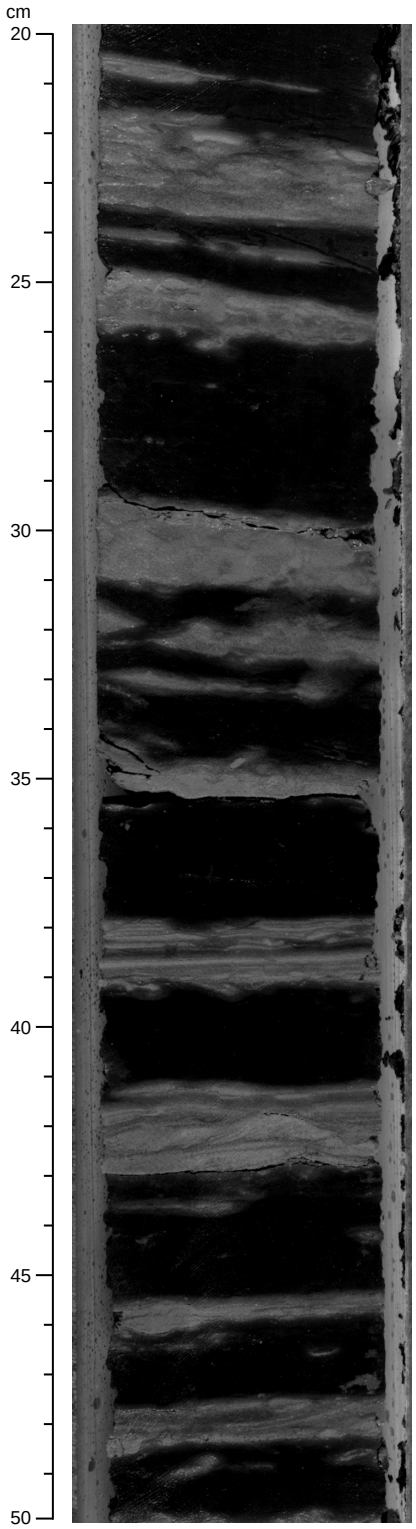

Figure 6. An interval showing Motif 3 sequences in interval 173-1068A-5R-4, 20–50 cm. Layers of lighter colored calcareous sandy siltstone show parallel and cross laminae, and disrupted irregular layers possibly caused by burrowing or soft sediment deformation. Lighter colored reduction halos around the silty layers extend into the dark (brown) claystones.

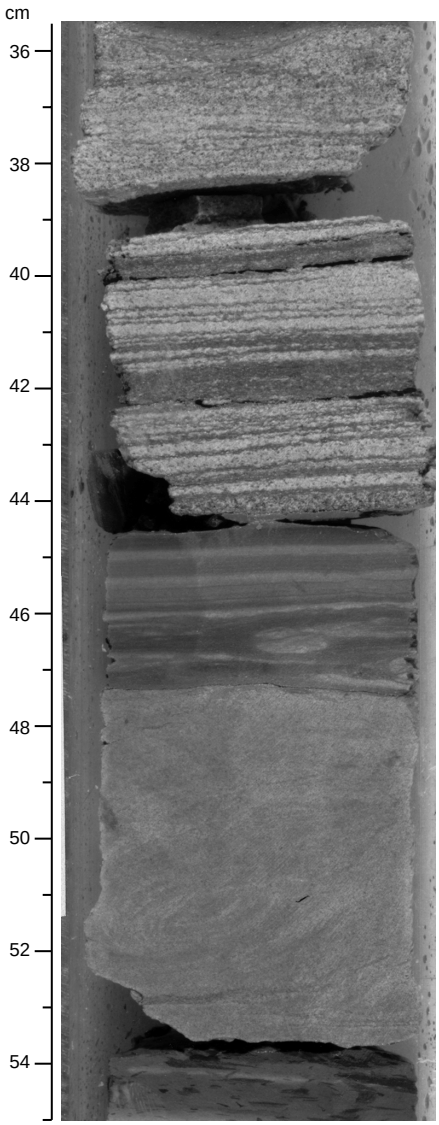

Figure 7. Two examples of Motif 4 sandstones showing sharp tops and bases from Section 173-1068A-6R-1. The upper one (35.5–44.5 cm) contains parallel interlaminated calcite cemented foraminiferal sandstone (darker) and micritic foraminiferal sandstone (lighter). The lower calcareous sandy siltstone (47.4–53.6 cm) is massive apart from some faint ovoid-shaped laminae.

sediments and the overlying darker phyllosilicate claystones. Following the procedure outlined in the Site 1067 "Lithostratigraphy" section, the upward-fining symbol was used on the barrel sheets (see Section 3) to represent all upward-darkening sequences, and was placed at the base of individual upward-darkening sequences. The symbol for "calcareous chalk" was used to represent calcareous claystone, as the AppleCORE program does not include a symbol for the latter lithology.

In addition to the boundary types and internal structures described by Motif 2, ball and pillow structures occur in the calcareous sandy siltstone in Section 173-1068A-2R-1, and small-scale slumping and microfaults with slickensides are present in small intervals in Core 173-1068A-2R.

Subunit IIC

The boundary between Subunits IIB and IIC is placed at interval 173-1068A-3R-3, 45 cm (733.55 mbsf), at the top of the first occurrence of a relatively thick (27 cm) nannofossil chalk interval. The boundary marks the change from a succession dominated by Motif 2 (Subunit IIB) to one in which all four motifs occur (Subunit IIC; see Fig. 3).

Core recovery of Subunit IIC averaged 88%. The subunit is dominated by brown to dark greenish gray claystone (50%), light greenish gray nannofossil chalk and greenish gray to pale yellowish brown calcareous claystone, and calcareous silty claystone (40%). Minor lithologies include light gray calcareous siltstone and calcareous sandy siltstone (~8%) and light greenish gray calcareous foraminiferal sandstone (~2%). A coarse-grained lithoclastic sandstone occurs as a minor lithology in Section 173-1068A-9R-2 (Fig. 8).

Upward-darkening sequences with the characteristics of Motif 1, in which the light-colored calcareous claystone or nannofossil chalk interval is relatively thick, occur in intervals 173-1068A-3R-3, 33 cm, to 4R-5, 150 cm, 1068A-6R-1, 77 cm, to 6R-4, 42 cm, and again in 1068A-9R-2, 120 cm, to 11R-CC, 24 cm. In rare cases, the claystone interval overlying the expanded calcareous interval is also relatively thick (as much as 15 cm; e.g., Core 173-1068A-11R).

The thick upward-darkening sequences contrast sharply with long intervals of claystone within which Motif 3 occurs. These thick clay-rich intervals occur in intervals 173-1068A-4R-6, 0 cm, to 6R-1, 77 cm, 6R-4, 42 cm, to 9R-2, 120 cm, and 12R-1, 0 cm, to 12R-CC, 20 cm. A 260-cm-thick interval of massive brown claystone, containing very few light calcareous laminae, occurs in Sections 1068A-8R-1 and 8R-2.

Subunit IIC also contains an increased variety of siltstone and sandstone intervals with characteristics of Motif 4. Beds of light gray calcareous sandy siltstone, 3- to 11-cm thick, are present within the dominantly brown claystones in Cores 173-1068A-5R, 6R, and 7R. Beds of medium-grained light greenish gray calcareous foraminiferal sandstone, 2–36 cm thick, occur in Cores 1068A-5R, 7R, and 8R. They show faint parallel laminae and sometimes contain scattered flakes of black plant debris and lenses of greenish gray claystone. Finally, an unusual dusky brown to dark greenish gray sandstone, 6 cm thick, containing orange-colored granule-sized clasts (possibly strongly altered glauconite?) and well-preserved cross-lamination occurs in Section 1068-9R-2 (Fig. 8).

Petrography

The petrographic features of the Unit II sediments from Hole 1068A are similar to those documented in the Hole 1067A chapter. This section, therefore, only describes features not observed in the latter hole.

In Subunit IIC, the light-colored lower parts of individual upward-darkening sequences are often more carbonate-rich than their equivalents in Hole 1067A. This is revealed by both smear-slide analyses (which show a greater proportion of calcareous and nannofossil chalks) and carbonate analyses (which show a greater proportion of samples with more than 50% carbonate). The carbonate-rich lithologies are common in the lower parts of Motif 1 sequences that characterize Subunit IIC.

Foraminiferal sands and chalks occur as parallel and wavy interlaminations at the bases of the calcareous and nannofossil chalks in

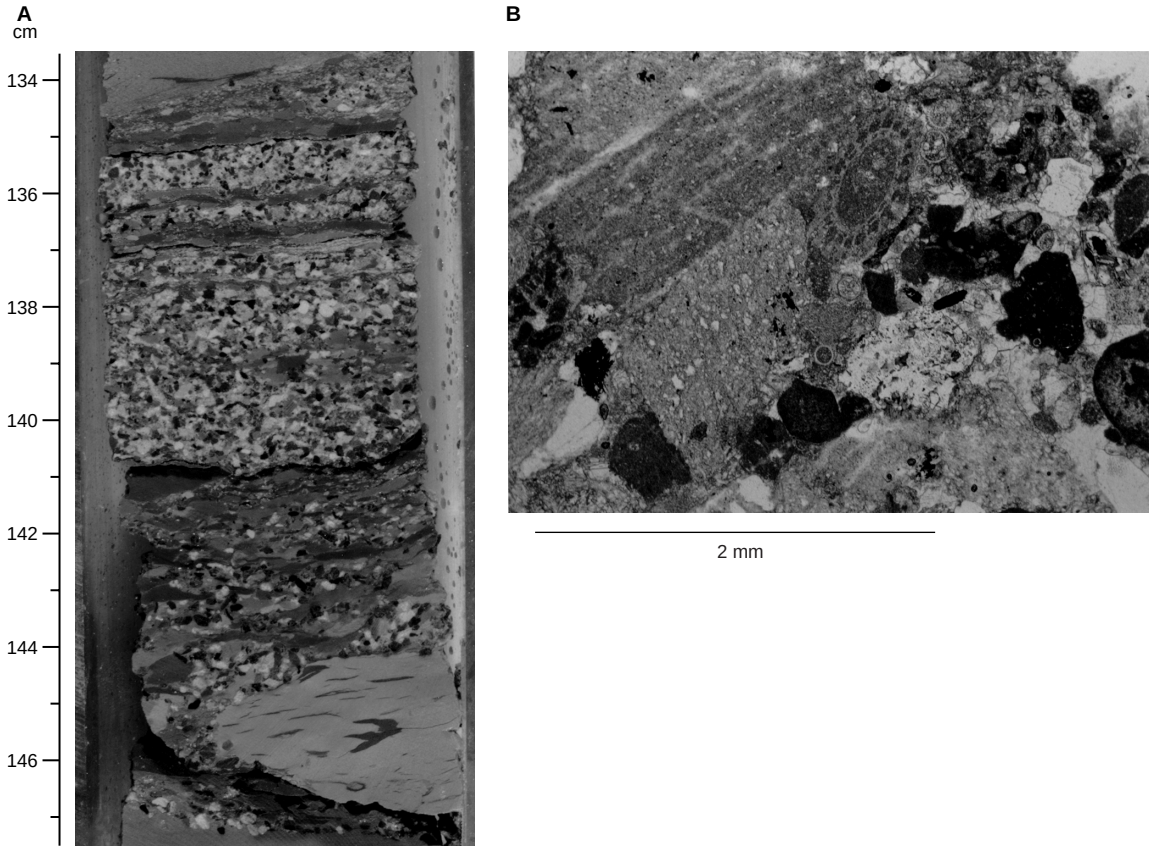

Figure 8. Lithoclastic sandstone to conglomerate (interval 173-1068A-9R-2, 133.5–147.5 cm). **A.** Core photograph showing clasts consisting of shallow-water limestones and pelites and laminae of darker calcareous claystone. Bioturbation has disrupted the lower boundary. **B.** Photomicrograph of thin section: to the left of the ovoid echinoderm spine occur two large pelite clasts; parts of two more occur at the bottom of the photograph. The darker clasts are composed of cryptalgal micrite. Angular quartz clasts occur, and one composed of biotite hornfels is situated to the left of the angular dark limestone clast at the center right. Thin-shelled planktonic foraminifers are scattered between the clasts. The sediments are well compacted, with sparite cement occurring only on the right side of the photograph.

Motif 1 sequences in Subunit IIC, particularly from Core 173-1068A-7R to the base of the subunit (Fig. 5). They may also be interlaminated with calcareous sandy siltstones. These lithologies are dominated by complete and/or fragmented planktonic foraminifers, which may occur in a micritic matrix or calcite microspar cement.

Thin- to medium- (as much as ~13 cm) thick beds of coarse lithic sandstone and conglomerate are more common in Hole 1068A than Hole 1067A (Fig. 8). They consist of a mixture of clasts, including shallow-water limestones (peloidal grainstones, coated and micritized grains, skeletal fragments), chalk, and basement rocks (arkose, pelite, meta-arenite, mica schist). A single pebble (1.5 cm across) of mica schist occurs at interval 173-1068A-15R-3, 18 cm.

Depositional Processes

The interpretation of the upward-darkening sequences as calcareous turbidites overlain by hemipelagic clays that is given for Hole 900A by Shipboard Scientific Party (1994c) and for Hole 1067A (this volume), applies to the Unit II sediments in Hole 1068A. The recognition of the four lithologic motifs shown in Figure 3 and consideration of the sedimentological implications of the location of Hole 1068A at a lower level on the western flank of the basement high permit some refinement of this broad environmental interpretation.

The Unit II/Eocene sedimentation rate at Site 1068 was much higher (~47 m/m.y.) than at Site 900 (~18 m/m.y.; Shipboard Scientific Party, 1994c, fig. 6) and Site 1067 (29–35 m/m.y.; "Site 1067" chapter, this volume). The relative sediment starvation at Sites 900 and 1067 was probably the result of turbidity flows partially by-passing these relatively elevated locations (Fig. 10, "Introduction" chapter, this volume), a suggestion consistent with the lower proportion of turbiditic calcareous lithologies at these sites (24% and 30%, respectively, of the total recovered cores in Subunit IIB) compared to Site 1068 (60% in Subunit IIB and 40% in Subunit IIC). Motif 3 occurs in all three holes. It may have resulted from turbidity flows dropping only sandy silts, with the suspended load of fine-grained carbonate sediment being carried further downslope. Alternatively, contour currents may have eroded away the carbonate component, leaving laminae or thin beds of sandy silt behind. The same origin may apply to the sharp-topped sandstones occurring in Motif 4, although the coarser clasts composed of shallow-water limestones and basement rocks must have been transported from high areas to the north by turbidity flows before being reworked by contour currents.

The bases of some Motif 1 and Motif 2 sequences contain parallel, wavy, cross, and lenticular laminae of silt or foraminiferal sand. Sharp-topped intervals showing these features were interpreted as evidence of some reworking by contour currents at Site 900 (Shipboard

Scientific Party, 1994c) and Site 1067 ("Site 1067" chapter, this volume) and this inference applies at Site 1068. Where the laminated interval passes gradually into overlying carbonate lithologies, it is possible that the former may have been formed by turbidity flow. Such structures are common in fine-grained siliciclastic turbidites and result from "suspension fall-out and traction, shear sorting of silt grains and clay flocs in the bottom boundary layer" (Pickering et al., 1989, p. 25). However, in the absence of clay flocs in fine-grained carbonate turbidity flows, it is uncertain whether such structures would develop, and so the influence of contour currents cannot be ruled out. They are very likely to have contributed to the preferential sorting of foraminifers into individual laminae, alternating with silt-rich or micrite-rich laminae, which are commonly observed at the base of some upward-darkening sequences.

Unit IV

Interval: 173-1068A-15R-5, 17 cm, through 173-1068A-20R-7, 105 cm
Depth: 853.02–893.13 mbsf
Age: Early Cretaceous (Valanginian–Barremian) to ? (barren)

General Description

The contact between Subunit IIC and Unit IV occurs at interval 173-1068A-15R-5 (Piece 1, 17 cm; 853.02 mbsf). This boundary marks the first occurrence of light-colored limestone clasts and dark basement clasts in a very pale orange to moderate reddish orange chalk matrix. Core recovery in Unit IV averaged 86% and ranged from 70% to 91% (Table 1). Core disturbance is restricted to slight fracturing.

Unit IV is comprised entirely of extremely poorly sorted breccia. It is subdivided into three subunits based on changes in matrix composition and clast deformation (Fig. 2). Subunit IVA consists of matrix to clast-supported breccias, in which a few Tithonian–Lower Cretaceous calpionellid limestone clasts occur. The matrix consists of calcareous chalk yielding Lower Cretaceous (Valanginian–Barremian) nannofossils. The contact between Subunits IVA and IVB is placed at the top of Core 173-1068A-17R. Subunit IVB consists entirely of clast-supported breccias, the matrix of which consists of fine-grained calcite that contains sand- to silt-sized metabasic mineral and rock fragments. Subunit IVC contains breccias that have been subjected to significant hydrothermal alteration and cataclasis; they are described in the "Igneous and Metamorphic Petrology" and "Structural Geology" sections, this chapter.

Visual estimates of the proportion of clasts were made by using diagrams in Rothwell (1989), and the following four categories were used: <20%, 20%–30%, 30%–50%, and >50%. A preliminary comparison of clast proportions obtained by visual estimation and by image analysis reveals only moderate agreement between the two methods (Fig. 9). Where >50% clasts are present, the breccia is considered to be clast supported. On the barrel sheets (see Section 3), the proportion of clasts is represented by light gray to black shading in the column usually used to show "Bioturbation Intensity" (see Fig. 1, "Explanatory Notes" chapter, this volume).

Clast size as measured across the cut surfaces of the cores seldom exceeds 10 cm; however, clasts up to 25 cm long are occasionally present. Clast sorting is extremely poor.

Subunit IVA

Subunit IVA is 12.6 m thick and is dominated by angular dark greenish gray metabasic clasts set in a carbonate matrix (Fig. 9; Table 2). Meta-igneous clast lithologies include foliated amphibolite, anorthosite, metagabbro, and microamphibolite. Minor epidote-rich clasts are also present in Cores 173-1068A-15R and 17R. Pinkish gray very fine-grained limestone clasts only occur at the top of the subunit (Section 173-1068A-15R-5). Clast size rarely exceeds 10 cm; however, longer clasts (12–25 cm long) occur in Samples 173-1068A-15R-6 (Piece 1), 16R-1 (Piece 1), 16R-3 (Piece 4), and 16R-4 (Piece 1).

On the basis of the characteristics of the matrix, at least three separate breccia subunits are present in Subunit IVA; incomplete recovery prevented observation of the nature of the contacts between them:

1. From the top of Unit IV (interval 173-1068A-15R-5, 20 cm) to interval 1068A-15R-6 (Piece 1, 1 cm), the matrix of the breccia consists of a pale orange to white to pinkish gray very fine-grained limestone, which includes nannofossils. Scattered coarse sand- and granule-sized clasts of meta-basic rocks and minerals are incorporated in the matrix.
2. The matrix of the next breccia subunit (intervals 173-1068A-15R-6, Piece 2 through Piece 4) consists of greenish red to greenish gray carbonate mudstone, which contains numerous meta-igneous clasts ranging in size from silt to small pebbles (Fig. 10).
3. The matrix of the breccia in Core 173-1068A-16R is very pale orange to moderate orange-pink carbonate mudstone and contains sand- and granule-sized clasts which are generally matrix supported. Diffuse randomly oriented millimeter-scale bands of red-brown coloration occur in the matrix in Section 1068A-16R-3. Additional breccia units may be present in the intervals that were not recovered.

Calcite, probably filling original interclast void spaces, occurs in Section 173-1068A-16R-2, and occurs as veins <2 mm across in Sections 1068A-16R-4 and 16R-5. Clasts with irregular millimeter-scale rims of sparry calcite occur in Sections 1068A-15R-6 and 1068A-16R-5 and 16R-6. An example of calcite-rimming metagabbro and amphibolite clasts is shown in Figure 10.

Subunit IVB

Subunit IVB is 19.3 m thick and is dominated by angular dark greenish gray meta-igneous clasts in a multicolored matrix of clay-sized carbonate containing silt- to sand-sized meta-igneous minerals and rock fragments (Fig. 11). Locally, the matrix also contains calcite, as vein (Sections 173-1068A-19R-1 and 20R-3, 20R-4, and 20R-6) and possible void space fillings (Cores 173-1068A-17R to 19R), chlorite (Section 1068A-19R-2), and iron oxyhydroxides (Section 1068A-19R-5). The matrix in Subunit IVB shows a range of colors, including dark greenish gray, light olive brown, moderate brown, dusky yellow green, dusky yellowish orange, and dusky yellow.

Clast lithologies in Subunit IVB include microamphibolite, metagabbro, anorthosite, amphibolite, fine-grained metabasite, epidosite, olivine gabbro, dunite, and serpentinite. Measured clast sizes seldom exceed 10 cm and are typically less than 7 cm. The visually estimated proportion of clasts is variable (between <20% and >50%), but is generally greater in Cores 173-1068A-17R and 18R than in Core 19R.

A 5-cm interval of moderate reddish brown silt- to sand-sized material occurs at the base of Section 173-1068A-17R-2 and at the very top of Section 1068A-18R-1, which includes subrounded clasts up to 1 cm in diameter. This lithology has a gradational contact with the breccias above and below it.

Two distinct features that occur towards the base of Subunit IVB are (1) faint irregular color banding in the matrix in Sections 173-1068A-19R-3 and 4; (2) a change in the occurrence of calcite, which occurs largely within shelter porosity beneath larger clasts near the

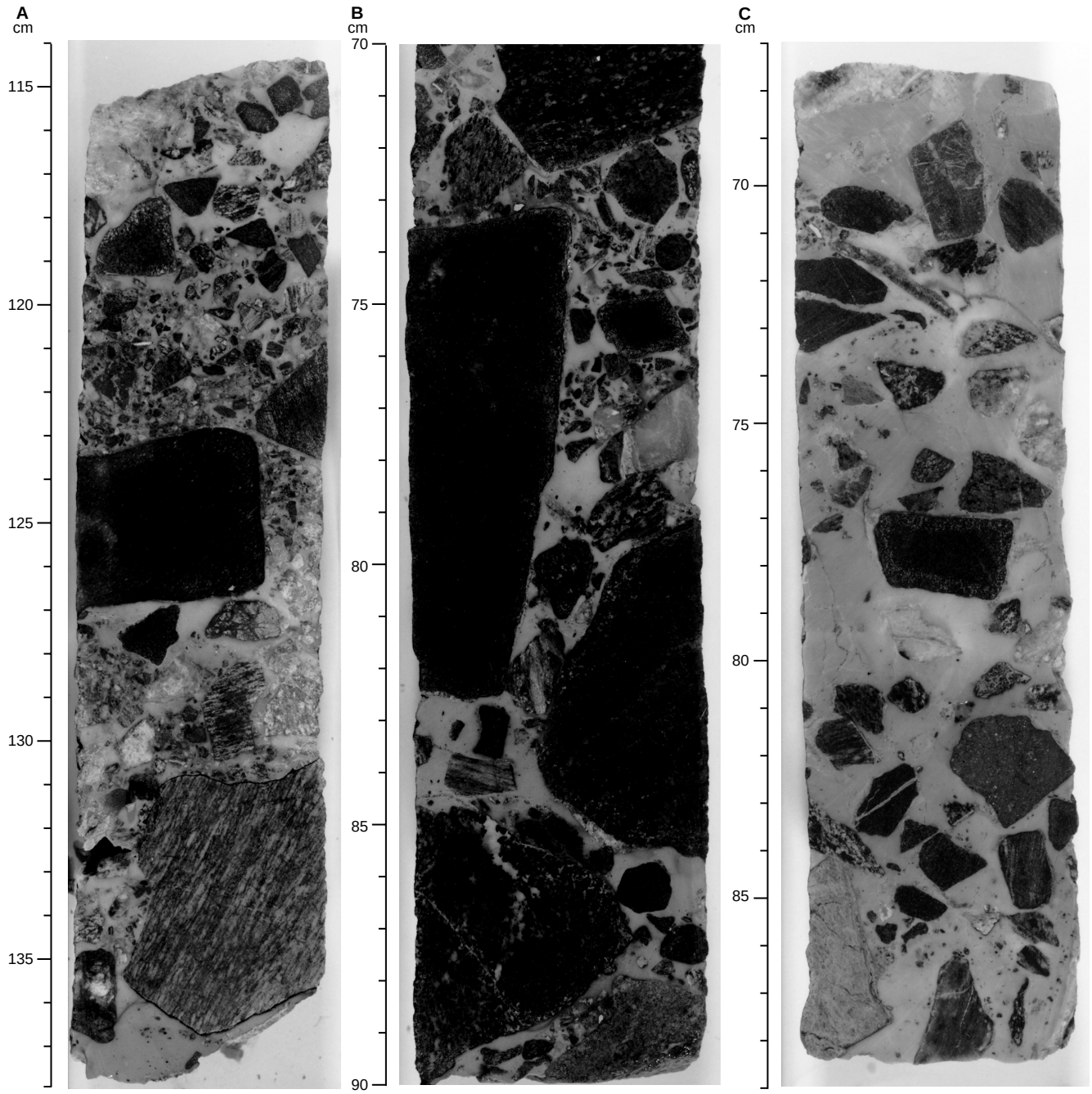

Figure 9. Photos of breccia in Core 173-1068A-16R, Subunit IVA, showing variation in clast proportions. **A.** Interval 173-1068A-16R-1, 114–138 cm. Estimate of proportions of clasts: visually = >50%; by image analysis = 61%. Note how the proportion of smaller clasts (sand to granule sized) varies within the matrix: between 116–119 cm on the right of the core, and below the larger clasts at 127 cm and 137 cm, smaller clasts are almost absent. They appear in greater proportions above the clasts at 123.5 cm and 131 cm, suggesting some settling through the matrix after deposition. **B.** Interval 173-1068A-16R-3, 70–90 cm. Estimate of proportion of clasts: visually = ~50%; by image analysis = 73%. **C.** Interval 173-1068A-16R-4, 67.5–88.5 cm. Estimate of proportion of clasts: visually = <20%; by image analysis = 31%. (Continued next page.)

top of the unit and in veins near the base of the unit. These features may be the result of an increased degree of fluid-rock interaction (see "Igneous and Metamorphic Petrology" section, this chapter). The base of Subunit IVB is placed at 173-1068A-20R-1, 0 cm.

Petrography

The matrix of the breccias in Subunit IVA consists of calcareous chalk, which appears in thin section as micrite. The matrix varies from clast free to containing sand- and gravel-sized clasts of metaigneous rocks. In Pieces 2 through 4 in Section 173-1068A-15R-6, the matrix consists of calcite microspar (<0.02 mm), each crystal of which shows a reddish brown dusty rim. Silt- to sand-sized metaigneous clasts are scattered throughout. One clast of biotite schist was observed in a thin section taken at Sample 173-1068A-16R-5, 91–95 cm. Many clasts in this interval (as seen in the cut core and in thin section) possess rims of elongate calcite crystals (0–3 mm as seen in cut core; 0–0.2 mm in thin section; Fig. 10). Calcite veins, up to 0.5

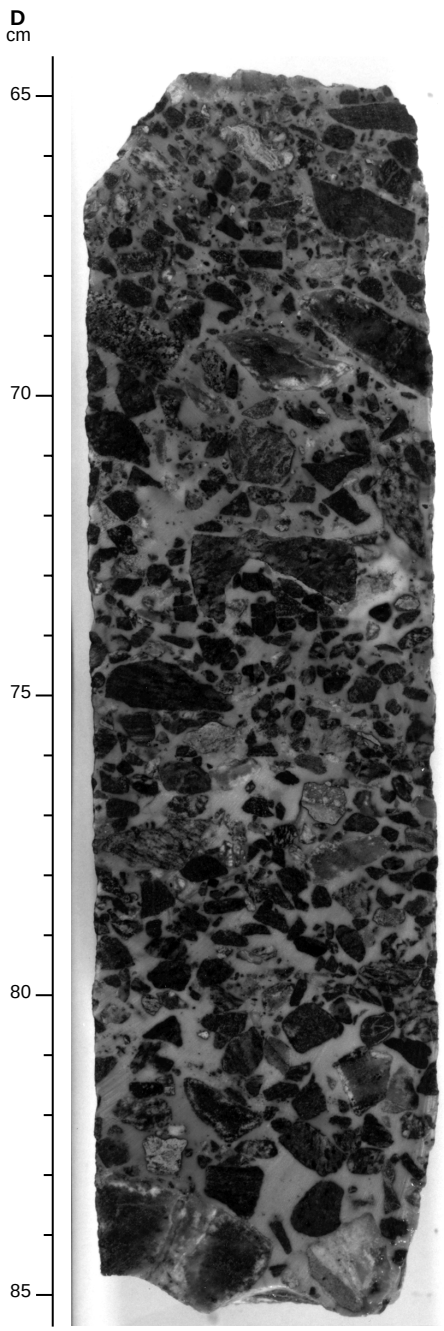

Figure 9 (continued). **D.** Interval 173-1068A-16R-6, 65–85 cm. Estimate of proportion of clasts: visually = >50%; by image analysis = 51%.

mm across, wrap around the clasts, and within them inclusion ghosts of older calcite rims are visible.

The matrix of the breccias in Subunit IVB contains numerous silt- to sand-sized clasts. It contains calcite spar occupying shelter porosity beneath larger clasts, with the remainder of the interclast spaces being filled with a mixture of calcite microspar and micrite; sometimes the latter is aggregated into peloids. Further study may reveal whether the finer grained calcite and peloids are depositional features or are the result of redeposition within pore spaces of diagenetic or hydrothermal precipitates.

The results of XRD analyses of the breccias are presented in the "Igneous and Metamorphic Petrology" section (this chapter).

Depositional Processes

The presence of a depositional matrix of calcareous chalk (probably a recrystallized nannofossil chalk) in the breccias of Subunit IVA suggests transport by and deposition from debris flows. The change in matrix composition from chalk, with minor amounts of sand- and gravel-sized meta-igneous clasts, to a clast-rich matrix in interval 173-1068A-15R-6 (Pieces 2 through 4), to a clast-poor matrix below, suggests the presence of at least three separate debris flows. The presence of calpionellid limestone clasts, and two sand-sized clasts of biotite schist seen in thin section indicate that at least a small proportion of the flows was derived from sources more distant than the Site 900 meta-igneous basement high.

The clast-supported breccias of Subunit IVB probably originated as rock fall or talus deposits accumulating beneath a steep slope. Thin (<20 cm) intervals containing smaller clasts indicate that more than one depositional event was responsible for Subunit IVB.

It is possible that an unconformity separates Subunits IVA and IVB (Fig. 12). This conclusion is based on the interpretation of the depositional processes responsible for each subunit. Debris flows are able to move up to tens to hundreds of kilometers down slopes inclined at only a few degrees; talus deposits and rockfalls originate only from steep slopes, and the angle of repose of the former is likely to be about 30° (Stow, 1994). The existence of an unconformity, or hiatus, between the two subunits is also supported by the observation that a hydrothermal overprint (in particular the presence of albite: see discussion of XRD analyses in "Igneous and Metamorphic Petrology" section, this chapter) in the matrices of the breccias is observed only toward the base of Subunit IVB. The calcareous chalk matrices of Subunit IVA are unaffected, which suggests that they were deposited after the main hydrothermal activity affecting Subunit IVB had ceased, or that the chalk matrix of the breccias in Subunit IVA may have effectively isolated it from the activity nearby.

BIOSTRATIGRAPHY

Biostratigraphically, the calcareous claystone section of lithostratigraphic Unit II is essentially continuous (ignoring minor gaps caused by barren intervals or incomplete recovery) and ranges from middle Eocene to Maastrichtian in age. Core recovery was considerably better than at previous sites drilled on this leg, and an essentially complete Paleocene section was observed for the first time at an ODP site in this region. Calcareous microfossils are common and generally well preserved at the tops of both the Eocene and Paleocene sections, but become less so toward the bottoms of those intervals, parts of which were deposited as microfossiliferous turbidites below the CCD.

The prevalence of turbidites throughout Unit II accounts for the constant background of reworked Cretaceous nannofossils in most samples as well as reworked planktonic foraminifers in samples from Core 173-1068A-10R downward, where they become dominant close to the K/T boundary in Core 173-1068A-13R. The fact that many of the fossiliferous intervals, which are bounded by unfossiliferous dark red or green clays, have been introduced by turbidity currents lends caution to straightforward biostratigraphic interpretations and could complicate correlations between the biostratigraphy and magnetostratigraphy. In general, however, the turbiditic material still falls within the expected biostratigraphic sequence; thus, the turbidity flows apparently mostly entrained the most recently deposited materials in the source areas and did not involve massive mixing of older sediments.

An intact K/T boundary was not recovered at this site as it had apparently been eroded away completely or thoroughly mixed within the bioturbated turbidites. The chalky matrix of the breccias of Subunit IVA yielded rare Lower Cretaceous nannofossils. Pelagic calpionellid limestone cobbles at the top of the breccia, apparently em-

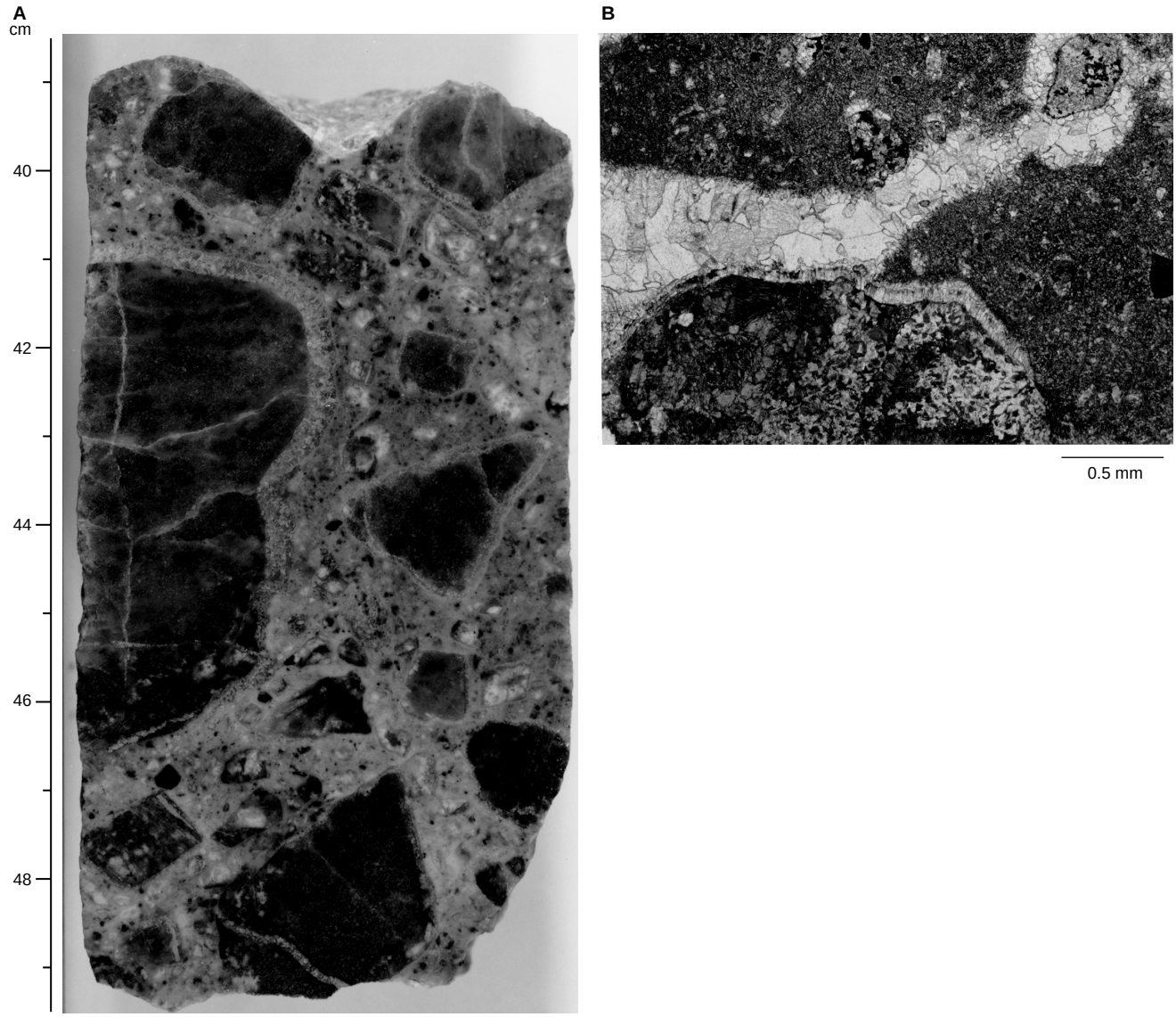

Figure 10. Clast-rich matrix in Subunit IVA in Hole 1068A. **A.** Interval 173-1068A-15R-6, 38.8–49.5 cm: the carbonate mud matrix contains clasts ranging from less than silt sized to granules and pebbles, in contrast to the matrices shown in Figure 9, which contains only sand-sized and larger clasts. Note the rims of elongate crystals of calcite spar surrounding the larger clasts. These vary in thickness around each clast. **B.** Interval 173-1068A-15R-6, 29–31 cm: photomicrograph in plane-polarized light of clast (at the base) with fringe of elongate calcite crystals that dies out to the left and right. The clast is set in a microspar matrix containing small clasts, and is cut by a calcite vein, within which the inclusion-rich calcite fringe to the clast is visible.

placed by a debris flow, are Late Jurassic to earliest Cretaceous in age (see "Lithostratigraphy" section, this chapter).

The age-depth plot for this site (Fig. 13; Table 3) is similar to that for Site 1067 in that it indicates high sedimentation rates for the uppermost lower Eocene to the lowest middle Eocene (roughly 48.5–49.5 Ma), where there is considerable pelagic carbonate in a sequence deposited well above the CCD. A thinner middle Eocene section was drilled here, however, and thus sedimentation rates are a bit lower. Similarly, relatively low rates are indicated for the lower Eocene (50–54 Ma), where carbonate dissolution was intense because of deposition close to and below the CCD and because turbidites were diverted away from the crestal area of the basement high that was draped only by pelagic sediments.

Sedimentation rates were higher again in the Paleocene section (55–65 Ma), where nannofossils were abundant and quite well preserved in some intervals, but not in others. The Paleocene section is much thicker here than at Site 1067, but there are many carbonate-barren intervals and probably a number of minor hiatuses.

A major disconformity separates the uppermost Cretaceous interval from the Lower Cretaceous. The age of the latter interval is not well constrained, as indicated by the box from 121 to 135.8 Ma in Figure 13.

Planktonic Foraminifers

The planktonic foraminifers of Unit II vary in preservation and abundance. Rich and diverse assemblages of poor to moderately well-preserved specimens have been recovered from Samples 173-1068A-2R-CC, 3R-CC, 7R-CC, and 10R-CC; 13R-CC and 14R-CC also contain abundant, moderately well-preserved, specimens, but the assemblages are of relatively low diversity (Table 4). All other core-catcher samples contained either very rare occurrences of poor-

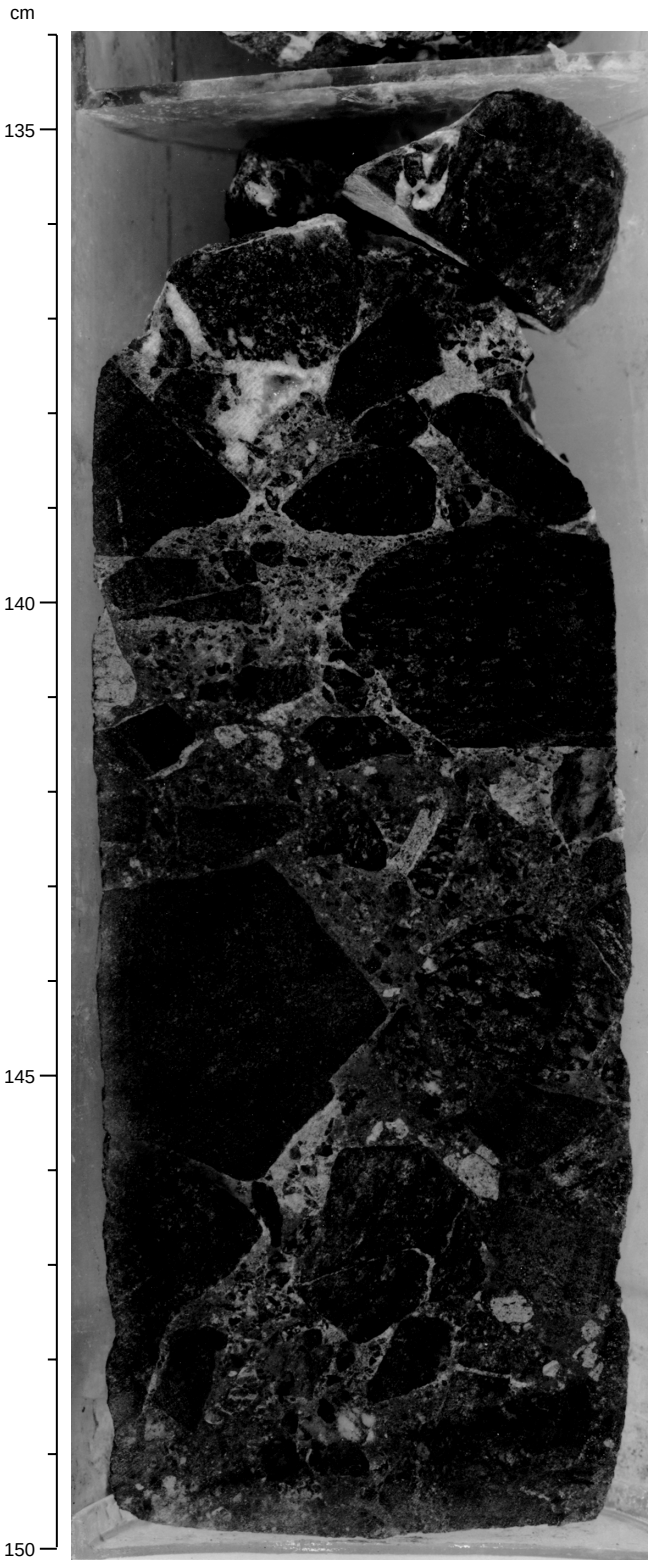

Figure 11. Core photograph of a breccia in Subunit IVB, interval 173-1068A-17R-4, 134.5–150 cm. The matrix consists of calcite microspar and micrite with dispersed silt- to granule-sized clasts. In places, interclast porosity is filled with sparry calcite (136–139 cm).

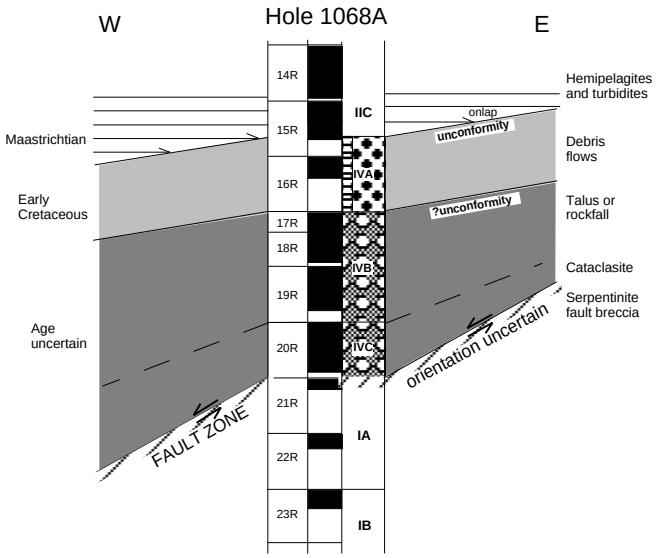

Figure 12. Sketch showing possible depositional processes and stratigraphic and structural relationships between breccia subunits and overlying sediments and underlying mantle serpentinite at Site 1068. Note that the angular relationships shown cannot be determined precisely. If Subunit IVB is a talus deposit, its lateral extent would be relatively narrow, and its lower boundary with Subunit IVC would be inclined at a higher angle (assuming no post-depositional tectonic rotation).

ly preserved and indeterminate forms or were barren. Sample 173-1068A-2R-CC contained rare, poorly to moderately well-preserved specimens of *Globigerina eocaena, Acarinina broedermanni, Morozovella aragonensis, Pseudohastigerina wilcoxensis,* and *Acarinina soldadoensis,* whose co-occurrence indicates Zone P9 (early Eocene). Core 173-1068A-3R yielded abundant but poorly preserved forms, including the species *Globigerina eocaena* and *Acarinina soldadoensis angulosa,* also suggesting Zone P9. Sample 173-1068A-10R-CC yielded a rich and diverse assemblage of moderately well-preserved forms including *Acarinina convexa, Morozovella aequa, Globanomalina pseudomenardii,* and *Pseudohastigerina wilcoxensis,* which is consistent with a late Paleocene, Zone P4 age. Sample 173-1068A-11R-CC is barren of planktonic foraminifers, and Sample 173-1068A-12R-CC only contains small foraminifers in the 63–125-µm size fraction. One of these smaller forms belongs to the species *Globanomalina pseudomenardii,* which is restricted to the upper Paleocene Zone P4. Sample 173-1068A-13R-CC is taken from a highly bioturbated horizon, and the foraminiferal assemblage recovered is dominated by Upper Cretaceous planktonic foraminifers. The assemblage also contains common *Eoglobigerina eobulloides*, a species that ranges from the base of the Tertiary to the upper Danian, Zone P2. The species *Parvularugoglobigerina eugubina* and *Globoconusa daubjergensis* were searched for in the small (63–125 µm) size fraction but were not found. Common but very poorly preserved planktonic foraminifers in Sample 173-1068A-14R-CC are Maastrichtian in age. Although discernible as Cretaceous forms, they are indeterminate at specific or generic level.

Benthic Foraminifers

Calcareous benthic foraminifers in the size fraction of 125–500 µm are rare throughout the samples analyzed in Hole 1068A, excepting Samples 173-1068A-3R-CC and 173-1068A-5R-CC, in which they are common to abundant. However, well-preserved and abundant calcareous benthic foraminifers are generally present throughout these sediments in the small size fraction (63–125 µm) except for bar-

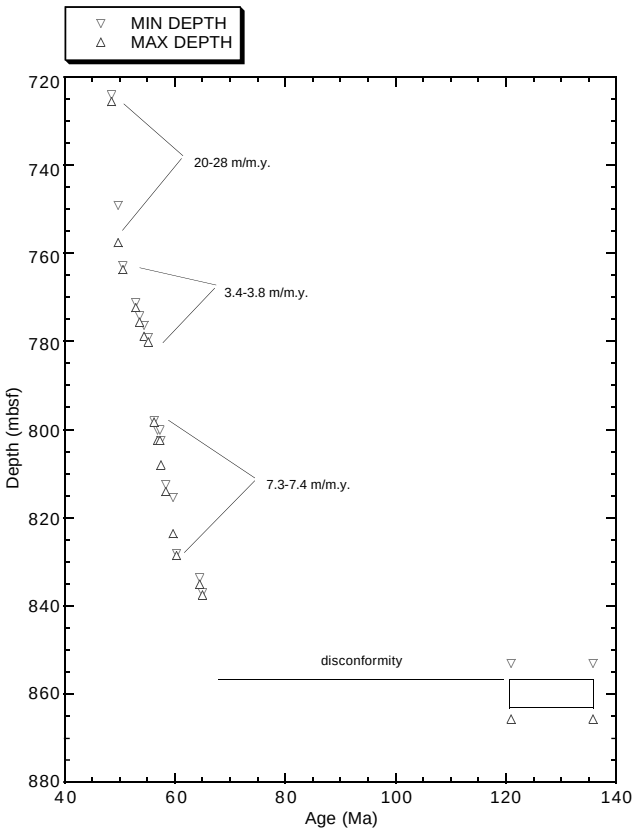

Figure 13. Age-depth plot for Site 1068 (see Table 3 for datums used).

Table 3. Calcareous nannofossil datums used to construct the age-depth plot in Figure 13.

Biozones		Biostratigraphic datums	Age (Ma)	Core, section, interval (cm)	Min. depth (mbsf)	Max. depth (mbsf)
CP12b	b	*R. inflata*	48.5	2R-3, 31-32	724.2	725.7
CP12a	b	*D. sublodoensis*	49.7	4R-CC, 30-33	749.2	757.7
NP12	t	*T. orthostylus*	50.6	6R-3, 121-123	762.9	763.8
CP10	b	*D. lodoensis*	52.9	7R-2, 60	771.3	772.4
CP9b	t	*T. contortus*	53.6	7R-5, 38	774.3	775.7
	b	*T. contortus*	54.4	7R-CC	776.4	778.9
CP9a	b	*R. cuspis*	55.2	8R-1, 30-31	779.2	780.2
CP8a	b	*D. multiradiatus*	56.2	10R-1, 20	798.1	798.3
CP7	b	*D. nobilis*	56.9	10R-2, 51-52	800.1	802.5
	b	*H. riedelii*	57.3	10R-2, 51-52	800.1	802.5
CP6	b	*D. mohleri*	57.5	10R-CC,1 4-16	802.5	808
CP5	b	*H. kleinpellii*	58.4	11R-4, 35	812.5	814.1
CP4	b	*F. tympaniformis*	59.7	11R-CC, 23-26	815.41	823.6
CP3	b	*E. macellus*	60.3	13R-7, 121-122	828.11	828.6
CP1b	b	*C. tenuis*	64.5	13R-5, 78-79	833.68	835.1
	t	Cretaceous spp.	65	14R-1, 52-54	837.1	837.5
	t	Valanginian	121	15R-5, 17	853	865.6
	b	Barremian	135.8	15R-5, 17	853	865.6

Note: b = bottom; t = top

ren intervals in Samples 173-1068A-4R-CC, 8R-CC, and 9R-CC and for rare occurrences in Sample 173-1068A-6R-CC. These size-sorted assemblages of smaller forms are considered to be allochthonous, redeposited turbidite material.

In Sample 173-1068-8R-CC, a relatively diverse assemblage of common agglutinated foraminifers is present and includes *Glomospira* spp., *Ammodiscus* spp., *Bathysiphon* spp., and *Haplophragmoides* spp. This assemblage is considered to be probably in situ, based on the diversity and preservation of the specimens recovered, and suggests sediment accumulation in a deep, probably abyssal depositional environment.

Calcareous Nannofossils

Within lithostratigraphic Unit II, all Cenozoic Okada and Bukry (1980) calcareous nannofossil zones are accounted for from Subzone CP12b (Zone NP14 of Martini, 1971) in Core 173-1068A-1R to CP1a (NP1) in Core 173-1068A-13R. The presence of *Micula prinsii* and *M. murus* in Core 173-1068A-14R help delineate the K/T transition within the first section of that core. Throughout the Tertiary interval, an ever-present but small number of Cretaceous taxa pervade the background of the assemblages, becoming numerous only as the K/T boundary is approached in Core 173-1068A-13R. *Nannoconus steinmannii* and related forms date the sedimentary breccia of Subunit IVA as Early Cretaceous (Valanginian to Barremian).

The general nannofossil assemblage compositions for the middle Eocene through uppermost Paleocene section at this site are similar to those enumerated for Site 1067 in Table 4, "Site 1067" chapter, this volume. At the top of the drilled section at Site 1068, calcareous nannofossils are abundant and quite well preserved within the micaceous claystones of Zone CP12b (NP14), the lower boundary of which lies between Samples 173-1068A-2R-3, 31 cm, and 2R-4, 33 cm. The FAD (first appearance datum) for *Pseudotriquetrorhabdulus inversus* is near the base of Section 173-1068A-2R-3, which corresponds closely to its position in Hole 1067A; thus, this seems to be a useful biostratigraphic datum in this region. CP12a (*Discoaster kuepperi* Subzone) extends downsection approximately to the juncture between Cores 173-1068A-4R and 5R. Diagenetic overgrowths, however, distort the shape and size of the lower zonal marker, *Discoaster sublodoensis*, and makes the placement of its FAD somewhat arbitrary. The consistently good preservation of delicate forms such as *Rhabdosphaera* along with the high diversity of these samples indicates deposition well above the CCD.

The base of the underlying *Discoaster lodoensis* Zone (NP12; ~CP11) was placed between Samples 173-1068A-6R-3, 33 cm, and 6R-3, 121 cm, based on the LAD (last appearance datum) of *Tribrachiatus orthostylus*, as prescribed by Martini (1971). Dark green and red claystones in Cores 1068A-4R and 5R were barren. Below that, however, Zone NP11 (CP10) was traced within the light brown and light green interbedded claystones to Sample 1068A-7R-2, 60 cm, which marked the FAD for *Discoaster lodoensis.* Preservation was best in the greenish sediments.

CP9b (NP11), the *Discoaster binodosus* Subzone, was confined to Sections 173-1068A-7R-3 and 7R-4; its lower boundary was placed between Samples 173-1068A-7R-4, 54 cm, and 7R-5, 38 cm. The latter sample contained *Tribrachiatus orthostylus, T. contortus*, and *T. bramlettei*, although virtually all specimens displayed calcite overgrowths that appeared glass-like in phase contrast light. This subzone was traced downsection tentatively to Sample 173-1068A-8R-1, 30 cm, although poor preservation made it difficult to distinguish between *T. bramlettei* and the closely related *Rhomboaster cuspis.* The low diversity of these assemblages, plus calcite overgrowths on the more dissolution-resistant forms, indicates that these are residual assemblages deposited close to the CCD.

The Paleocene *Discoaster multiradiatus* Zone (CP8; NP9) extends from Sample 173-1068A-8R-1, 133 cm, to the core catcher of Core 173-1068A-9R, based in part on the presence of *Discoaster mahmoudii* in the latter sample. As at Site 1067, this interval contains an exceptionally well preserved and diverse fasciculith assemblage dominated in size by *Fasciculithus tonii.*

Sample 173-1068A-10R-1, 20 cm, lacks *Discoaster multiradiatus* but *D. megastypus, Heliolithus kleinpellii, Fasciculithus tympaniformis,* and *F. bobii* are common, which together indicate upper Zone CP7 (NP8). This assignment is confirmed in Sample 173-1068A-10R-2, 51 cm, by the presence of *Discoaster noblis* (or *D. falcatus*),

Table 4. Distribution of planktonic foraminifers, Hole 1068A.

Age	Zone	Core, section	Depth (mbsf)	Abundance	Preservation	*Globigerina eocaena*	*Acarinina broedermanni*	*Acarinina soldadoensis*	*Morozovella aequa*	*Pseudohastigerina wilcoxensis*	*Morozovella aragonensis*	*Acarinina soldadoensis angulosa*	*Eoglobigerina eobulloides*	*Acarinina convexa*	*Globanomalina pseudomenardii*	Indeterminate spp.	Reworked
		173-1068A-															
middle Eocene		1R-CC	719.55	R	P											R	
early Eocene	P9	2R-CC	727.85	A	P	R	R	R		R	R					C	C
early Eocene	P9	3R-CC	740.43	R	P	R						R					
early Eocene		4R-CC	749.23	B													
early Eocene		5R-CC	757.71	A	P					R						C	
early Eocene		6R-CC	769.47	R	P											R	
early Eocene		7R-CC	776.41	A	P												A
early Eocene		8R-CC	788.75	B													
early Eocene		9R-CC	798.1	B													
late Paleocene	P4	10R-CC	802.52	C	P				R	R				R	R	C	
late Paleocene		11R-CC	815.41	B													
late Paleocene	P4	12R-CC	827.01	B													
early Paleocene		13R-CC	835.75	A	P								C				A
Maastrichtian		14R-CC	845.68	C	P											C	
Maastrichtian		15R-CC		B													

Heliolithus riedelii, and a fasciculith assemblage dominated by *F. bobii.*

Another barren interval occupies most of Section 173-1068A-10R-3, below which Sample 173-1068A-10R-CC is tentatively assigned to the *Discoaster mohleri* Zone (CP6; NP7) based on the presence of the nominate species. Below the ~5 m coring gap in Core 173-1068A-10R, the first four sections of Core 173-1068A-11R are assigned to the *Heliolithus kleinpellii* Zone (CP5; NP6). Large *H. kleinpellii* are abundant, but disappear abruptly in Section 173-1068A-11R-5, which, along with the core catcher, is assigned to the *Fasciculithus tympaniformis* Zone (CP4; NP5). In addition to the nominate species, Section 173-1068A-11R-5 contains very large *Fasciculithus ulii* and large *Coccolithus subpertusa* with bright, orange-yellow centers in polarized light. When isolated by dissolution, these centers superficially resemble helioliths. Rare discoasters in this sample and Sample 173-1068A-11R-4, 35 cm, are interpreted as contaminants.

Three samples from the first four sections of Core 173-1068A-12R were barren. Sample 173-1068A-12R-5, 35 cm, contained no *Fasciculithus tympaniformis* but did yield a few well-preserved *F. ulii,* which indicate the *Ellipsolithus macellus* Zone (CP3, NP4). This age determination was confirmed by the presence of well-preserved *Fasciculithus magnus* in Sample 173-1068A-12R-6, 35 cm, which could be traced downcore through Section 173-1068A-12R-7 to the core catcher. Sample 173-1068A-13R-1, 121 cm, contained no *F. magnus,* but did yield a single specimen of the basal zonal marker, *Eillipsolithus macellus,* along with common *Prinsius martinii* (which is sometimes used as a substitute marker for the base of Zone CP3), *Cruciplacolithus tenuis* (with "feet"), and common *Prinsius dimorphosus.* The latter become abundant in the subjacent Sample 173-1068A-13R-2, 20 cm, and its "bloom" can be traced downsection to Sample 173-1068A-13R-5, 78 cm, which also contains *Cruciplacolithus intermedius.* Together, these two taxa delineate Zones CP2 to CP1b, which are here combined because of difficulty in distinguishing *Chiasmolithus danicus,* the Zone CP2 lower boundary marker. The latter sample also contains the basal Tertiary marker taxon, *Biantholithus sparsus.*

Sample 173-1068A-13R-6, 52 cm is barren; however, Sample 1068A-13R-6, 69 cm, contains *Cruciplacolithus primus,* no *C. intermedius,* few to common *Braarudosphaera bigelowii* and numerous fragments of *Thoracosphaera operculata,* all of which are characteristic of Subzone CP1a (NP1). The latter two taxa increase in number downsection to the core catcher, which also contains sparse *Biantholithus sparsus* and a greater number of reworked Cretaceous taxa, including the Lower Cretaceous *Nannoconus steinmannii.* Most of the calcium carbonate in the sample is micrite.

At some other localities in this part of the world (e.g., Caravaca, Spain; Pont Labau, France; El Kef, Tunisia), *Braarudosphaera bigelowii* and/or *Thoracosphaera operculata* bloomed immediately after the K/T event (Pospichal and Wise, 1990). Their increased abundance above the boundary can indicate the presence of Tertiary strata. A K/T contact could not be distinguished in or above the first section of Core 173-1068A-14R amidst the interbedded dark brown hemipelagites and bioturbated turbidites, but could only be inferred by the numbers of *Braarudosphaera bigelowii* and *Thoracosphaera operculata.* These diminished downsection from Sample 173-1068A-14R-1, 8 cm, where fragments of the latter were abundant. The last *Braarudosphaera bigelowii* were noted in Samples 173-1068A-14R-1, 53 and 64 cm; none were present at 14R-1, 89 cm. Considering the effects of bioturbation, the K/T boundary could have originally lain between Cores 173-1068A-13R and 14R, or within the top 40 to 65 cm in the first section of Core 14R. The uppermost Cretaceous boundary markers, *Micula prinsius* and *M. murus* are noted in Sample 173-1068A-14R-1, 76 cm, indicating a near-complete biostratigraphic K/T transition even though the boundary itself was not preserved.

A substantial hiatus separates the uppermost Cretaceous sediments of Subunit IIC from the Lower Cretaceous breccias of lithostratigraphic Subunit IVA. These breccias are embedded within a pinkish cream-colored micritic matrix that contains trace numbers of dissolution-resistant nannofossils in all samples examined. Sample 173-1068A-15R-CC, for instance, contains *Nannoconus steinmannii, N. kamptneri, Cyclagelosphaera margerelii,* and large *Watznaueria barnesea.* A small green clast within the sample also contains *Nannoconus steinmannii,* indicating the incorporation of previously consolidated nannofossil ooze or chalk in this portion of the breccia.

Sample 173-1068A-15R-5, 114.5 cm, contained *Nannoconus bermudezi* in addition to *N. steinmannii.* In the next core downhole, Sample 1068A-16-1 (Piece 3) contained no nannoconids, but rather a slightly more varied nannoflora dominated by common to abundant

Cyclageiosphaera margerelii and *Watznaueria barnesea*, *Discorhabdus rotatorius*, *Zeugrhabdotus embergeri*, and *Cretarhabdus* spp.

Biostratigraphically, *Nannoconus steinmannii* ranges from the uppermost Tithonian through the Barremian, *N. bermudezii* ranges from the Valanginian through the Barremian, and *N. kamptneri* from the Valanginian through lower Aptian (Perch-Nielsen, 1985, fig. 44**)**. A tentative age for the breccia matrix of Valanginian to Barremian, therefore, can be derived from the nannoconid assemblage.

PALEOMAGNETISM

Archive halves of cores from Hole 1068A were measured at 5-cm intervals, using the pass-through cryogenic magnetometer. Sections were progressively demagnetized using peak alternating fields (AF) of 10, 20, 30, 40, 50, and 60 mT as described in the "Paleomagnetism" section, "Explanatory Notes" chapter (this volume). Sixty-eight discrete samples were progressively AF and thermally demagnetized to verify paleomagnetic reversals indicated in the sedimentary units and to determine directional stability of the basement rocks. Measurements of volume magnetic susceptibility were made at 3-cm intervals on most of the cores from Hole 1068A. Procedures are described in the "Physical Properties" section, "Explanatory Notes" chapter (this volume).

Common Magnetic Properties

Within the cored units, there are considerable variations in the magnetic properties of the various lithologies. The magnetic intensity (Fig. 14) and volume magnetic susceptibility (Fig. 15) of material recovered from Hole 1068A reflect the observed lithologic variations, with relatively low values in lithostratigraphic Subunit IIB, the middle part (about 780–820 mbsf) of Subunit IIC, and Subunit IVC. The most common feature, however, is a pervasive remagnetization (overprint) imparted by the coring process, characterized by NRM inclinations that are strongly biased toward the vertical (+90°). Shipboard AF and thermal demagnetization studies indicate that even at the highest AF demagnetization levels (up to 60 mT) not all of the drilling-induced remagnetization was removed, and that thermal demagnetization is generally more effective for removing this component. The effect of AF demagnetization, as shown in Figures 14 and 16, is a significant decrease in intensity and a shift toward shallower or negative inclinations for intervals with normal or reversed polarity, respectively.

Magnetostratigraphy

Results from the pass-through cryogenic magnetometer measurement indicate that a number of magnetic polarity reversals may be discerned on the basis of changes in sign of the inclinations of Cores 173-1068A-1R through 15R (711.3–855.9 mbsf). A total of 45 discrete paleomagnetic samples from these sediments were subjected to progressive AF or thermal demagnetization to verify the magnetostratigraphic results from the cryogenic magnetometer and to understand the magnetic behavior during stepwise demagnetization. Figure 17 illustrates the response to AF and thermal demagnetization for two samples from Subunit IIC. The relatively high stability shown by normally magnetized Sample 173-1068A-8R-1, 55–57 cm, and reversely magnetized Sample 173-1068A-7R-4, 86–88 cm, is characteristic

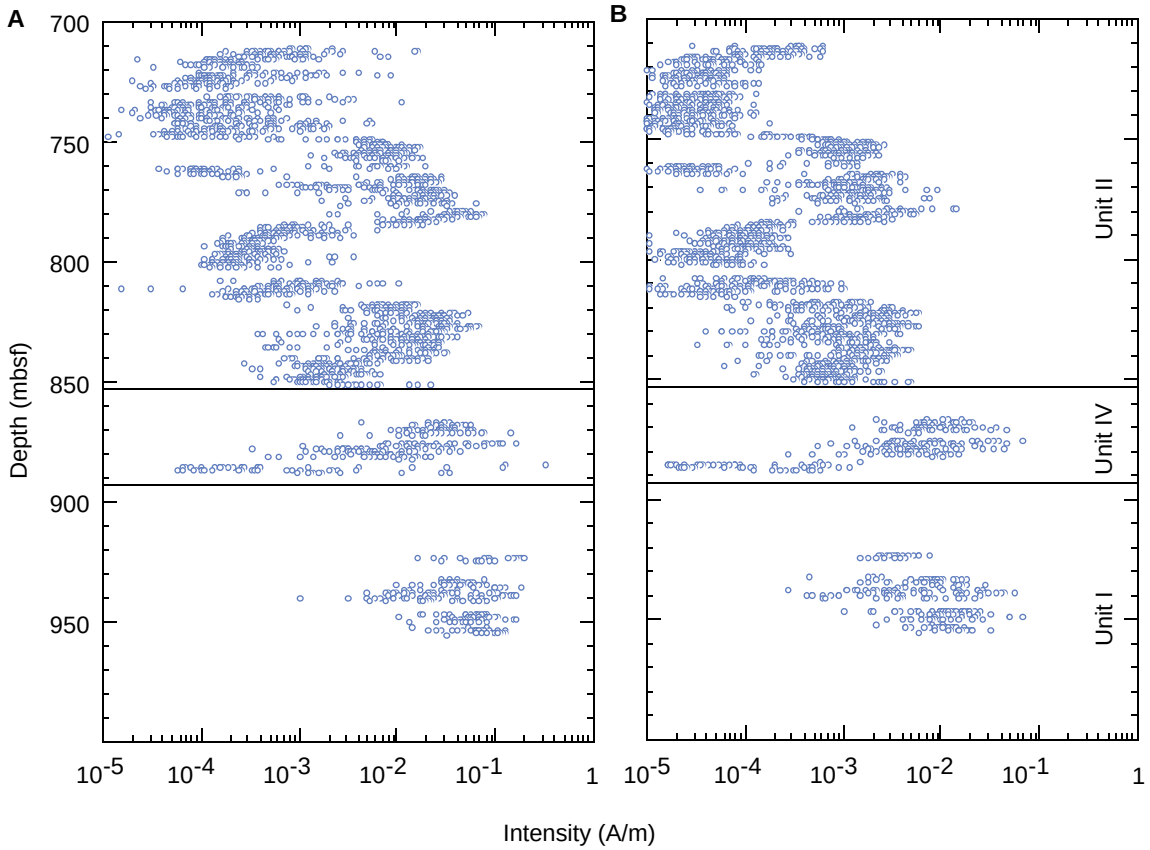

Figure 14. Remanent magnetization intensity (**A**) before and (**B**) after 60-mT AF demagnetization as a function of sub-bottom depth. AF demagnetization to 60 mT can effectively remove most of the drilling-induced magnetization as indicated by changes in intensity. Horizontal axis is a log scale.

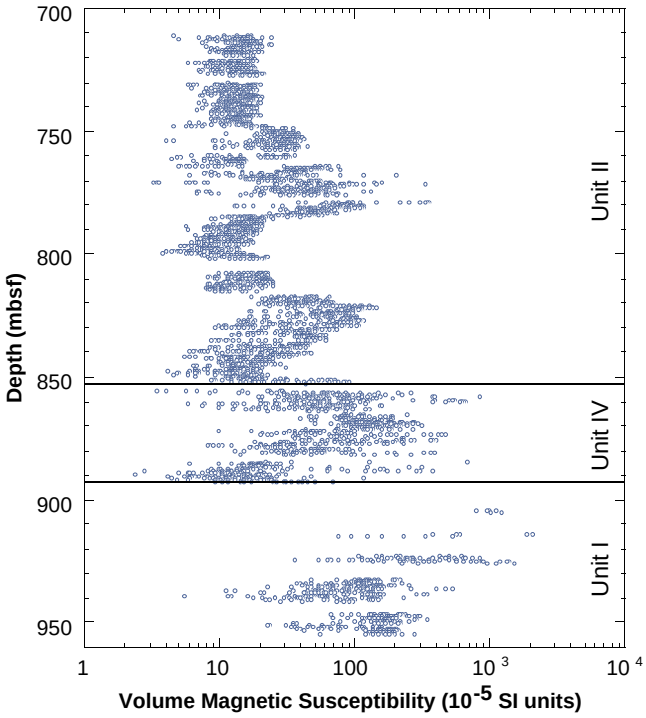

Figure 15. Downhole profile of magnetic susceptibility in Hole 1068A. Horizontal axis is a log scale.

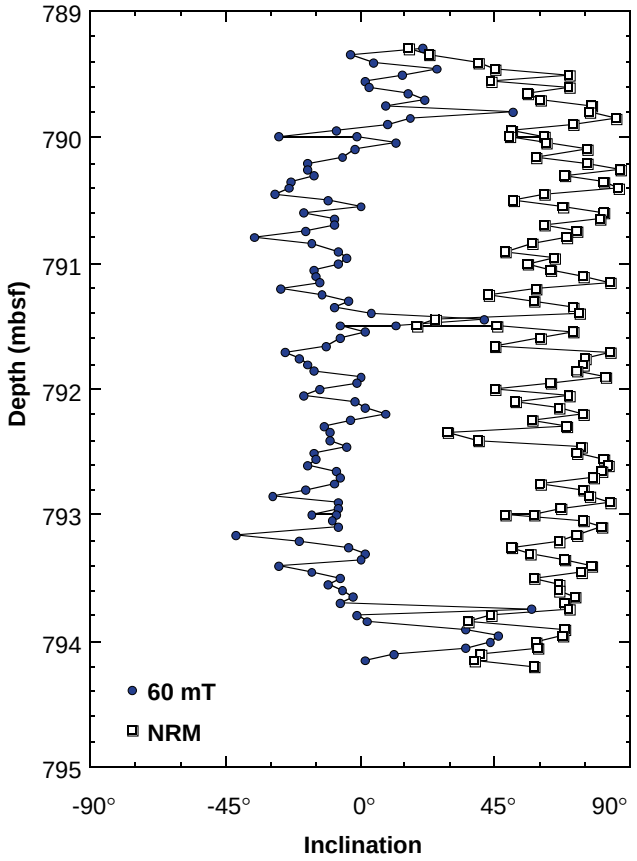

Figure 16. Plot of remanent inclination before (open squares) and after (solid circles) 60-mT AF demagnetization as a function of sub-bottom depth for Sections 173-1068A-9R-2 through 4. Upon demagnetization to 60 mT, a predominantly negative inclination was observed, suggesting that a drilling-induced magnetization is present.

of a high proportion of the samples from this subunit. These samples maintain an inclination close to the theoretically predicted value for the paleolatitude of this site, indicating they may represent the primary magnetization. As with most applications of magnetostratigraphy, one of the greatest problems is the correct matching of the observed sequence of magnetic polarity zones with the appropriate part of the magnetostratigraphic time scale (e.g., Berggren et al., 1995). Fortunately, available biostratigraphic data can assist in deciding which observed magnetic polarity zone or set of zones should be correlated with which magnetic chron on the polarity time scale. The combined biostratigraphic and paleomagnetic data suggest that the cored sediments span Chrons C29r–C21n and that the K/T boundary is within Core 173-1068A-14R-1 at a depth of 836 to 837 mbsf (Fig. 18).

Magnetic susceptibility and intensity measurements revealed sharp peaks in the brown sediment of Cores 173-1068A-6R through 8R (764.2–788.5 mbsf; Fig. 19). These peaks were verified by further measurements on corresponding discrete samples (locations of discrete samples are shown in Fig. 18). This characteristic brown bed and the associated peaks in NRM intensity and volume susceptibility, were also observed at nearby Sites 1067 and 900 (see "Paleomagnetism" section, "Site 1067" chapter, this volume; and Shipboard Scientific Party, 1994c) and appear to be synchronous at the three sites. Thus, this bed provides a proxy stratigraphic marker for correlation between the sedimentary records of the ocean/continent transition zone in the southern Iberia Abyssal Plain and the Cenozoic stratigraphic framework.

Magnetic Characterization of the Breccia and Serpentinite Units

The NRM intensities of the sedimentary breccias (Unit IV, "Lithostratigraphy" section, this chapter) range from ~1.0×10^{-4} to ~1.0×10^{-1} A/m (Fig. 14). Although the NRM intensity of the breccias is scattered, generally the values are higher at the top of the unit. In detail, intensity follows three trends: (1) from 855.9 through 875.2 mbsf, NRM intensities are higher, with a mean value ~2.5×10^{-2} A/m; (2) from 875.2 through 884.9 mbsf, intensities are scattered with a mean of 1.0×10^{-2} A/m; and (3) from 884.9 through 892.6 mbsf, intensities are much lower, averaging 1.5×10^{-3} A/m, and more scattered (Fig. 14). To a first order, the high and low intensity values in the downhole profile appear to coincide with petrographical boundaries in the unit (see "Lithostratigraphy" section, this chapter).

We conducted a conglomerate test on three oriented samples taken from clasts of gabbro, amphibolite, and the surrounding sedimentary matrix to test if the measured NRM from the matrix of the breccia unit was primary. The conglomerate test uses the randomness of magnetization directions to establish the stability of magnetization. If the directions of magnetization of the conglomerate clasts are random, then this suggests the magnetization of the parent formation (matrix) has been stable since the deposition of the conglomerate (Graham, 1949). As shown in Figure 20, the NRM directions of the three samples are quite different. Upon progressive thermal demagnetization, the demagnetization trajectory of the sediment matrix sample approximately followed a great circle and moved to a much shallower inclination, whereas the individual clasts retained their NRM directions. The result of this conglomerate test is positive, suggesting that the direction of magnetization of the sediment has been stable since the deposition of the conglomerate and that no strong overprint events have remagnetized the breccia unit.

The NRM intensity and volume susceptibility of the serpentinized peridotite unit (Unit 1, see "Igneous and Metamorphic Petrology"

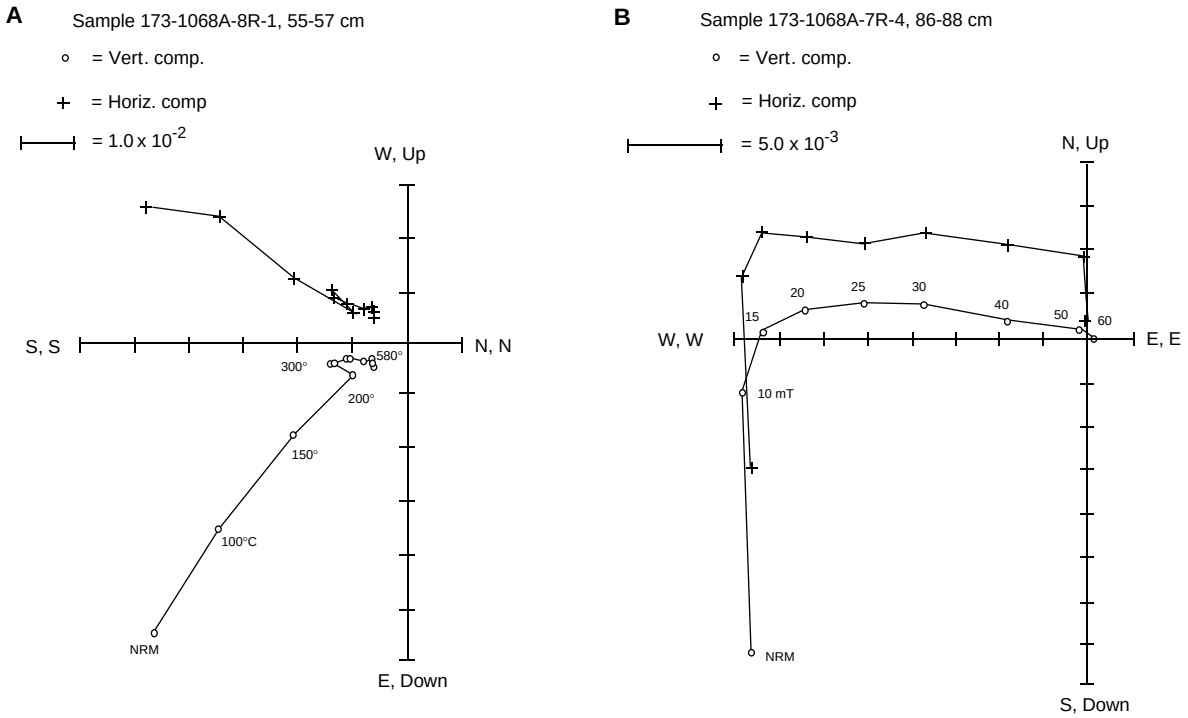

Figure 17. Representative vector end-point diagrams showing the results of (**A**) thermal demagnetization on the normally magnetized discrete Sample 173-1068A-8R-1, 55–57 cm, and (**B**) AF demagnetization on the reversely magnetized Sample 173-1068A-7R-4, 86–88 cm. Crosses and open circles represent the projection of the magnetization vector end points on the horizontal and vertical planes, respectively (note the declination values in this figure have not been corrected; see "Paleomagnetism" section, "Explanatory Notes" chapter, this volume).

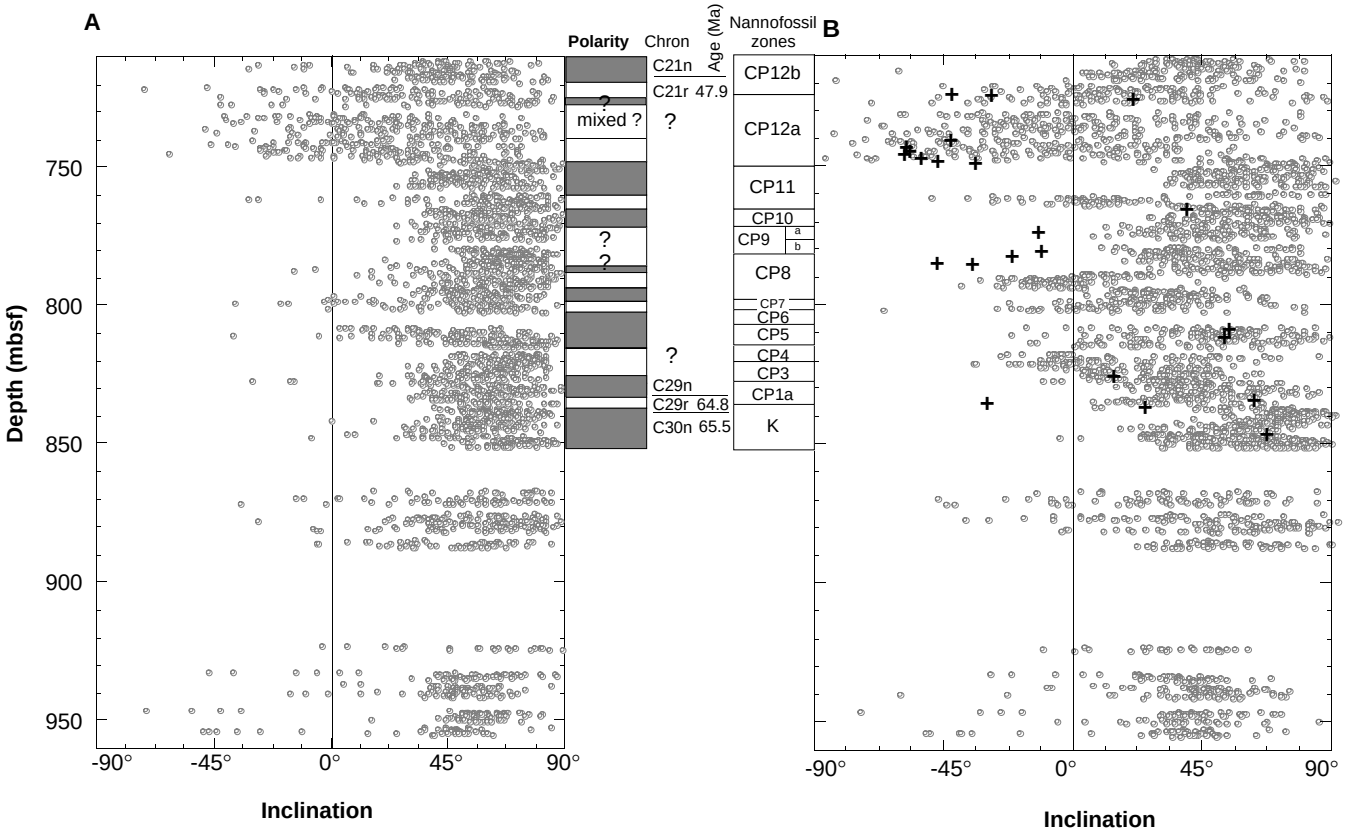

Figure 18. Downhole variation of magnetic inclination (**A**) before and (**B**) after 60-mT AF demagnetization, plotted with inferred polarity, geomagnetic chrons, and nannofossil biostratigraphic zones for Cores 173-1068A-1R through 15R. In the polarity column, normal polarity is indicated by black areas and reversed polarity is indicated by white areas. Discrete samples are shown by crosses.

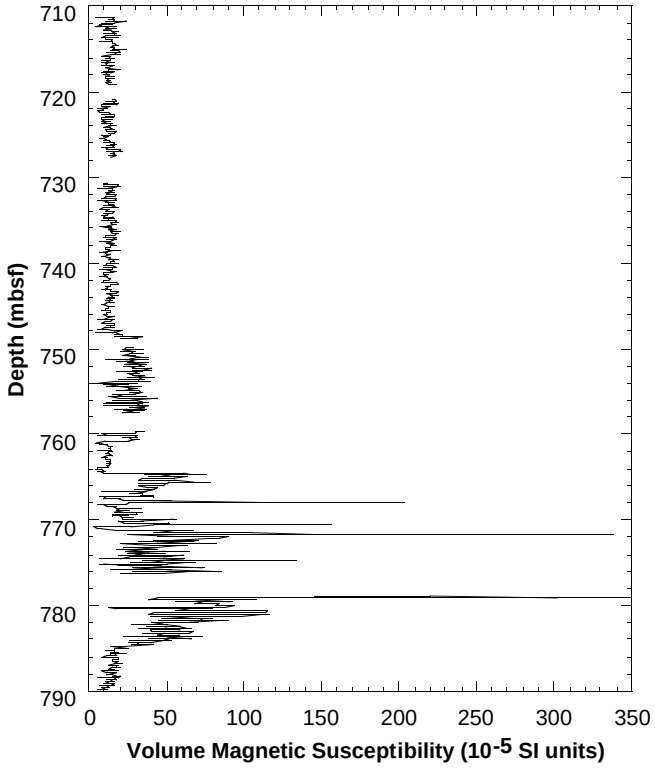

Figure 19. MST magnetic susceptibility measurements of Cores 173-1068A-1R through 8R. Several sharp peaks were revealed in the brown sediment of Cores 173-1068A-6R through 8R (764.2–788.5 mbsf).

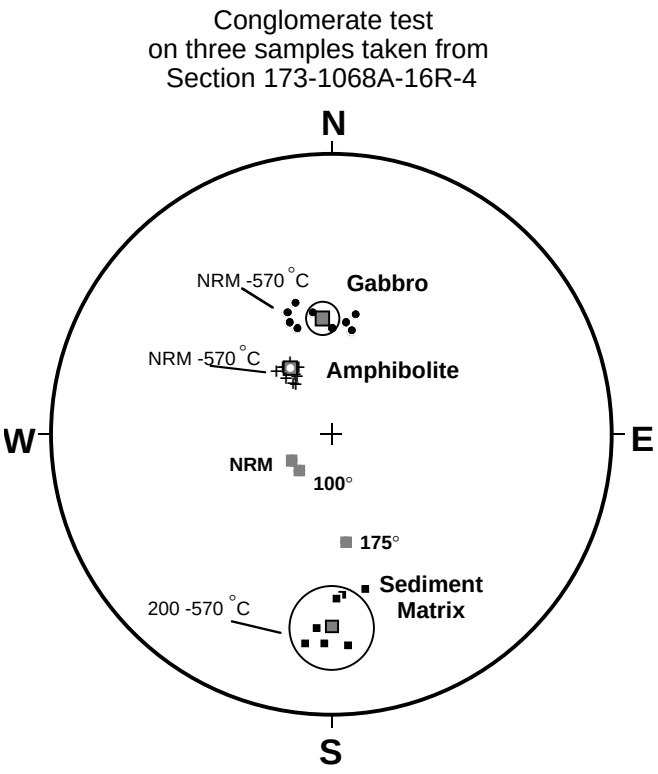

Figure 20. Equal angle (stereographic) projection showing the results of the conglomerate test (see text for explanation), lower hemisphere projection (note the declination values in this figure have not been corrected; see "Paleomagnetism" section, "Explanatory Notes" chapter, this volume).

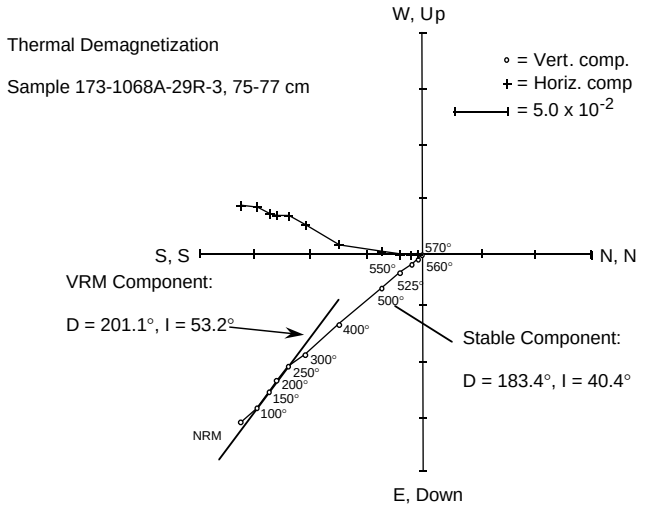

Figure 21. Vector end-point diagram of thermal demagnetization for discrete serpentinized peridotite Sample 173-1068A-29R-3, 75–77 cm. Viscous remanent magnetization component (VRM) and stable component of magnetization, both defined by the least-squares best fitting method, are indicated. Crosses and open circles represent the projection of the magnetization vector end points on the horizontal and vertical planes, respectively. D = declination, I = inclination (note the declination values in this figure have not been corrected; see "Paleomagnetism" section, "Explanatory Notes" chapter, this volume).

section, this chapter) have average values consistently above 15,000 $\times 10^{-5}$ A/m and 200×10^{-5} SI units, respectively, suggesting that these serpentinized peridotites are able to contribute significantly to the magnetic anomalies observed in the vicinity of Site 1068 and more generally in the ocean/continent transition. Although, in general, a stable component of magnetization can be identified by both AF and thermal demagnetization techniques, the removal of secondary magnetization was better accomplished through thermal demagnetization than through AF demagnetization. Progressive thermal demagnetization on several minicores of serpentinized peridotite revealed that a component of viscous remagnetization parallel to the present-day magnetic field has been recorded in these rocks, which can be used to reorient these cores azimuthally. As shown in Figure 21, thermal demagnetization of Sample 173-1068A-29R-3, 75–77 cm, removed a "soft" VRM component at low-temperature demagnetization steps (NRM = 300°C). Demagnetization from 300° to 566°C revealed the stable component of magnetization. It appears that there is no significant difference in demagnetization behavior of serpentinized peridotites through this part of the section, whether cores display a clear foliation or not. The dominant magnetic mineral in these rocks appears to be magnetite as indicated by the unblocking temperature and the coercivities.

The magnetically cleaned inclinations (mean = 42.9°, N = 17, α_{95} = 3.7°) in the serpentinized peridotites are systematically shallower than the inclination expected today (59°) at the drilling sites, but are statistically indistinguishable from the Jurassic–Cretaceous inclinations for Iberia (33.4°– 45.2°, α_{95} ~10°, see Van der Voo, 1969; Galdeano et al., 1989). Assuming the inclination represents the primary remanence at the time when these rocks were formed, the similarity between the observed and the expected inclinations is consistent with the notion that the drill sites were part of the Iberia plate at the time of acquisition of the magnetization.

IGNEOUS AND METAMORPHIC PETROLOGY

Acoustic basement cored in Hole 1068A consists of sedimentary breccias above serpentinized mantle peridotite. The lowermost breccia and uppermost serpentinite are variably tectonized. Breccia was first found in Section 173-1068A-15R-6 at 853.03 mbsf and serpentinite was first found in Section 173-1068A-20R-7 at 893.13 mbsf. The hole was terminated in serpentinite at 955.8 mbsf. Average recoveries were 86% in the breccia and 42% in the serpentinite. The recovery of serpentinite improved with depth, most notably in Cores 173-1068A-25R through 29R, each of which was recovered from a 4.8-m cored interval rather than the standard 9.7-m interval.

General Lithologic Description

Two units were delineated in the acoustic basement (Fig. 22). The breccias were defined as lithostratigraphic Unit IV (see "Lithostratigraphy" section, this chapter), and the serpentinite was defined as basement Unit 1. The reason for these definitions was to make clear the distinction between the acoustic basement (sedimentary breccia) and the petrologic basement (serpentinized upper mantle). Unit IV is divided into Subunits IVA and IVB based on matrix composition (see "Lithostratigraphy" section, this chapter), and Subunit IVC based on the degree of tectonic and/or hydrothermal overprint. In brief, Subunit IVA contains angular clasts of variably foliated amphibolite, metagabbro, and meta-anorthosite dominantly in a chalk matrix. Subunit IVB contains angular clasts of variably foliated amphibolite and metagabbro in a matrix of barren calcareous mud with fine-grained rock fragments. Subunit IVC contains similar clast lithologies that are variably fragmented in a variably cataclastic, fine-grained matrix of albite, chlorite, and calcite (see "X-ray Diffraction Studies" subsection, this chapter). Basement Unit 1 is divided into Subunits 1A and 1B based on the degree of tectonism. As far as can be ascertained from the limited core material (caused by low recovery of ~20%), Subunit 1A is a breccia, with clasts of serpentinized mantle peridotite supported by a fine-grained, cataclastic matrix that contains chlorite and serpentine minerals (see "X-ray Diffraction Studies" subsection). Subunit 1B consists of serpentinized peridotite. The extent to which original pyroxene and spinel can be recognized in hand specimen, albeit largely as pseudomorphs, increases with depth. Foliation, defined by alignment of pyroxene pseudomorphs and relict spinels, is strongest in the lower part of Unit 1.

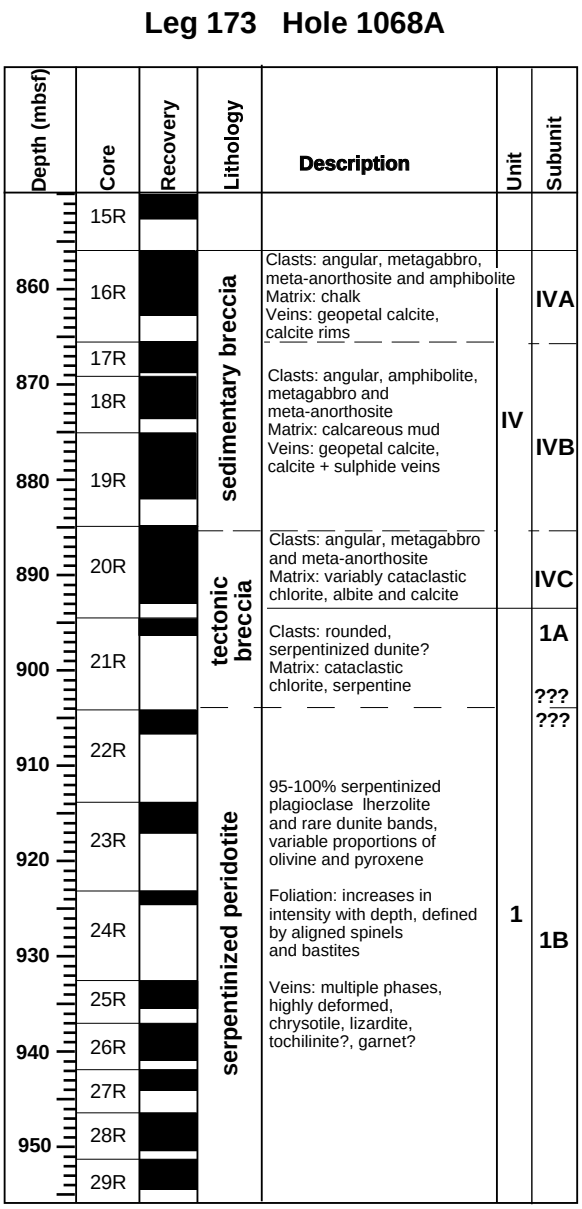

Figure 22. Summary of the lithologic basis for the definition of sedimentary Subunits IVA, IVB, and basement Subunit IVC and Unit 1.

Unit IV

Unit IV is divided into Subunits IVA (853.02–865.6 mbsf), IVB (865.6–884.9 mbsf), and IVC (884.9–893.13 mbsf). The rationale for defining Subunits IVA and IVB is based on the sedimentological characteristics of the matrix and is therefore discussed in detail in the "Lithostratigraphy" section (this chapter). This section focuses on describing (1) the petrology of clast lithologies and their distribution

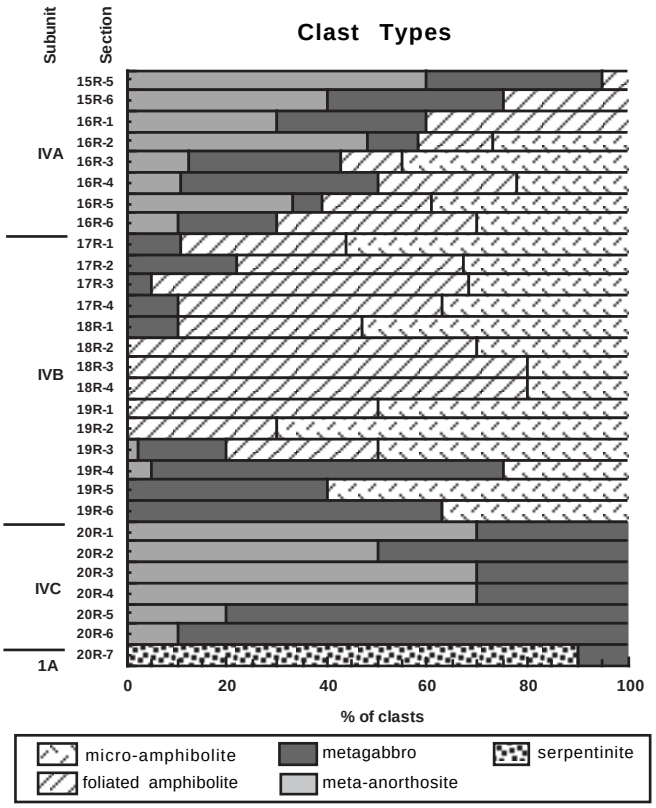

Figure 23. Cumulative plot of clast lithologies in lithostratigraphic Unit IV and basement Subunit 1A.

Table 5. Main mineralogical and textural characteristics of Hole 1068A rock types, based on petrographic evidence.

Core, section, interval	Rock type	Foliated textures	Unfoliated textures	Relict igneous textures	Cataclasite	Comments
173-1068A-						
Lithostratigraphic Unit IV						
15R-5 (Piece 10, 71-75 cm)	Meta-anorthosite			Anorthosite		Chlorite veins
15R-5 (Piece 12, 88-93 cm)	Meta-anorthosite			Anorthosite		Calcite veins
15R-6 (Piece 1, 10-14 cm)	Metagabbro			Metagabbro		Epidote veins
15R-6 (Piece 3, 29-31 cm)	Breccia: meta-anorthosite, metagabbro			Anorthosite/metagabbro		Calcite veins and calcite matrix
15R-6 (Piece 4, 40-43 cm)	Breccia: meta-anorthosite	Meta-anorthosite				Calcite veins and calcite matrix
15R-6 (Piece 5, 52-56 cm)	Foliated metatonalite	Metatonalite				Calcite veins
16R-1 (Piece 5C, 66-68 cm)	Foliated amphibolite	Amphibolite				
16R-2 (Piece 9B, 115-119 cm)	Foliated amphibolite	Amphibolite		Metagabbro		Chlorite veins and thin shear zone
16R-3 (Piece 4, 106-111 cm)	Metagabbro			Metagabbro		Plagioclase, calcite, and epidote veins
16R-5 (Piece 3B, 63-68 cm)	Foliated micro-amphibolite	Micro-amphibolite				
16R-5 (Piece 5, 91-95 cm)	Breccia: leucocratic metagabbro and amphibolite	Amphibolite		Leucocratic metagabbro	Breccia	
16R-6 (Piece 1B, 30-33 cm)	Metagabbro			Metagabbro		Calcite veins
17R-2 (Piece 1A, 1-6 cm)	Foliated amphibolite	Amphibolite				Epidote veins
17R-4 (Piece 1A, 26-28 cm)	Leucocratic metagabbro			Leucocratic metagabbro		Calcite veins
17R-4 (Piece 1B, 76-80 cm)	Breccia: amphibolite, epidosite, chloritite	Amphibolite				Calcite veins and calcite matrix
17R-4 (Piece 1B, 85-89 cm)	Breccia: leucocratic metagabbro					Calcite veins and calcite matrix
18R-2 (Piece 10, 135-139 cm)	Micro-amphibolite		Micro-amphibolite			Plagioclase veins
18R-4 (Piece 4, 60-64 cm)	Foliated amphibolite	Amphibolite				
18R-4 (Piece 6, 97-101 cm)	Breccia: foliated amphibolite	Amphibolite		Metaleucogabbro		Calcite veins and matrix
19R-3 (Piece 1E, 100-105 cm)	Metagabbro	Metagabbro		Metagabbro		
19R-4 (Piece 1B, 23-27 cm)	Breccia: metagabbro and amphibolite			Metagabbro		Calcite veins and breccia matrix
19R-4 (Piece 1C, 56-60 cm)	Breccia: metagabbro			Metagabbro		Calcite veins and breccia matrix
19R-4 (Piece 3, 130-135 cm)	Foliated amphibolite	Amphibolite				Calcite veins
20R-1 (Piece 3D, 77-78 cm)	Breccia: leucocratic amphibolite	Leucocratic amphibolite				
20R-5 (Piece 4, 57-60 cm)	Metasomatized anorthosite or leucocratic metagabbro	Leucocratic metagabbro		Leucocratic metagabbro		Tremolite and prehnite veins
Basement Unit 1						
20R-7 (Piece 5, 56-59 cm)	Breccia				Breccia	Extensively chloritized, serpentine veins
20R-7 (Piece 7A, 82-85 cm)	Serpentinized dunite (70%), peridotite (30%)				Breccia	Serpentine veins
22R-1 (Piece 9A, 75-78 cm)	Serpentinized peridotite (dunite?)			Serpentinized peridotite		Serpentine veins
23R-1 (Piece 3C, 28-32 cm)	Serpentinized peridotite			Serpentinized peridotite		Serpentine veins
24R-1 (Piece 3H, 71-75 cm)	Foliated serpentinized plagioclase peridotite	Serpentinized plagioclase peridotite		Serpentinized plagioclase peridotite		Serpentine veins
24R-2 (Piece 4A, 57-61 cm)	Foliated serpentinized plagioclase peridotite	Serpentinized plagioclase peridotite		Serpentinized plagioclase peridotite		Serpentine veins
25R-2 (Piece 8A, 96-100 cm)	Serpentinized plagioclase peridotite			Serpentinized peridotite		Serpentine veins
25R-3 (Piece 3, 43-47 cm)	Serpentinized peridotite			Serpentinized peridotite		Serpentine veins
25R-3 (Piece 8B, 116-120 cm)	Serpentinized peridotite	Serpentinized peridotite		Serpentinized peridotite		Serpentine veins
26R-1 (Piece 2, 11-14 cm)	Foliated serpentinized peridotite	Serpentinized peridotite		Serpentinized peridotite		Serpentine veins
26R-1 (Piece 4B, 120-124 cm)	Foliated serpentinized lherzolite	Serpentinized lherzolite		Serpentinized lherzolite		Serpentine veins
26R-2 (Piece 1B, 51-56 cm	Serpentinized plagioclase peridotite	Serpentinized plagioclase peridotite				Serpentine veins
26R-4 (Piece 2B, 45-48 cm)	Foliated serpentinized plagioclase lherzolite	Serpentinized plagioclase lherzolite		Serpentinized plagioclase lherzolite		Serpentine veins
28R-2 (Piece 1, 42-46 cm)	Serpentinized plagioclase lherzolite	Serpentinized plagioclase lherzolite		Serpentinized plagioclase lherzolite		Serpentine veins
28R-3 (Piece 1B, 2-5 cm)	Serpentinized plagioclase lherzolite	Serpentinized plagioclase lherzolite				Serpentine veins
28R-CC	Serpentinized plagioclase lherzolite			Serpentinized plagioclase lherzolite		
29R-3 (Piece 1C, 62-66 cm)	Foliated serpentinized plagioclase lherzolite	Serpentinized plagioclase lherzolite		Serpentinized plagioclase lherzolite		Serpentine veins
29R-3 (Piece 1F, 99-103 cm)	Foliated serpentinized plagioclase lherzolite	Serpentinized plagioclase lherzolite		Serpentinized plagioclase lherzolite		Serpentine veins

throughout the cores, (2) the evidence for subsequent deformation and fluid-rock interaction affecting the lowermost part of Unit IV, and (3) the rationale for defining Subunit IVC.

The distribution of major clast lithologies in the breccias (Unit IV and the uppermost part of Subunit 1A) is shown in Figure 23. Four major clast types were identified in Unit IV aided by thin section observations, which are listed in Table 5. These are (1) foliated amphibolite, (2) micro-amphibolite, (3) metagabbro, and (4) meta-anorthosite. Micro-amphibolites are distinguished from the other rock types on the basis of their macroscopic similarity to microgabbros and their finer grain size compared to the foliated, medium-grained amphibolites. Additional minor clast lithologies include epidosites, various fine-grained metabasic rocks, and, in the uppermost part of Subunit IVA, rare exotic clasts (e.g., biotite schist). Metagab-

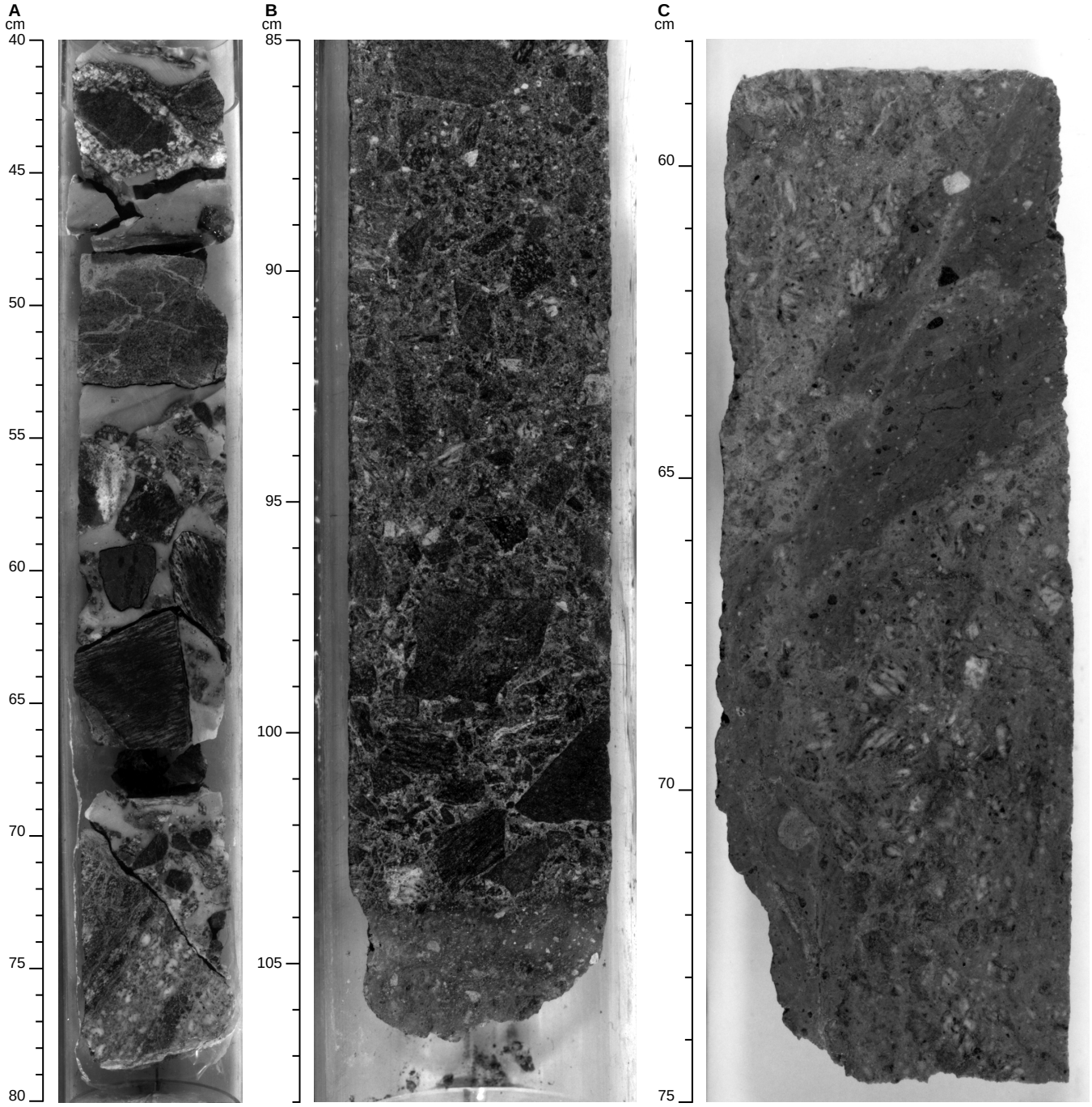

Figure 24. Typical breccias. **A.** Subunit IVA showing angular clasts of metagabbro, meta-anorthosite and amphibolite in a chalk matrix (Sample 173-1068A-16R-1, 40–80 cm). **B.** Subunit IVB showing angular clasts of amphibolite in a calcareous matrix (Sample 173-1068A-17R-2, 85–108 cm). **C.** Subunit IVC showing fragmented angular clasts of metagabbro and meta-anorthosite in a chlorite, calcite, albite matrix (Sample 173-1068A- 20R-1, 58–75 cm). Note oblique, chlorite-rich cataclasite zone in the upper half of the photograph.

bro and meta-anorthosite clasts dominate the upper and lower parts of Unit IV, which roughly correspond to Subunits IVA and IVC (Fig. 24). Foliated amphibolite and micro-amphibolite clasts dominate the middle part of Unit IV, which roughly corresponds to Subunit IVB (Fig. 24).

Clasts are typically angular and <1 to 6 cm in diameter, although clasts as much as 17 cm in diameter occur in the uppermost part of the unit. Typical metagabbro clasts contain 50%–60% plagioclase, 35%–50% amphibole and pyroxene, and 5% epidote. Leucocratic metagabbros have 70%–90% plagioclase, 5%–25% amphibole and pyroxene, and 5% epidote. They are medium- to coarse-grained (<1 to 6 mm) and are commonly foliated. Some clasts show a mylonitic foliation, reminiscent of the flaser gabbros that were described at Site 900 (Cornen et al., 1996a). In hand specimen, crystals are generally anhedral and elongated parallel to the foliation. Meta-anorthosite occurs as discrete clasts or as patches and layers in larger clasts of metagabbro. Typical meta-anorthosite clasts contain ≥90% equigranular coarse crystalline (1 to 5 mm) plagioclase with ≤10% fine-grained (<1 mm) platy chlorite, granular epidote, amphibole, and/or pyroxene. Typical micro-amphibolite clasts contain 50%–70% plagioclase and 30%–50% amphibole. They are finer grained (<1 mm) and variably foliated. Crystals are equant or elongated parallel to foliation. Typical foliated amphibolite contains 60% amphibole and 40% plagioclase. In Section 173-1068A-15R-6, foliated amphibolite clasts also contain small amounts of chlorite. They are medium grained (1 to 3 mm) and, almost without exception, strongly foliated. Crystals are anhedral and elongated parallel to the foliation.

The percentage of matrix is plotted as a function of depth in Figure 25, which shows that matrix increases from 20%–30% at the top of Unit IV (~853 mbsf) to a maximum of 70%–80% at the base of Subunit IVB (~885 mbsf) and then decreases to 40% at the base of Subunit IVC (~893 mbsf). The increased percentage of matrix with depth observed in Figure 25 is accompanied by a gross reduction in clast size and frictional rounding of clasts. Jigsaw breccias are first observed from Core 173-1068A-18R (869.2–875.2 mbsf). Oblique bands of cataclasite are first observed in Section 173-1068A-19R-1 (875.2 mbsf) and increase in size and frequency, down through Cores 173-1068A-19R and 20R, above Subunit 1A. Geopetal structures, formed on the underside of clasts (see "Lithostratigraphy" section, this chapter), and observed sporadically in Cores 173-1068A-15R through 18R, are visibly "fed" by calcite ± sulfide veins in interval 173-1068A-19R-1, 85–111 cm, and surpassed in abundance by these calcite ± sulfide veins in Cores 173-1068A-19R and 20R. The matrix of Cores 173-1068A-19R and 20R is banded, pale green and yellowish brown. It is rich in chlorite, albite, and calcite (identified by XRD). These observations, which are indicative of cataclastic deformation and fluid-rock interaction, form the basis for ascribing Cores 173-1068A-19R and 20R (above Subunit 1A) to Subunit IVC.

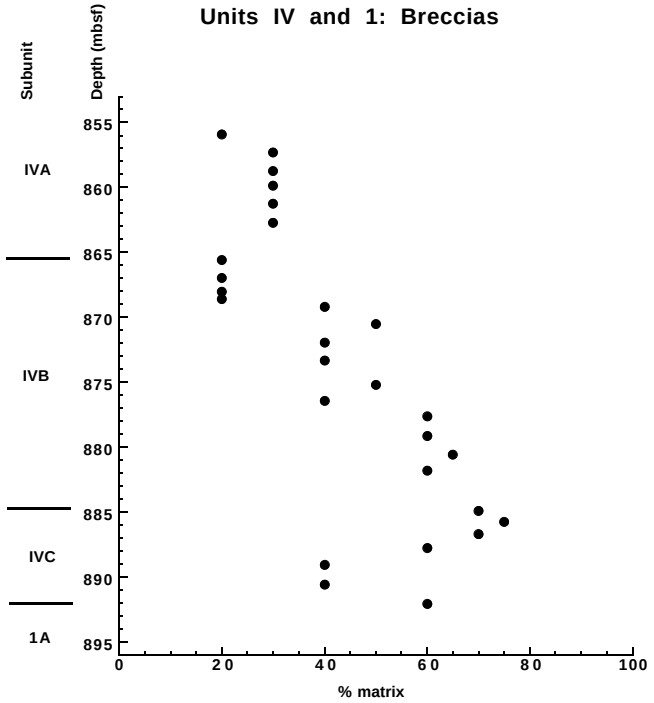

Figure 25. Percentage of matrix in Unit IV breccias from visual estimates and core-scan images, plotted as a function of depth.

Unit 1

Unit 1 is divided into Subunits 1A (893.13–904.2 mbsf) and 1B (904.2–955.8 mbsf) based on the degree of brecciation. Subunit 1A is a breccia, which differs from Subunits IVA–IVC in that it contains clasts of serpentinized mantle peridotite and chrysotile-rich vein material (Fig. 23). These clasts are rounded, 1 to 5 cm in diameter, and contain 100% serpentine replacing >95% olivine and <5% pyroxene. They are supported by a fine-grained, cataclastic matrix that contains chlorite and serpentine minerals, indicative of greenschist- to subgreenshist-facies conditions during breccia formation. The clasts and matrix are crosscut by shallowly inclined anastomosing veins that contain serpentine minerals (observed in thin section).

Recovery in Subunit 1A and the uppermost part of Subunit 1B was poor, therefore the exact position of the contact is difficult to ascertain. However, Core 173-1068A-23R contains discrete pieces of serpentinite with similar orientation, and Core 173-1068A-24R contains long continuous pieces. Subunit 1B is characterized by variably foliated, intensely veined serpentinized peridotite (Fig. 26).

In hand specimen (Sample 173-1068A-25R-1 [Piece 9A, 73–75 cm]), it is possible to distinguish (1) 1- to 5-mm bastite pseudomorphs replacing original pyroxenes, (2) <2-mm relict spinels, with pale chlorite rims possibly replacing original plagioclase rims, and (3) a black <<1-mm crystalline serpentine matrix that replaces original olivine (Fig. 27). The serpentine matrix weathered to a dark yellowish orange within 24 hr of recovery, the weathering product being partly soluble in 10% HCl. Pseudomorphed pyroxenes occur throughout the cores, although their abundance varies. In addition to these general fluctuations, narrow (5–10 cm) bands of dunite are observed in intervals 1068A-25R-1, 110–115 cm, and 26R-1, 0–10 cm. Relict spinels with white rims of chlorite, interpreted as pseudomorphs after plagioclase, occur throughout the core. However, locally their distribution is patchy. Similar textures were observed on Leg 149 at Site 897 (Shipboard Scientific Party, 1994a).

Foliation in the serpentinized peridotite is strongest in Cores 173-1068A-25R through 29R. However, this might be, in part, a preservation artifact because these cores were the least brecciated and weathered and the best recovered.

Serpentinization is pervasive throughout Unit 1, affecting 90%–95% of the peridotite protolith, and extends into the lowermost clasts (and matrix?) of Unit IV. Veins are ubiquitous throughout Unit 1 and their geometries are everywhere complex and record several stages of fluid migration. The earliest stages that can be recognized in hand specimen are characterized by <0.1-mm veins of fibrous dark green chrysotile and/or platy dark green lizardite(?), which often crosscut one another and are commonly contained within later broad (2–10 mm) pale green-blue veins, which are identified as microcrystalline serpentine in thin section. The earlier veins are crumpled, folded, thrusted, and pulled apart within the later veins, presumably reflect-

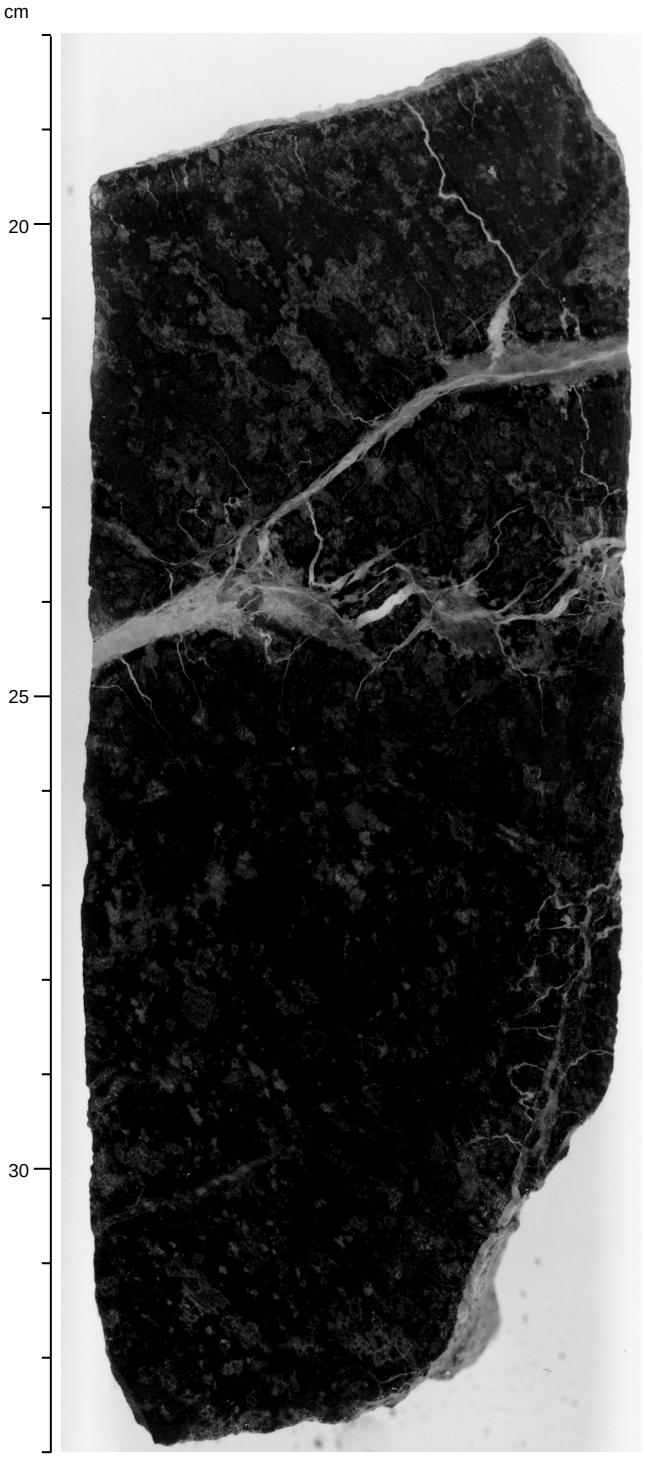

Figure 26. Typical serpentinized peridotite from Subunit 1B, showing (1) variable foliation defined by alignment of bastite (after pyroxene) and relict spinels rimmed by chlorite (after plagioclase), and (2) branching veins of serpentine minerals (interval 173-1068A-27R-3, 18–33 cm).

ing the internal stresses imposed by the positive volume change that accompanies serpentinization (see "Structural Geology" section, this chapter).

Petrography

This section documents the salient petrographic characteristics both of the metamorphic and igneous rock types that occur as clasts within Unit IV and of the serpentinized peridotite in Unit 1. Six major petrographic subdivisions are recognized, on the basis of mineralogy: amphibolites, metagabbros, meta-anorthosites, metatonalites, chloritized metabasites, and serpentinized peridotites (Table 5).

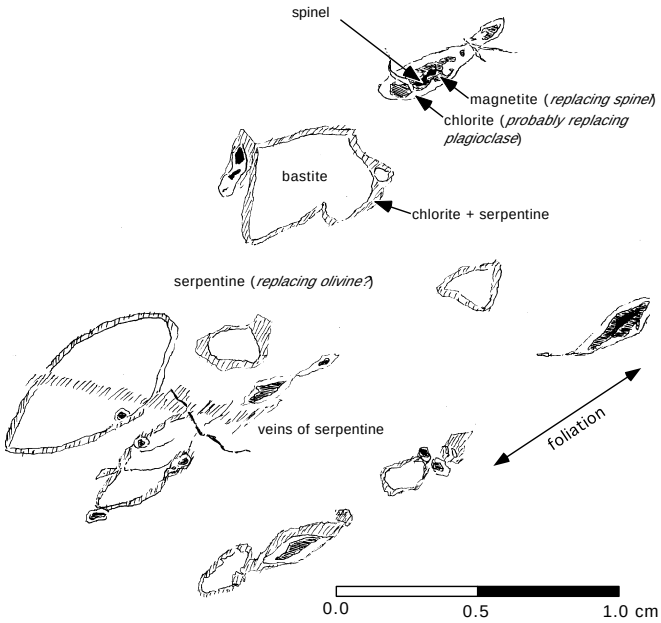

Figure 27. Drawing of split core face illustrating hand specimen evidence for the protolith mineralogy of the basement Unit 1 serpentinite (Sample 173-1068A-25R-1 [Piece 9A, 73–75 cm]). Trace of foliation plane is indicated.

Unit IV: Amphibolite Clasts

The commonest meta-igneous clast type is amphibolite, which includes micro-amphibolites and foliated and unfoliated varieties. The clasts are comprised of essential plagioclase and greenish brown amphibole, each composing between 40% and 60% of the rock. Ilmenite (with hematite exsolution lamellae and pyrrhotite) also occurs, along with relict clinopyroxene and trace apatite in several samples. Lower grade minerals occur in variable abundance and include epidote and chlorite.

With the exception of a single micro-amphibolite clast examined microscopically, the amphibolites show a variably developed foliation, which is defined by elongate banded concentrations of plagioclase and green-brown amphibole. The plagioclase is mainly andesine and shows extensive recrystallization and a well-organized interlocking triple junction network (Fig. 28). Relict porphyroclasts (as much as 3 mm long) show sweeping extinction and are commonly mantled by arrays of neoblasts. Similar textures are observed within the foliated micro-amphibolites where plagioclase occurs as a fine-grained groundmass and as porphyroclasts (~1.2 mm), which show sweeping extinction and marginal recrystallization to small neoblasts (e.g., Sample 173-1068A-19R-4 [Piece 3, 130–135 cm]).

The microstructural characteristics of the amphiboles vary from sample to sample, ranging from strained crystals elongated in the foliation plane (e.g., Sample 173-1068A-17R-2 [Piece 1A, 1–6 cm]), to aggregates that are elongated parallel to the foliation but show random orientations of individual crystals. In the latter case, most amphiboles appear unstrained (e.g., Sample 173-1068A-17R-4 [Piece 1B, 76–80 cm]). The unfoliated micro-amphibolite (Sample 173-1068A-18R-2, 135–139 cm) contains sparse plagioclase phenocrysts (~1.0 mm), a fine-grained amphibole-plagioclase–rich groundmass, and shows a granular texture of equidimensional plagioclase. Amphiboles are unstrained, anhedral, and randomly oriented.

All varieties of amphibolite show, to greater or lesser extent, a nonpervasive overprint of epidote ± chlorite veining, with associated localized alteration of plagioclase and amphibole. In some instances, epidote and chlorite veins are subparallel to the foliation (e.g., Sample 173-1068A-17R-2 [Piece 1A, 1–6 cm]). In such examples, amphibole and plagioclase show localized microfracturing.

Unit IV: Metagabbro Clasts

Four clasts of unfoliated hypidiomorphic-textured metagabbro were examined microscopically. The essential mineralogy consists of ~30% clinopyroxene, 40% plagioclase (labradorite), 30% brown amphibole, and trace ilmenite. Sample 173-1068A-15R-6 [Piece 1, 10–14 cm], differs in that it has more abundant clinopyroxenes and less abundant amphiboles than the other three clasts. The plagioclase is frequently zoned, shows inhomogeneous undulatory extinction, and a subophitic relationship with clinopyroxenes. Small anhedral lenses of ilmenite are interstitial to both phases, and are occasionally separated from clinopyroxenes by brown hornblende. The metagabbros show a partial transition to randomly oriented interlocking granoblastic textures, which resemble those present within the amphibolites. This texture consists of small equigranular plagioclase crystals, locally showing pronounced triple junctions and interlocking green-brown amphiboles. Small quantities of amphibole also occur as discrete oriented blebs within clinopyroxene; the blebs form patterns suggestive of pseudomorphed exsolution lamellae. In common with the amphibolites the metagabbros show, to variable extent, replacement by epidote, chlorite, and sericite. Also, in places there is an overprint of locally anastomosing ferric-iron oxyhydroxide veins that project inward from the clast-matrix interfaces.

One metagabbro examined microscopically shows weathered olivine poikilitically enclosed in clinopyroxene (Sample 173-1068A-17R-4 [Piece 1B, 76–80 cm]). Where olivine and plagioclase are in contact, the altered plagioclase contains biotite and hornblende intergrowths, and adjacent plagioclase has abundant green inclusions (probably spinel) arranged parallel to crystallographic directions. These relationships are interpreted as corona textures, formed between olivine and plagioclase as the gabbro cooled.

Two clasts of foliated brown to green-brown amphibole-bearing (~20% mode) leucocratic metagabbros were identified (Samples 173-1068A-17R-4 [Piece 1A, 26–28 cm], and 173-1068A-17R-4 [Piece 1B, 85–89 cm]). The foliation is defined by discontinuous lenses of strained and variably chloritized amphiboles or pyroxenes. Plagioclase crystals are small (<1.5 mm), variably strained, and recrystallized to fine new grains along grain boundaries. Opaque minerals occupy interstitial spaces throughout the plagioclase dominated groundmass and also occur as discrete lenses, that lie adjacent to amphiboles and are elongated parallel to the foliation.

Unit IV: Meta-anorthosite Clasts

Two samples of meta-anorthosite were examined. They are coarsely crystalline (grain size ≤6 mm), and composed of ~98% plagioclase, with accessory pyrrhotite, ilmenite, clinopyroxene, and metamorphic sphene. The plagioclase shows limited marginal recrystallization and sporadic undulatory extinction. In Sample 173-1068A-15R-5 [Piece 10, 71–75 cm], the plagioclase is predominantly unaltered and dissected by limited numbers of chlorite veins. In contrast, Sample 173-1068A-15R-5 [Piece 12, 88–93 cm], shows extensive sericitization, which increases in intensity with proximity to calcite veining, and clast-matrix interfaces. In addition, some plagioclase crystals show albitized margins adjacent to calcite-plagioclase interfaces.

Unit IV: Metatonalite Clasts

One clast of foliated metatonalite was examined in thin section (Sample 173-1068A-15R-6 [Piece 5, 52–56 cm]). The rock consists

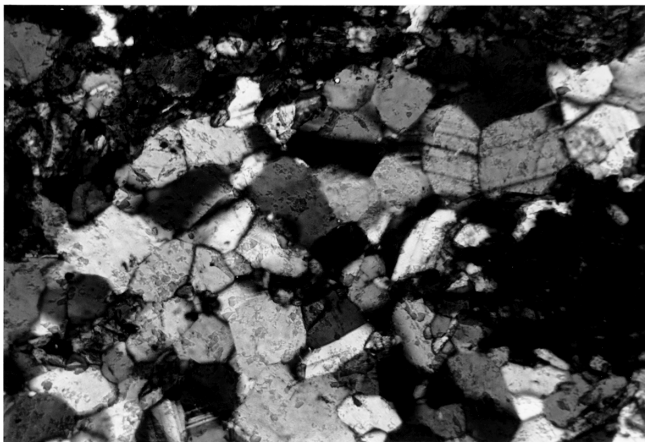

Figure 28. Photomicrograph of plagioclase neoblasts with well-developed triple junctions within an amphibolite clast. Base of photomicrograph = 1.25 mm; cross polarized light (Sample 173-1068A-17R-4, 56–59 cm).

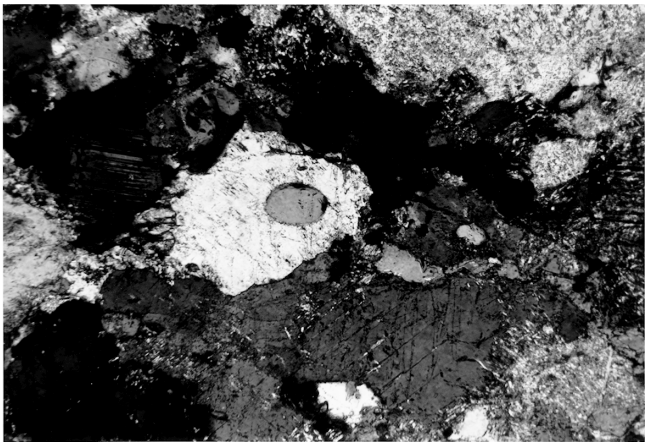

Figure 29. Photomicrograph showing deformed metatonalite. Note the poikilitic inclusion of quartz (gray) within plagioclase crystal (white) in the center of the photomicrograph. Base of photomicrograph = 1.25 mm, cross polarized light (Sample 173-1068A-15R-6, 52–56 cm).

of essential plagioclase, with accessory quantities of quartz, amphibole, and chlorite, and with trace concentrations of zircon and apatite. The foliation is defined by the preferred orientation of plagioclase porphyroclasts and neoblasts, all of which exhibit undulatory extinction (Fig. 29). Quartz occurs as poikilitic inclusions within plagioclase and as a discrete interstitial phase. The fabric is intermittently disrupted by grain boundary films and fractures filled with undeformed calcite, and by lesser quantities of chlorite and quartz. Plagioclase is variably altered to sericite and also sporadically replaced by epidote.

Unit IV: Chloritized Metabasite

Clasts from the lowermost part of the Unit IV breccia (Subunit IVC) are pervasively chloritized metabasite, which show anastomosing chlorite and serpentinite veining closest to the contact (e.g., Sample 173-1068A-20R-7 [Piece 5, 56–59 cm]). The only surviving relict phases are small anhedral clinopyroxenes, surrounded by chlorite (± serpentinite), and epidote that is variably overgrown by chlorite (Fig. 30). Chlorite shows variable birefringence, and crystallite

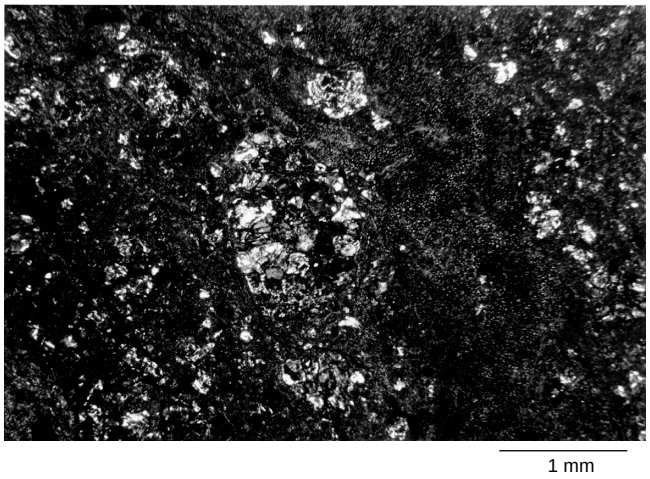

Figure 30. Photomicrograph showing chloritized metabasite cataclasite. Base of photomicrograph = 5 mm; cross polarized light (Sample 173-1068A-20R-7, 56–59 cm).

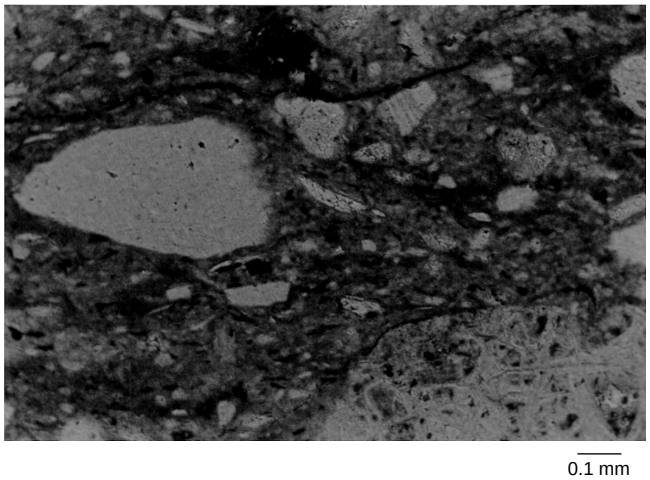

Figure 31. Photomicrograph showing foliation in serpentinite cataclasite. The foliation is defined by preferred orientation of clasts. Base of photomicrograph = 1.25 mm; plane polarized light (Sample 173-1068A-20R-7, 82–85 cm).

sizes ranging from acicular to fibrous, to very fine-grained patches (see "X-ray Diffraction Studies" subsection, this chapter). The different physical and optical properties of the chlorites appear to delineate relict outlines of clasts. In some instances, such "ghost margins" show the selective development of a wall-lining fibrous phase on exterior margins of protoliths. Some of these "ghost clast" morphologies are similar to those encountered within serpentinite cataclasites (discussed below).

Unit 1: Serpentinized peridotite

The serpentinized peridotites consist of 80%–95% serpentine group minerals (chrysotile and lizardite) forming mesh textures after olivine and bastites after pyroxene. Less than 10% chlorite (some of which may be chromium-rich) is present and commonly surrounds chrome spinel in a replacement of plagioclase and also as part of pyroxene pseudomorphs. Magnetite, ferric-iron oxide/oxyhydroxides, and in a few cases relict anhedral clinopyroxene (e.g., Sample 173-1068A-26R-1 [Piece 4B, 120–124 cm]; and Sample 173-1068A-29R-3 [Piece 1C, 62–66 cm]) and tremolite (Sample 173-1068A-29R-3 [Piece 1C, 62–66 cm]) are also present in these samples. Several of the serpentinized peridotites also contain vein-hosted wairakite, analcime, and small clasts of garnet within friable serpentinite (see "X-ray Diffraction Studies" subsection).

The principal textural attribute of the serpentinized peridotites is arrays of mesh cells of serpentine. These contain minute blebs of magnetite that are interwoven with serpentine minerals, forming discrete linear trails, irregular banded patterns, and more or less random disseminated aggregates within mesh cell interiors. The mesh cell interiors show a variety of optical properties, ranging from continuous sweeping extinction to discontinuous mottled extinction. The planar arrays of apparent fibers that delineate mesh cell edges range in orientation from normal to subparallel to mesh cell edges.

The mesh cell textural patterning is variably crosscut by serpentine veins, which range up to 5 mm in width, are locally anastomosing, and show a variety of morphologies and crosscutting relationships. These serpentine veins commonly contain banded optically distinct fibrous and platy layers. These layers are variably disrupted by fold-like structures and a series of discontinuities across which individual bands appear to be offset or truncated. The serpentinite breccia and lizardite-chrysotile cataclasite (Sample 173-1068A-20R-7, [Piece 7A, 82–85 cm]) show a variety of mesh-cell textures, with associated serpentinite veining, within individual clasts. In addition, smaller lenticular blocks of serpentinized peridotite set within a finer grained matrix of serpentinite show a strong tendency to be flattened about larger clasts, forming a weak foliation (Fig. 31).

Figure 32. Photomicrograph, showing holly-leaf textured spinels, surrounded by pale chlorite, set within mesh-textured serpentinite matrix. Note that the elongation of the spinel and surrounding chlorite define a relict high-temperature foliation. Base of photomicrograph = 1.25 mm; plane polarized light (Sample 173-1068A-29R-3, 62–66 cm).

Spinels are yellowish to reddish brown, subhedral to anhedral (holly-leaf to vermicular) in form, and show a common preferred orientation within some thin sections (Sample 173-1068A-25R-3 [Piece 2, 11–14 cm]). Grain boundaries are frequently decorated by concentrations of magnetite. Commonly, adjacent to these, or in direct contact with spinels, are microdomains of variable size, which contain bladed randomly orientated aggregates of chlorite (Fig. 32). Similar textural relationships were observed between spinels and plagioclase in peridotites recovered from Sites 897 and 899 (Leg 149), which

suggests that the chlorite may have replaced primary plagioclase. Apple green and colorless chlorites also occur in association with serpentine group minerals, forming optically distinct domains that mimic the previous position, and cleavage disposition, of pyroxenes.

The spatial distribution, and comparative abundance, of bastite-rich microdomains compared to mesh-textured serpentine-rich microdomains, coupled with the preservation of trace clinopyroxenes within some sections (e.g., Sample 173-1068A-29R-3 [Piece 1C, 62–66 cm]), suggest the previous existence of differing ultramafic protoliths. These include dunites and spinel peridotites (e.g., Sample 173-1068A-26R-1 [Piece 2B, 45–48 cm]). In other cases, there is no way of deciding with any certainty whether bastite has replaced clinopyroxene or orthopyroxene. The textural interrelationships between bastites (after pyroxenes) and mesh-textured serpentinites (after olivines) is also instrumental in defining a relict foliation in several thin sections (e.g., Sample 173-1068A-26R-4 [Piece 2B, 45–48 cm]).

Discussion

Hole 1068A contains breccias that consist of a range of intrusive meta-igneous clast types, the majority of which have experienced high- to low-grade metamorphic events. These clasts are cemented by a calcite-rich cement and overlie serpentinized peridotite. The contact between the breccias and serpentinized peridotite is tectonized (see "Structural Geology" section, this chapter), and clasts within this tectonized zone are extensively chloritized. The clasts of Hole 1068A fall into the same basic categories that were established for the basic and leucocratic lithologies from Hole 1067A. Beyond systematic nomenclature, the rock types show a range of petrographic features that serve to distinguish the two sites. Perhaps the most marked protolith-dependent petrographic difference is the lesser abundance of zircon and apatite at Site 1068, which points to different compositions of the original magma or contamination processes by host rocks at the two sites. Unaltered clinopyroxene, absent in Site 1067 samples, occurs in a number of metagabbro clasts from Site 1068, and several samples (e.g., Samples 173-1068A-16R-4 [Piece 1B, 30–33 cm, and Piece 1C, 56–60 cm]) show original igneous textures.

Meta-igneous rocks from both sites show a nonpervasive, more or less static, greenschist facies metamorphic overprint upon an amphibole-bearing higher temperature fabric. However, beyond that, similarities are limited. The marked differences in the rheological response of plagioclase to deformation, and marked reduction in recrystallized grain size at Site 1068, compared to Site 1067, points to an upper amphibolite to granulite facies dynamic metamorphism at Site 1068 and higher strain and differential stress. In contrast, the textures of the Site 1067 amphibolites are consistent with less strain, probably at lower temperatures (i.e., middle to lower amphibolite facies conditions).

The foliated amphibolites of Site 1068 are also distinguished by the fact that individual amphiboles within foliated bands are occasionally randomly oriented across the entire sample and show little if any evidence of strain. At the same time, plagioclase shows well-developed triple junctions, plastic strain, and flattening parallel to the foliation. These textural attributes suggest that, at least in some instances, the amphiboles may be pseudomorphs after pre-existing deformed mafic phases, perhaps overprinting granulite-facies pyroxene-bearing assemblages, similar to those encountered at Site 900 (Leg 149).

It is important to stress that some clasts of the Site 1068 amphibolites do contain extensive petrographic similarities to Site 1067 amphibolites, whereas others show textures and inferred grades of metamorphism akin to those encountered at Site 900. These considerations imply that, although generalized differences in the metamorphic evolution do exist between the three sites, the rock types are unlikely to be genetically divorced in origin.

Perhaps the most striking petrographic features of the breccias are the presence of pervasively chloritized metabasite, which shows anastomosing chlorite and serpentinite veining, the near-complete obliteration of clast assemblages, and the retention of relict exterior outlines that are represented by optically distinct wall linings of fibrous mineral phase(s). These physico-chemical features point to the passage of heated hydrothermal metasomatizing fluids through the lowermost sections of the breccias.

The presence of serpentinite cataclasite in close proximity to the chloritized metabasite breccia, coupled with the propagation of anastomosing serpentine veins upward from the serpentinite, points to a serpentinized upper mantle provenance for the fluids. Such an interpretation necessitates uplift and exposure of highly fractured peridotite that was subjected to pervasive serpentinization. It is suggested that fluids involved in the serpentinization of peridotite exited through the overlying breccia and this led to extensive chlorite alteration and localized serpentine and tremolite veining, particularly at the base of the breccia. It is also possible that the serpentinization processes are associated with the generation of methane gas (Charlou and Douval, 1993; see "Organic and Inorganic Geochemistry" section, this chapter).

X-ray Diffraction Studies

X-ray diffraction (XRD) studies of the breccias and serpentinites focused on (1) the fine-grained matrix of the breccias (Cores 173-1068A-15R through 20R) and (2) veins within the serpentinites. In addition, one calcite-rich vein from the breccia and one whole-rock sample from each of the hydrothermally altered breccia and the serpentinite were analyzed. The mineralogy of the breccias and serpentinites is summarized in Tables 6 and 7. All XRD analyses were conducted without the incorporation of an internal standard. An anomalous peak, apparently metallic Fe, was present in all samples (including red clays from the overlying Eocene sediments) and is attributable to contamination during the crushing process. All results reported here are strictly qualitative.

Subunit IVA: Breccia Matrix

The matrix of the upper breccia (Subunit IVA) consists largely of calcite. In addition to the calcite, Sample 173-1068A-15R-6 (Piece 3, 28–30 cm), appears to contain small amounts of plagioclase (possibly andesine) and chlorite. Sample 173-1068A-16R-1 (Piece 4, 37–38 cm) may contain a trace of sericite.

Subunit IVB: Breccia Clasts and Matrix

Samples from Subunit IVB include breccia matrix from Cores 173-1068A-17R, 18R, 19R, and 20R (Table 6). Calcite is an important constituent and produces the strongest peak in all samples except Samples 173-1068A-17R-2 (Piece 2, 104–105 cm), and 18R-3 (Piece 8, 81–82 cm), where plagioclase predominates (Fig. 33). Plagioclase is found in all samples and is abundant in all but the calcite vein Sample 173-1068A-19R-1 (Piece 3, 93–94 cm). Where present, the principal plagioclase peak at 3.19 °2θ is several times stronger than any other plagioclase peak (e.g., Fig. 33), suggesting that the plagioclase is Na-rich (probably albite). The characteristic chlorite peaks at 7 and 14 °2θ (Fig. 33), as well as subordinate chlorite peaks, occur in all samples except the calcite vein. The presence of amphibole is inferred on the basis of peaks ranging from 8.37 to 8.5 °2θ (Fig. 33) and subordinate peaks. Amphibole is absent and quartz is present in Sample 173-1068A-18R-3 (Piece 9, 130–131 cm). The presence of hy-

Table 6. X-ray diffraction mineralogy of Hole 1068A breccia samples from lithostratigraphic Subunit IVB.

Core, section, interval (cm)	Color	*Albite	Calcite	Chlorite	Amphibole	"FeOH"	"Other"
173-1068A-							
17R-2, 105-105	Red?	Max	Vs	S	W	Yes	Ankerite?
18R-1, 25-26	Green	Vs	Max	M	M	No	
18R-3, 81-82	Green	Max	Vs	S	M		
18R-3, 130-131	Green	Nmax	Max	S		No	Quartz
18R-4, 54-55	Olive	Max	Max	S	M	Yes	
18R-4, 96-97	Red-brown	Vs	Max	S	M		
19R-1, 93-94**	White	W	Max			No	Unk. peak
19R-5, 56-57	Yellow-green	Vs	Max	S			
20R-1, 51-52	Green	S	Max	Vs		No	Quartz
20R-2, 54-55	Pale green	Nmax	Max	Vs		No	Quartz, analcime

Notes: * Peak intensities: max = biggest peak; nmax = nearly as intense as the maximum peak; vs = very strong; s = strong; m = moderate; w = weak. All "FeOH" and "other" peaks are weak. **Sample 19R-1, 93-94 cm, is a calcite vein containing an unknown ore mineral. Unknown peak at 2.85 °2θ.

Table 7. X-ray diffraction mineralogy of Hole 1068A serpentinites and veins from basement Unit 1.

Core, section, interval (cm)	Lizardite	Chrysotile	Chlorite	Tochilinite	Other	Comments
173-1068A-						
20R-7, 62-63	Max	S				Vein/cataclasite, peaks broad, low intensity partly amorphous?
21R-2, 65-66	Max	S		W		Pale gray-green vein
21R-2, 131-132	Max	S				Pale blue vein
21R-2, 138-139	Max	S	S	S	Calcite (w), heazlewoodite?	Serpentinite with bronze coating
22R-1, 44-45	Max	S	W		Calcite (w)	Green vein
22R-1, 134-135	Vs	Max?				Green, foliated vein
22R-2, 32-33	Max	S	S	Vs	Brucite, godlevskite	Serpentinite
22R-2, 71-72	Vs	Max?		W	Calcite (w)	Serpentine vein
24R-1, 19-20	Vs	Max?	W		Godlevskite Brucite?	Vein
24R-1, 110-112	Max?	Vs			Garnet	Light green vein
24R-2, 63-67	Max	S	W		Godlevskite?, brucite?	Surface scraping
25R-1, 56-57					Ugrandite garnet	Brown-green crystal essentially pure
26R-1, 134-135	S	Max?				Light-green vein
26R-2, 111-112	Max	Vs				Light-green vein
28R-2, 123-124	S?	Max?				Light-green vein
28R-3, 2-3	S	S			Garnet max	Blue part of zoned blue-to-green vein

Note: Peak intensities: max = strongest, s = strong, w = weak, vs = very strong.

drated, ferric iron oxide (inferred from goethite peaks) correlates fairly well with observed color. It is absent from the vein and absent or only questionably present in the green samples. It is always present or questionably present in the reddish, brownish, and yellowish samples (Table 6). Finally, Sample 173-1068A-17R-2 (Piece 2, 104–105 cm), contains a recognizable peak characteristic of either dolomite or ankerite (Fig. 33). Because subordinate dolomite peaks were not found and because ankerite lacks any strong subordinate peaks, the mineral is tentatively identified as ankerite.

Subunit IVC: Breccia Clasts and Matrix

Two samples (173-1068A-20R-1 [Piece 3, 51–52 cm], and 20R-2 [Piece 2, 54–55 cm]) were analyzed from this highly fractured and locally cataclastic (see "Structural Geology" section, this chapter) subunit of the breccia. Sample 173-1068A-20R-1 (Piece 3, 51–52 cm), is from a dark-green vein-like or cataclastic structure. Calcite peaks are the strongest, but albite and chlorite are also abundant. A small quartz peak is present, and no clear amphibole peaks were detected. Sample 173-1068A-20R-2 (Piece 2, 54–55 cm), is a whole-rock sample from the highly altered, pale green portion of the breccia in Core 20R. All of the minerals found in Sample 173-1068A-20R-1 (Piece 3, 51–52 cm), also occur in Sample 173-1068A-20R-2 (Piece 2, 54–55 cm), although the albite peak is of approximately the same strength as the calcite peak. In addition, Sample 173-1068A-20R-2 (Piece 2, 54–55 cm), contains a series of lines (e.g., at 5.58, 3.43, 2.91, 2.68, and 1.73 °2θ), absent in all other samples, interpreted as the mineral analcime ($NaAlSi_2O_6 \cdot H_2O$; Fig. 33).

Unit IV: Discussion

The abundance of chlorite and albite, minerals generally scarce or absent in the breccia clasts (and, in particular, subordinate to more calcic plagioclase and hornblende) suggests substantial diagenetic or hydrothermal modification of the breccia matrix. In Samples 173-1068A-20R-1 (Piece 3, 51–52 cm), and 18R-3 (Piece 9, 130–131 cm), both of which are dark green and highly altered, amphibole is entirely absent and quartz is present. This suggests that throughout much of the breccia unit the diagenetic/alteration assemblage is albite + chlorite and that calcic plagioclase and amphibole are unstable during diagenesis/alteration. In addition, the matrix-transforming process may precipitate quartz under some circumstances. Calcite is present in all samples and may have been stable throughout the alteration/diagenesis of the breccias; it appears to have been part of the early diagenetic cement in the breccias (i.e., the microfossiliferous calcite in Subunit IVA). In addition, calcite appears to be part of the stable assemblage during the late diagenetic/alteration event, as seen from its presence in even the most highly altered rocks (e.g., Sample 173-1068A-20R-2 [Piece 2, 54–55 cm]) as well as veins and late drusy cements. Identification of an unknown oxide or sulfide mineral in a calcite vein (Sample 173-1068A-19R-1 [Piece 2, 93–94 cm]) will have to await more detailed analysis onshore.

Of particular interest is the presence of analcime (along with the assemblage noted above) in Sample 173-1068A-20R-2 (Piece 2, 54–55 cm), probably the most hydrothermally altered breccia sample examined by XRD. This mineral is common in hot spring deposits (e.g., Yellowstone) and in hydrothermally altered basalts and sediments

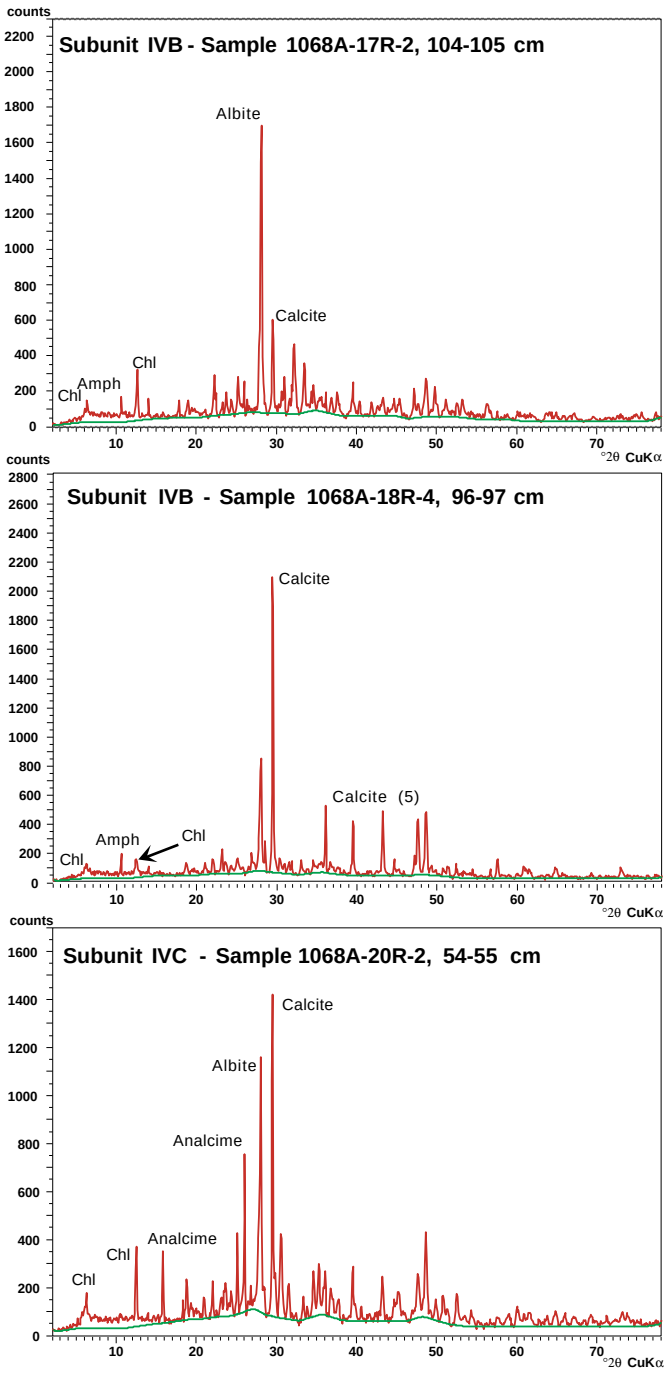

Figure 33. X-ray diffraction patterns from the breccia in Subunit IVB.

(Deer et al., 1993). Its presence strongly suggests hydrothermal circulation in the Hole 1068A breccias.

Unit 1: Serpentinized Peridotite

One sample of serpentinite and 14 samples of veins within serpentinite were analyzed by XRD. The mineralogy of the massive serpentinite and of most of the veins is similar and (with a few exceptions dominated by garnet; see below) consists mostly or entirely of lizardite and chrysotile (Table 7).

Both lizardite (identified by the large peak at 2.50°2θ) and chrysotile (identified by a series of peaks around 2.6, 2.45, and 2.09°2θ) occur in all samples (except Sample 173-1068A-25R-1 [Piece 8, 56–57 cm]; see below; Fig. 34). Antigorite was not found. Additional minerals found in one or more samples include chlorite, calcite, and brucite. The unusual mineral tochilinite {II-4FeS·3[(Mg, Fe)$(OH)_2$]} was found in several samples and yielded strong peaks at 5.45 and 10.9 °2θ in Samples 173-1068A-21R-2 (Piece 1, 138–139 cm) and 22R-2 (Piece 1, 32–33 cm; Fig. 34). An unknown variety of garnet, probably in the ugrandite group, was found as brownish, broken fragments in Sample 173-1068A-25R-1 (Piece 8, 56–57 cm; Fig. 34). Additionally, a strong spectrum similar to the latter garnet was found in a sample consisting dominantly of the bluish portion of a zoned blue to green vein in Sample 173-1068A-28R-3 (Piece 1, 2–3 cm). The rare nickel sulfides heazlewoodite (Ni_3S_2) and/or godlevskite (Ni_7S_6) have been tentatively identified in several samples (Table 7).

Unit 1: Discussion

The XRD spectrum of Sample 173-1068A-20R-7 (Piece 5, 62–63 cm), a sample taken from a vein or zone of strong cataclasis near the sediment/serpentinite contact, was of low intensity and yielded broad and, sometimes, anomalous peaks. In thin section, this material can be seen to be largely isotropic and it may be, in part, amorphous or extremely finely crystalline. Tochilinite may form by reaction of serpentine with an Fe-bearing sulfide phase, but very little information relative to this mineral was available shipboard. Calcite is rare in the Hole 1068A serpentinites relative to serpentinites found on Leg 149, in the upper part of Holes 899B, 897C, and 897D (Sawyer, Whitmarsh, Klaus, et al., 1994; Gibson et al., 1996b). The presence of brucite suggests that fluids in the serpentinite were poor in CO_2. Ramdohr (1980) suggests that heazlewoodite and godlevskite may form by the breakdown of pentlandite, or, alternatively, from the Ni component in olivine in the presence of a relatively S-poor fluid. The exact composition and significance of the garnet is unknown at this time but it is probably hydrothermal in origin. The garnet reported in peridotite on land in the Galicia area belongs to the pyralspite series and is distinct from garnet found in Site 1068 serpentinite (Girardeau and Gil-Ibarguchi, 1991).

Major and Trace Element Geochemistry

Unit IV: Breccia Clasts

Samples from eight representative clasts from the Unit IV sedimentary breccia of Hole 1068A were chosen for shipboard whole-rock X-ray fluorescence (XRF) analysis. Unit IV clast types include metagabbro, micro-amphibolite, amphibolite, and meta-anorthosite. The metagabbros and amphibolites have Mg-numbers that range from 37–68 and TiO_2 contents from 1.05–1.81 wt% (Table 8). Trace element abundances of V (232–406 ppm), Zn (88–162 ppm), and Y (14–26 ppm) show two-fold variations for the metagabbro and amphibolite clasts, whereas Ni (104–438 ppm), Ce (13–52 ppm), Sr (219–651 ppm), Zr (28–178 ppm), and Ba (19–315 ppm) exhibit three-fold or greater variations. The magnitude of these trace element variations in the amphibolite clasts is comparable to those exhibited by the Site 1067 amphibolites (Table 8, "Igneous and Metamorphic Petrology" section, "Site 1067" chapter, this volume) indicating that the whole-rock chemistry of the Site 1068 clasts has not been affected by the postdepositional processes that may have operated within the breccias. In general, the overall downhole compositional variations in the clasts and variations in clast types are not distinguishable between Subunits IVA and IVB in Hole 1068A (Table 8). Thus, the

chemistries of the clasts from Subunits IVA and IVB are examined together.

Two samples show evidence of alteration in the chemical compositions unlike the other clasts studied from this breccia unit. Sample 173-1068A-16R-4 (Piece 1B, 30–33 cm), is a reddish altered metagabbro with lower SiO_2 and MgO contents and high Fe_2O_3, CaO, and LOI values, unlike the other clasts chosen for whole-rock analysis (Table 8). Thus, the Mg-number of 37 is much lower compared to the range of the other clasts (58–68). Sample 173-1068A-20R-5 (Piece 4, 57–60 cm), is a meta-anorthosite that has been interpreted, on the basis of petrographic evidence, to have been altered by hydrothermal fluids that probably moved out of the serpentinized peridotite basement into the overlying strata at this site. The Mg-number is much higher (80.5) in this sample compared to the amphibolites and metagabbros from Unit IV or the tonalite gneiss from Hole 1067A (Mg-number of 58) as a result of the presence of abundant fine-grained MgO-rich amphiboles resulting from hydrothermal alteration. Metagabbro Sample 173-1068A-19R-4 (Piece 1B, 23–27 cm), was probably contaminated with calcite matrix or vein (Table 8).

The Site 1068 metagabbro and amphibolite compositions appear to lie within a continuum of compositional variation defined by the primitive Site 900 metagabbros and the evolved Site 1067 amphibolites in this region of the southern Iberia Abyssal Plain. The Site 1068 samples exhibit higher compatible element (Ni) and lower TiO_2 abundances compared to the Site 1067 amphibolites at comparable Mg-numbers (Fig. 35). The Site 1068 metagabbros and amphibolites, like the Site 1067 amphibolites, are less primitive than the Site 899 metamicrogabbros and the Site 900 metagabbros. The samples from Sites 1067 and 1068 exhibit an iron-enrichment trend relative to the samples from Sites 899 and 900, but this trend does not distinguish between general tholeiitic and calc-alkaline fractionation trends (Fig. 36). Judging by the generally immobile elements (Ti, Y, Zr, Nb), the Hole 1068A metagabbros and amphibolites are most similar to the Site 899 metamicrogabbros and not as enriched as the Site 1067 amphibolites (Fig. 37). Compared to oceanic gabbros, the Hole 1068A samples are most comparable to the Leg 118 gabbroic rocks (Robinson, Von Herzen, Adamson, et al., 1989), which exhibit a zircon-enrichment trend (Fig. 37).

Unit 1: Serpentinized Peridotite

Three representative samples from the Subunit 1B serpentinized peridotite of Hole 1068A were chosen for shipboard whole-rock XRF analysis. These serpentinized peridotites (Samples 173-1068A-26R-2 [Piece 1B, 51–56 cm], 28R-2, [Piece 1B, 45–46 cm], and 29R-2, [Piece 1F, 99–103 cm]) in general are comparable to the Hole 897C serpentinized peridotites (Fig. 36). The Hole 1068A serpentinized peridotites have consistent Mg-numbers of 91–92 that are similar to the Hole 897C peridotites (Mg-numbers of 90–94) and the Hole 897D samples (Mg-numbers of 91–96). Because of the difficulty of determining the original modal abundance of plagioclase as a result of the serpentinization processes, the visually estimated abundances range from <5% to 20% in the Hole 1068A serpentinized peridotites. However, from normative calculations (Table 8) for the Hole 1068A samples discussed here, plagioclase would have constituted <10% of the peridotite. The whole-rock compositions of the Hole 1068A serpentinized peridotites also indicate that a low amount of plagioclase was originally present (Al_2O_3 and CaO; Fig. 38). The Site 897 serpentinized peridotites exhibit a much larger range of modal plagioclase compared to the Hole 1068A samples. The Hole 1068A serpentinized peridotites fall within the compositional range defined by the Site 897 peridotites (Figs. 36, 38). The Hole 1068A samples have generally higher TiO_2 abundances (0.13 wt%–0.23 wt%) compared to most of the Site 897 serpentinized peridotites (80% at <0.13 wt%) indicating that the Hole 1068A samples may have originally had a larger amount of modal clinopyroxene (Fig. 38). Compared to abyssal peridotites from the Mid-Atlantic Ridge (Leg 153; Cannat, Karson, Miller, et al., 1995), the Site 1068 peridotites have distinctly higher TiO_2 contents but comparable MgO contents and Mg-numbers (89.0–91.3; Fig. 38).

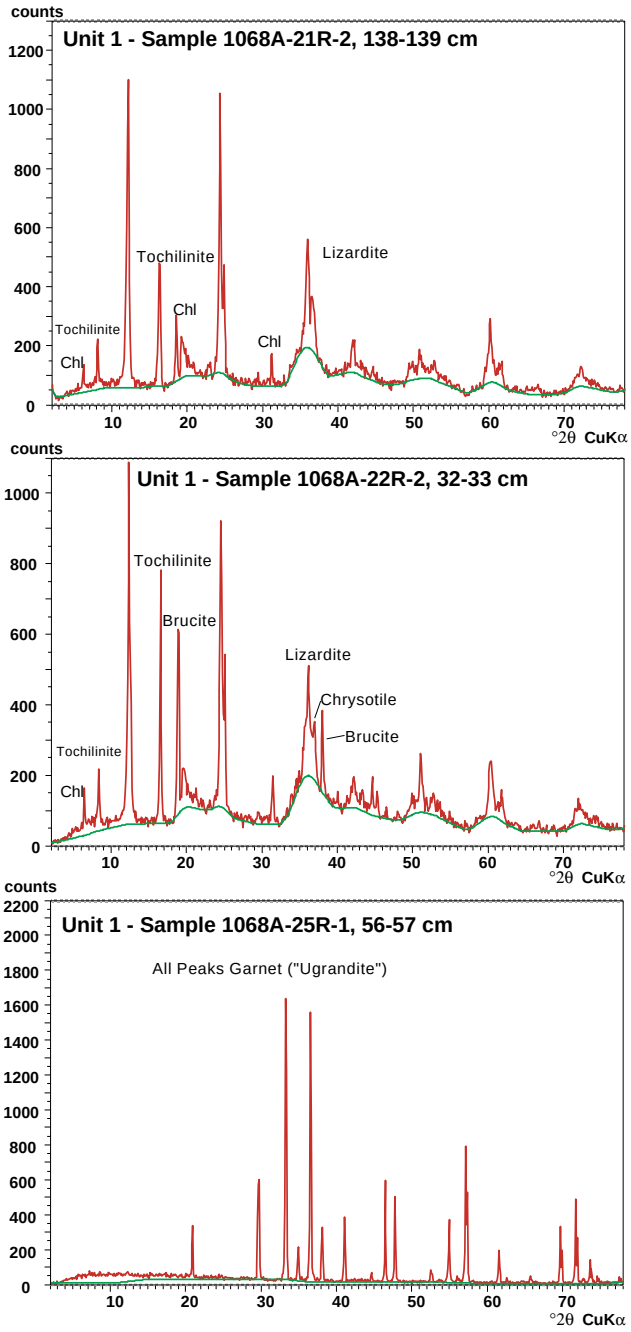

Figure 34. XRD patterns from serpentinites and veins in serpentinites in Unit 1.

STRUCTURAL GEOLOGY

Hole 1068A passed through 141.7 m of Eocene to Maastrichtian claystones and calcareous claystones (Subunits IIB and IIC), overlying 40.13 m of breccia with predominantly meta-igneous clasts (Unit IV). This breccia was subdivided into three subunits (see "Litho-

Table 8. Major and trace element whole-rock compositions and CIPW norms for Hole 1068A metagabbro, amphibolite, meta-anorthosite, and serpentinized peridotite.

	Clasts from sedimentary breccia–acoustic basement								Crystalline basement		
Subunit:	IVA			IVB				IVC	1B		
Rock name:	Amphibolite	Altered metagabbro	Micro-amphibolite	Foliated amphibolite	Micro-amphibolite	Amphibolite	Metagabbro	Meta-anorthosite	Serpentinized peridotite	Serpentinized peridotite	Serpentinized peridotite
Core, section:	16R-2	16R-4	16R-5	17R-2	18R-2	18R-4	19R-4	20R-5	26R-2	28R-2	29R-3
Interval (cm):	118-119	30-33	63-68	1-6	135-139	60-64	23-27	57-60	51-56	42-46	99-103
Piece:	9B	1B	3B	1A	10	4	1B	4	1B	1B	1F
Depth (mbsf):	858.47	860.15	861.89	866.96	871.87	872.54	879.35	889.62	938.88	948.28	954.50
SiO_2 (wt%)	53.34	37.76	50.85	48.73	50.20	48.07	48.88	48.33	43.43	43.37	44.08
TiO_2	1.29	1.81	1.72	1.52	1.19	1.63	1.05	0.10	0.15	0.23	0.13
Al_2O_3	15.36	11.72	12.78	16.05	17.04	18.06	17.73	26.78	2.10	3.10	1.66
Fe_2O_3	9.78	21.44	12.82	10.99	10.66	11.32	8.14	3.62	8.85	9.26	8.91
MnO	0.16	0.15	0.34	0.17	0.16	0.15	0.17	0.05	0.12	0.13	0.12
MgO	8.32	5.35	8.42	10.18	8.08	6.75	5.85	6.46	43.92	41.22	43.30
CaO	6.93	18.50	7.61	8.17	7.39	9.42	11.78	12.04	0.82	1.84	0.72
Na_2O	4.92	1.56	3.74	3.51	4.12	3.52	2.94	2.66	0.32	0.29	0.25
K_2O	0.42	1.55	0.25	0.93	0.71	0.93	2.74	0.10	0.05	0.06	0.04
P_2O_5	0.13	0.29	0.04	0.23	0.29	0.28	0.16	—	0.01	0.01	—
Total	100.62	100.10	98.55	100.45	99.81	100.12	99.40	100.12	99.77	99.49	99.19
FeO^*/MgO	1.06	3.61	1.37	0.97	1.19	1.51	1.25	0.50	0.18	0.20	0.19
Mg/(Mg + 0.86 Fe)	66.2	36.5	60.2	68.1	63.6	57.9	62.3	80.5	92.0	91.1	91.8
LOI (%)	2.10	13.99	1.74	2.56	2.36	2.36	9.71	2.29	14.38	14.17	14.22
QZ	—	—	—	—	—	—	—	—	—	—	—
CO	—	—	—	—	—	—	—	0.41	0.05	—	—
OR	2.48	—	1.48	5.5	4.20	5.5	16.19	0.59	0.30	0.35	0.24
AB	41.63	—	31.65	27.58	34.86	26.13	10.31	22.51	2.71	2.45	2.12
AN	18.59	20.40	17.34	25.59	25.90	30.73	27.09	59.73	4.00	6.98	3.29
LC	—	7.18	—	—	—	—	—	—	—	—	—
NE	—	7.15	—	1.15	—	1.98	7.89	—	—	—	—
DI	12.12	18.49	16.47	11.11	7.22	11.61	24.70	—	—	1.64	0.22
HY	5.66	—	16.81	—	2.38	—	—	2.83	14.67	14.83	20.68
OL	14.59	21.86	7.76	23.25	19.27	17.17	8.53	12.83	75.17	70.11	69.84
CS	—	14.74	—	—	—	—	—	—	—	—	—
MT	1.99	4.35	2.60	2.23	2.16	2.29	1.65	0.74	1.80	1.88	1.81
IL	2.45	3.44	3.27	2.89	2.26	3.10	1.99	0.19	0.28	0.44	0.25
AP	0.31	0.69	0.09	0.54	0.69	0.66	0.38	—	0.02	0.02	—
Total	99.82	98.30	97.47	99.54	98.94	99.17	98.74	99.83	99.01	98.71	98.44
V (ppm)	232	283	406	278	285	338	263	12	41	59	34
Cr	796	461	351	1150	240	689	437	17	1917	2184	1575
Ni	172	438	116	230	104	128	129	179	1955	1926	1779
Cu	17	47	43	46	28	44	121	6	6	11	5
Zn	118	88	99	162	119	117	100	49	36	46	37
Rb	3	19	3	5	7	6	22	0	0	0	0
Sr	237	219	156	357	243	651	243	410	18	18	17
Y	25	18	18	26	23	25	14	2	2	5	3
Zr	178	90	28	92	115	107	102	3	2	5	2
Nb	8	6	3	9	8	9	8	4	5	5	4
Ba	63	118	19	254	184	315	208	125	30	28	25
Ce	50	19	13	48	41	52	31	33	2	4	1

Note: Total iron is reported as Fe_2O_3. CIPW norms were calculated assuming Fe^{2+} = 0.86 Fe total. — = concentrations were below detection limit.

stratigraphy" section, this chapter). Subunit IVA has a chalk matrix, whereas the matrix in Subunit IVB consists of sand- and silt-sized clasts encased in calcite and iron oxyhydroxides. The lowermost Subunit IVC is characterized by brittle deformation features and strong hydrothermal alteration. The breccia rests on a tectonic contact underlain by almost completely serpentinized peridotite (Unit 1). The origin of Unit IV is problematic: either it represents an entirely sedimentary breccia whose basal part (mainly Subunit IVC) was affected by tectonic deformation after its deposition or it represents a tectonic breccia in its basal part, which grades upward into a sedimentary breccia.

The uppermost part of Unit 1, underlying Unit IV, is a serpentinite fault breccia (Subunit 1A) whereas in the lower part (Subunit 1B) high-temperature structures are partly still visible in highly serpentinized and veined peridotite. Hole 1068A penetrated 62.7 m into the serpentinized peridotite basement.

Structural Observations in Unit II

One hundred ninety-four measurements of true bedding dip in the core reference frame were made on the cores of Subunits IIB and IIC (Fig. 39; Table 9, on CD-ROM, back pocket, this volume). The dips range between 0° and 19° (mean dip 4.3°, standard deviation 3.1°) and suggest a slight increase with depth. Overall, the dip of the postrift sediments in Hole 1068A is shallower than in Hole 1067A (mean dip 11.5°; see Fig. 42, "Structural Geology" section, "Site 1067" chapter).

Deformation structures are very rare in Unit II. Some minor faults and slump folds (e.g., Sections 173-1068A-2R-4 and 173-1068A-5R-3) within siltstone layers result from soft-sediment deformation. Faults with slickensided surfaces crosscutting both claystone and siltstone layers were observed in Sections 173-1068A-2R-3, 9R-5, 9R-6, 11R-4, and 15R-1. The dips of these faults vary between 18° and 64°, the slickenside lineation is mostly parallel to the dip, and the slip sense, where it can be observed, is normal. These faults indicate a slight extensional deformation of Unit II. Zones of shattered claystone with slickensided fragments occur in the vicinity of the normal faults (e.g., Section 173-1068A-2R-3).

Structural Observations in Unit IV

Deformation structures in the breccia fall into two categories: (1) structures of the breccia that are related to its formation or that over-

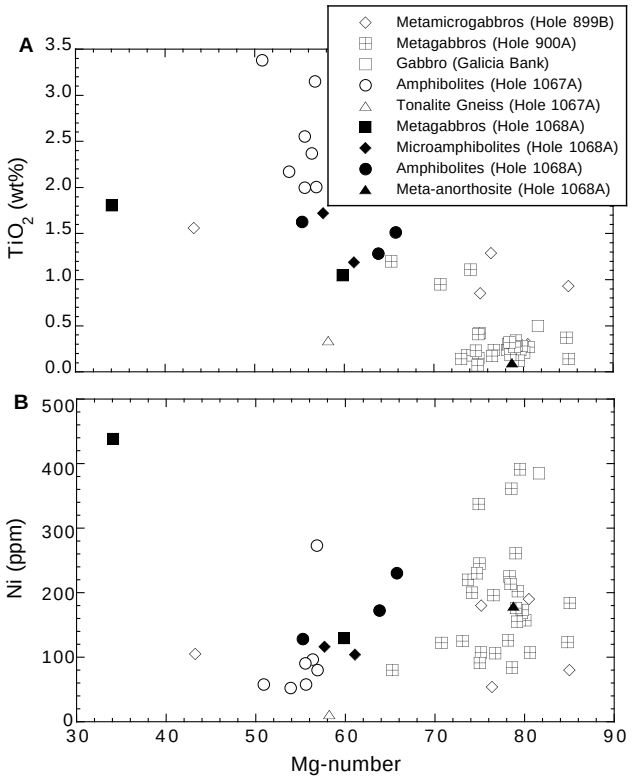

Figure 35. (**A**) Mg-number vs. TiO_2 (wt%) and (**B**) Mg-number vs. Ni (ppm) variation diagrams for the Site 1068 clasts of metagabbro, amphibolite, and meta-anorthosite. Also shown are the Site 899 metamicrogabbros, Site 900 metagabbros, a gabbro from Galicia Bank, and Site 1067 amphibolites and tonalite gneiss for comparison. Data from Sawyer, Whitmarsh, Klaus, et al. (1994); Schärer et al. (1995); Cornen et al. (1996a); Seifert et al. (1996); and "Igneous and Metamorphic Petrology" section, "Site 1067" chapter, this volume.

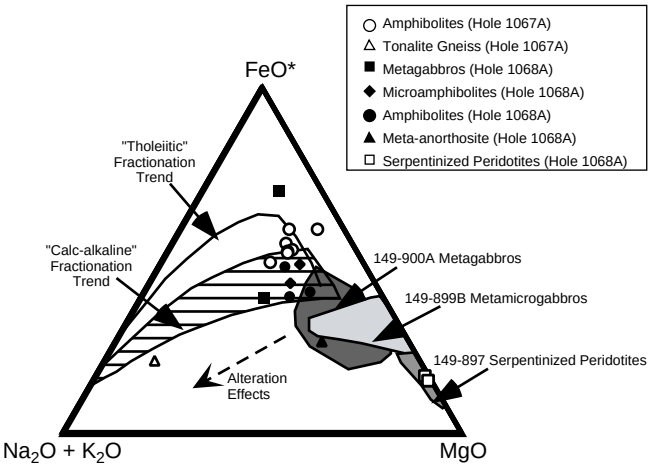

Figure 36. AFM ternary diagram for the Site 1068 clasts of metagabbro, amphibolite, and meta-anorthosite. Also shown are the Site 899 metamicrogabbros, Site 900 metagabbros, and Site 1067 amphibolites and tonalite gneiss for comparison. The approximate fractionation paths for tholeiitic and calc-alkaline magmas are displayed for reference (after Ringwood, 1977 and references cited within). Results from serpentinized peridotites from Sites 897 and 1068 are also plotted. Data from Sawyer, Whitmarsh, Klaus, et al. (1994); Cornen et al. (1996a); Seifert and Brunotte (1996); Seifert et al. (1996); and "Igneous and Metamorphic Petrology" section, "Site 1067" chapter, this volume.

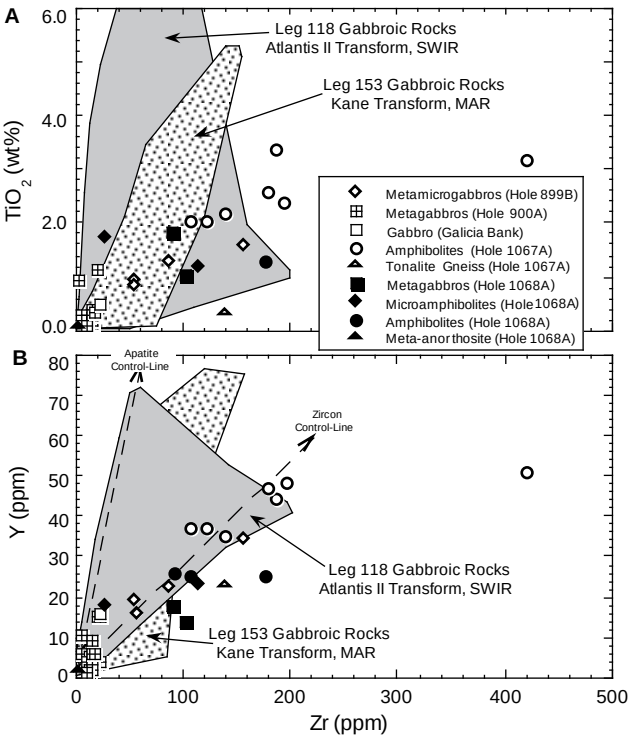

Figure 37. (**A**) TiO_2 (wt%) vs. Zr (ppm) and (**B**) Y (ppm) vs. Zr (ppm) variation diagrams for the Site 1068 clasts of metagabbro, amphibolite, and meta-anorthosite. The Site 1068 samples are shown in relation to the Site 899 metamicrogabbros, Site 900 metagabbros, a gabbro from Galicia Bank, and Site 1067 amphibolites and tonalite gneiss. The fields of oceanic gabbro compositions from the Southwest Indian Ridge (Leg 118) and Mid-Atlantic Ridge (Leg 153) are displayed. Also shown in (B) are the approximate paths for apatite and zircon accumulation based on Y compatibility in apatite (Deer et al., 1993) and Zr and Y compatibilities in zircon (Deer et al., 1982). Data from Robinson, Von Herzen, Adamson, et al. (1989); Sawyer, Whitmarsh, Klaus, et al. (1994); Cannat, Karson, Miller, et al. (1995); Cornen et al. (1996a); and "Igneous and Metamorphic Petrology" section, "Site 1067" chapter, this volume.

print the breccia after its formation, and (2) internal structures in the clasts predating the formation of the breccia.

Structures of the Breccia

The structures described here affected matrix and clasts together. Brittle deformation and veining increase toward the base of Unit IV. Fractures cutting and offsetting clasts are rare in the upper part of the breccia, becoming increasingly common toward the base. Jigsaw-style disintegrated clasts are observed in Cores 173-1068A-18R and 19R. Figure 40 shows an example from interval 173-1068A-19R-2, 14–19 cm, where pre-breccia epidote veins can be traced across several fragments of a disintegrated clast. Matrix consisting of sand- to silt-sized grains and rock fragments has filled the gaps that opened between the fragments, which indicates that, when the clasts broke apart, the matrix was not lithified. Clast disintegration appears to be a common process in Cores 173-1068A-18R and 19R, since clasts of similar rock type (e.g., foliated amphibolite, coarse-grained metagabbro, or fine-grained metagabbro) occur together in clusters.

A similar downward increase is observed for calcite veining. Calcite veins are thin (1 to 2 mm) in the upper part. There, they often follow the margins of clasts, but also cut across clasts and matrix. They are thicker and pervasive at the base of the breccia. In Core 173-1068A-20R, calcite veins are up to 1 cm thick, cut across clasts and

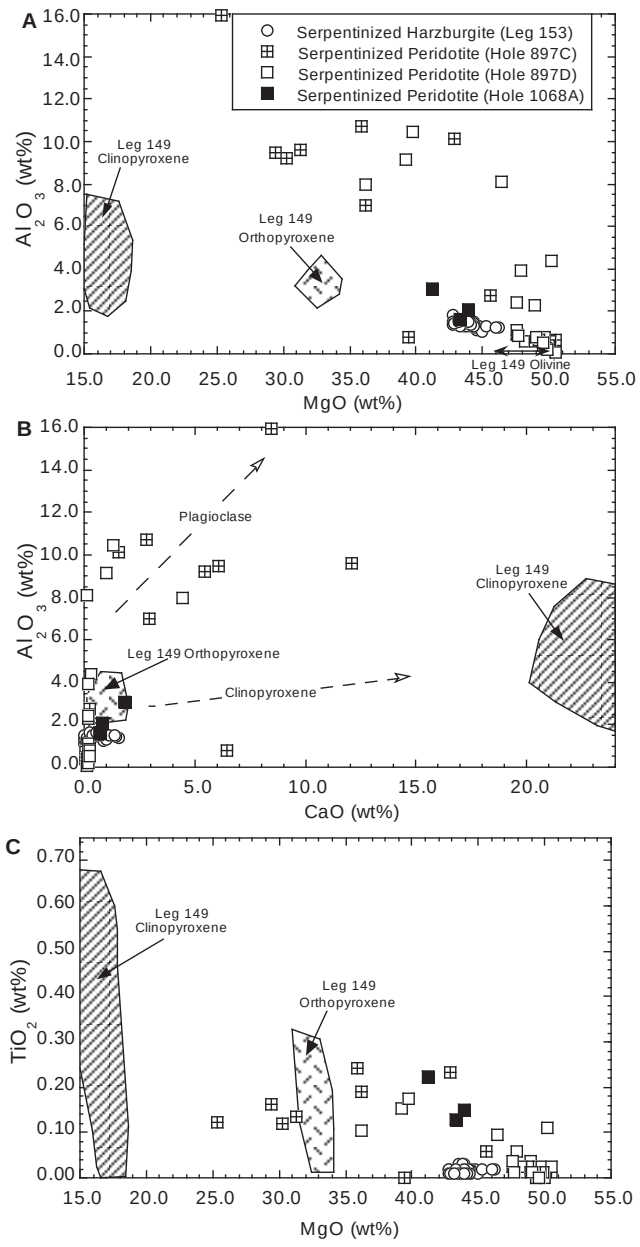

Figure 38. (**A**) MgO (wt%) vs. Al_2O_3 (wt%); (**B**) CaO (wt%) vs. Al_2O_3 (wt%); and (**C**) MgO (wt%) vs. TiO_2 (wt%) variation diagrams for the Hole 1068A serpentinized peridotites. Also shown are the serpentinized peridotites from Holes 897C and 897D from the southern Iberia Abyssal Plain and Leg 153 serpentinized harzburgites from the Kane Transform region, Mid-Atlantic Ridge. Mineral compositional fields based on Leg 149 results are displayed. Data from Cannat, Karson, Miller, et al. (1995); Cornen et al. (1996b); and Seifert and Brunotte (1996).

matrix, are predominantly steeply oriented, and are filled with several generations of sparry calcite (Fig. 41). In addition to calcite veining, a brittle overprint of the breccia is also suggested by the presence of sheared clasts, the occurrence of rounded clasts and the formation of a weak foliation at the base of the breccia unit. In Core 173-1068A-20R the matrix to clasts ratio appears to increase, and the clasts are generally smaller and more rounded compared to Core 173-1068A-19R. Elongated clasts are aligned and define a weak foliation that is also marked by the preferred orientation of phyllosilicates in the matrix, as observed under the microscope. The cataclastic overprint in

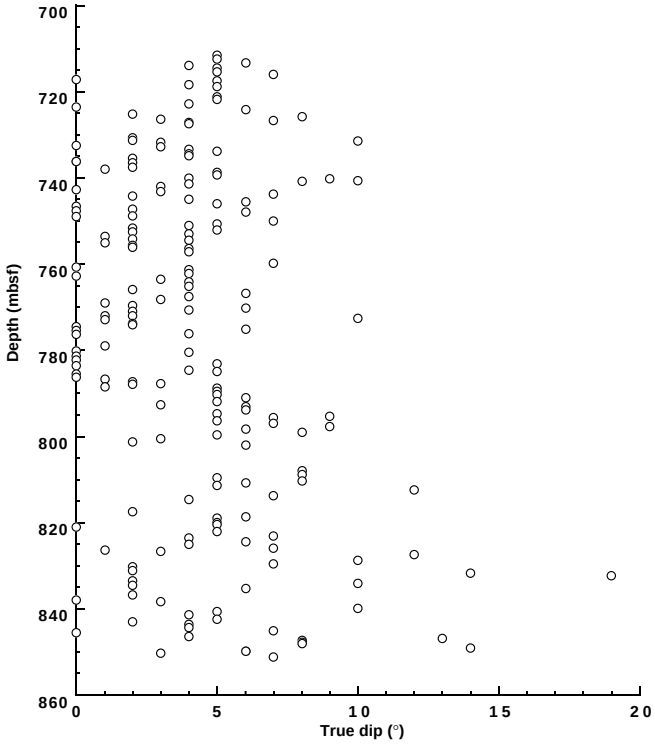

Figure 39. Dip of bedding vs. depth for sediments in Unit II.

Core 173-1068A-20R is accompanied by penetrative chloritization (e.g., Section 173-1068A-20R-1). Anastomosing, shallow-dipping serpentine veins occur in the cataclastically deformed breccias near the contact with Unit 1 (serpentinized peridotite) in Section 173-1068A-20R-7. The base of the breccias of Subunit IVC is defined by the last occurrence of gabbro and amphibolite clasts and the first occurrence of serpentinized peridotite clasts and is located in Section 173-1068A-20R-7, 105 cm. The contact is sharp. Thus, a brittle overprint that is locally observed in Cores 173-1068A-18R and 19R is more intense but still irregularly distributed in Sections 173-1068A-20R-1 to -5, and it increases gradually in Sections 173-1068A-20R-6 and -7 (i.e., toward the contact with the underlying brecciated serpentinized peridotites of Subunit 1A). The change in matrix composition from mainly calcite to chlorite and the occurrence of serpentine veins in the deformed breccias suggest that brittle deformation was assisted by fluid infiltration leading to alteration processes.

To summarize, there is ample evidence that the breccia was overprinted by brittle deformation in its lower part and along its base. More detailed studies are needed, however, to decide whether the breccia is completely of sedimentary origin and was affected by brittle deformation only after its deposition, or whether the lower part of the breccia was already formed as a tectonic breccia.

Internal Structures in the Breccia Clasts

Internal structures in the clasts were acquired before these were deposited in the breccia and yield evidence of deformation in the source area. Different types of ductile and brittle deformation are observed in the clasts. Clasts in the breccia include metagabbro, amphibolite, anorthosite, tonalite, epidosite, and chloritite.

Metagabbro and Amphibolite

Ductile deformation under granulite- to amphibolite-facies conditions is observed in metagabbro and amphibolite clasts (see also "Igneous and Metamorphic Petrology" section, this chapter). Some metagabbro clasts are essentially undeformed (e.g., Sample 173-

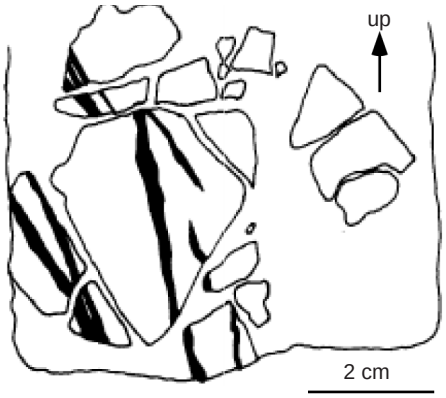

Figure 40. Sketch of an example of a disintegrated clast (jigsaw clast) from Subunit IVB (interval 173-1068A-19R-2, 14–19 cm). Dark bands are epidote veins.

1068A-16R-4, 30–33 cm). All intermediate stages are observed between these undeformed metagabbros and completely recrystallized and strongly foliated amphibolites.

A sample of metagabbro from interval 173-1068A-19R-4, 56–60 cm, still clearly shows the igneous texture, zoning in up to 5-mm-sized, euhedral plagioclase grains. These grains are partly strained (undulatory extinction) and along some of their margins they are recrystallized to subgrains and new grains of a smaller size (0.1 to 0.3 mm). Polygonal aggregates of plagioclase neoblasts have a strong crystallographic preferred orientation (as seen by turning the microscope stage with the gypsum plate inserted). In the same sample, large primary clinopyroxene crystals are replaced by amphibole along fractures and margins. The formation of subgrains and recrystallized grains along a plagioclase/plagioclase grain boundary in a weakly deformed metagabbro from interval 173-1068A-15R-6, 10–14 cm, is shown in Figure 42.

In other, more deformed, samples, plagioclase is recrystallized to a higher degree and elongate plagioclase porphyroclasts are surrounded by aggregates of neoblasts (core-mantle structure; e.g., metagabbro Sample 173-1068A-16R-3, 106–111 cm). These neoblasts show polygonal texture, strong crystallographic preferred orientation, and also some preferred orientation of the grain shapes (Fig. 43).

In amphibolite Samples 173-1068A-17R-2, 1–6 cm, and 17R-4, 76–80 cm, plagioclase has largely recrystallized and forms foliation-parallel ribbons and aggregates of neoblasts with polygonal texture and crystallographic preferred orientation, in which elongate, strained porphyroclasts of plagioclase occur. In these foliated amphibolites, porphyroclasts of amphibole exist and fine-grained amphibole occurs together with plagioclase neoblasts in the pressure-shadow tails of these porphyroclasts, indicating that amphibole recrystallized dynamically together with the plagioclase (Fig. 44). Finally, strongly foliated amphibolites occur in which plagioclase is completely, and amphibole almost completely, recrystallized (e.g., Sample 173-1068A-16R-1, 66–68 cm). The degree of deformation correlates negatively with the amount of preserved clinopyroxene. In strongly foliated rocks, clinopyroxene is commonly replaced by amphibole.

Meta-anorthosite

Meta-anorthosites display similar deformation features as the metagabbros and amphibolites. Some are weakly deformed and show only the beginning of plagioclase recrystallization (e.g., Samples 173-1068A-15R-5, 71–75 cm, and 15R-5, 88–93 cm), others show recrystallized plagioclase aggregates with a preferred crystallographic orientation and a polygonal texture that surrounds strained plagio-

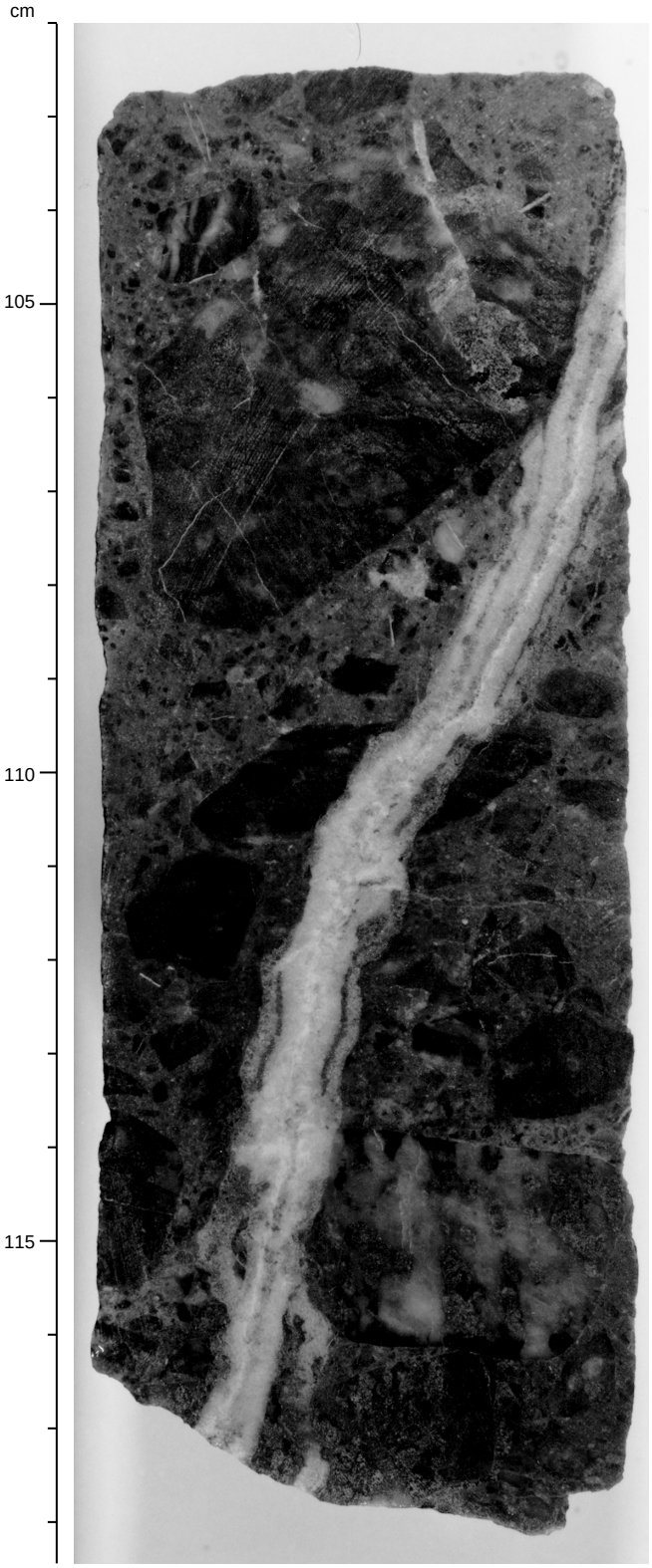

Figure 41. Tectonically overprinted breccia from Subunit IVC crosscut by calcite vein. Interval 173-1068A-20R-5, 102.5–118 cm.

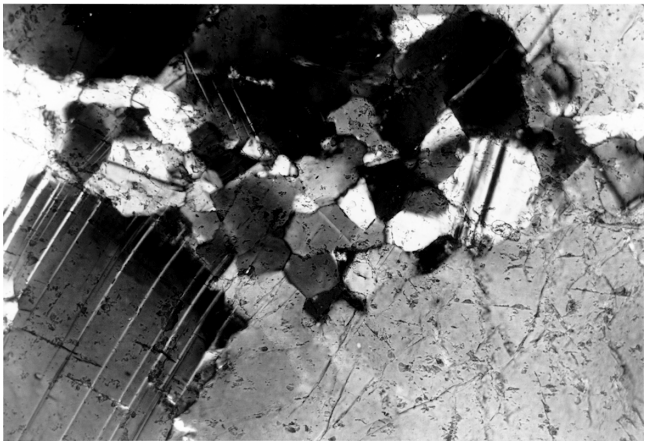

Figure 42. Photomicrograph showing subgrains and polygonal recrystallized grains of plagioclase along a grain boundary between old plagioclase grains in a weakly deformed metagabbro clast in the breccia (Unit IV) from Hole 1068A (Sample 173-1068A-15R-6, 10–14 cm; crossed polars).

Figure 43. Photomicrograph showing a strained plagioclase porphyroclast surrounded by recrystallized grains (core-mantle structure) in a clast of deformed metagabbro from Sample 173-1068A-16R-3 [Piece 4, 106–111 cm] (crossed polars). Note the slightly elongate shape and preferred orientation of the plagioclase neoblasts.

clase porphyroclasts (core-mantle structure; e.g., Samples 173-1068A-15R-6, 40–43 cm, and 20R-5, 57–60 cm).

Tonalite

An altered tonalite clast from interval 173-1068A-15R-6, 52–56 cm, exhibits a foliation defined by the alignment of plagioclase porphyroclasts with undulatory extinction, deformation twins, and subgrains. The plagioclase porphyroclasts are recrystallized along their boundaries. Layers rich in quartz and (secondary) calcite lie parallel to the foliation.

Epidosite and Chloritite

Clasts of epidosite occur in several samples (e.g., Sample 173-1068-17R-4, 76–80 cm). The epidosite is similar to the material in epidote veins within other clasts. Epidosite clasts may be assumed, therefore, to represent fragments of veins. In the same sample, a fragment of chloritite occurs. It consists entirely of chlorite, which is aligned along two foliations suggesting an S/C fabric (see Passchier and Trouw, 1996).

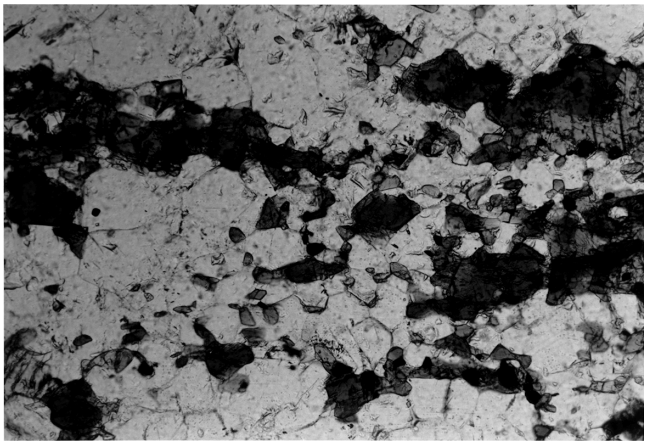

Figure 44. Photomicrograph showing polygonal plagioclase aggregate with small, interspersed amphibole grains. Recrystallized tails of larger amphibole porphyroclasts are also visible. This microstructure indicates dynamic recrystallization of amphibole together with plagioclase (Sample 173-1068A-17R-4 [Piece 1B, 76–80 cm]; crossed polars).

Veins in Clasts

Several types of vein are observed on cores and in thin sections. On the cores, it is obvious that the epidote veins are older than the formation of the breccia, because they are restricted to the clasts. Such epidote veins often occur at the margins of clasts, indicating that the disintegration of the source rock (or protolith, if part of the breccia is of tectonic origin), was facilitated by the network of epidote-filled fractures.

Tectonic Setting of the Breccia

The above observations suggest that the breccia was shed from a brittly deformed source area that exposed mostly medium- to high-grade meta-igneous rocks varying in composition between gabbro, anorthosite, and, in one sample, tonalite, and varying in deformation between undeformed and strongly foliated. The comparable deformation and metamorphic history of these rocks suggests a local source. The uppermost part of Subunit IVA, in which Upper Jurassic to Lower Cretaceous limestone clasts and some fragments of biotite schist occur, requires some input from a more distant source area (see "Lithostratigraphy" section, this chapter). The overprint of the breccia by brittle deformation, concentrated in Subunit IVC, indicates that movements occurred along the fault that separates the breccia from the underlying serpentinized peridotite (Unit 1), during and after the deposition of the breccia. It cannot be decided at the moment whether the breccia is entirely of sedimentary origin, or represents a tectonic breccia in its lowermost part (Subunit IVC), that grades upward into a sedimentary breccia. The jigsaw clasts may be interpreted as indicating some tectonic brecciation.

Structural Observations in Unit 1: Serpentinized Peridotite

The serpentinized peridotite forming the basement at Site 1068 is subdivided for structural reasons into an upper Subunit 1A, of serpentinite fault breccia, and a lower Subunit 1B, of serpentinized peridotite in which structures of the original peridotite are preserved.

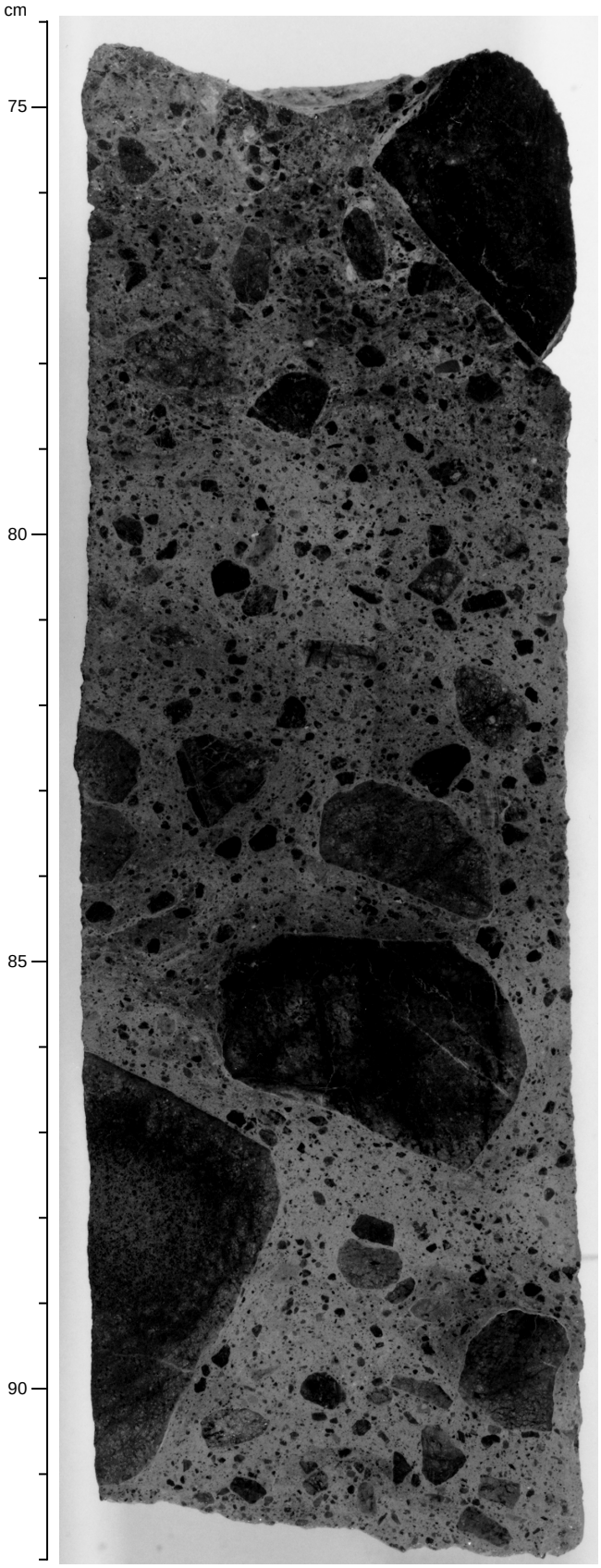

Figure 45. Matrix-supported serpentinite breccia from Subunit 1A in interval 173-1068A-20R-7, 74–92 cm.

Subunit 1A: Serpentinite Breccia

A matrix-supported breccia (Fig. 45) in Subunit 1A is underlain by incohesive serpentinite material containing clasts of serpentinized peridotite. The base of the serpentinite breccia is difficult to locate because of the poor recovery in Cores 173-1068A-21R and 22R, and it is assumed to coincide with the bottom of Core 173-1068A-21R, because the top of Core 173-1068A-22R is formed by cohesive, nonbrecciated, serpentinized peridotite.

The matrix-supported breccia of interval 173-1068A-20R-7, 74–92 cm (Fig. 45) is formed by mainly rounded clasts of serpentinized peridotite. "Jigsaw" clasts and elongate clasts of serpentine are also present, and the latter are aligned parallel to a weak foliation. Under the microscope (Sample 173-1068A-20R-7, 82–85 cm), elongated opaque fragments and fine-grained phyllosilicates (mainly serpentine) define a foliation that curves around the clasts (see "Igneous and Metamorphic Petrology" section, this chapter; Fig. 31). The size of clasts in the breccia ranges from 5 cm to microscopic. Comparing the grain-size distribution in the cores and under the microscope, the distribution appears to be scale-independent, suggesting that cataclasis was the dominant deformation mechanism during formation of the breccia (Sammis et al., 1986). However, the occurrence of lenticular chrysotile fibers in the matrix, which are aligned parallel to the foliation, suggests that with progressive deformation the deformation style changed from brittle to more ductile, that is, from fluid-assisted cataclastic fracturing to cataclastic flow. This is compatible with the local formation of a foliation and the occurrence of rounded clasts resulting from frictional wear. Altogether, it appears that the serpentinite breccia of Subunit 1A most likely formed as a fault gouge that lithified after movements along the fault plane terminated.

Subunit 1B: Serpentinized Peridotite

The serpentinized peridotite of Subunit 1B exhibits a foliation marked by elongate spinel grains, typically 1 to 2 mm long, and their light grey coronas (identified as chlorite in thin sections). In addition, slightly elongate bastite pseudomorphs after pyroxene are commonly aligned parallel to the foliation. Several vein generations can be observed.

Foliation

The foliation occurs from Core 173-1068A-23R down to the bottom of Hole 1068A. It is commonly only weakly developed. The true dip of the foliation in the core reference frame varies between 14° and 88° (Fig. 46; Table 10 on CD-ROM, back pocket, this volume) with a mean value of 43.1° and a standard deviation of 15.2°. Possible Viscous Remanent Magnetization (VRM) vectors of serpentinized peridotite samples were used to reconstruct the orientation of the foliation in the geographical reference frame (see "Paleomagnetism" section, "Explanatory Notes" chapter, this volume). This was done by rotating the orientation measured in the core reference frame around a vertical axis by the angle of declination of the VRM. This yielded relatively consistent, although preliminary, results. For eight out of nine measurements, the foliation dips between northwest (321°) and west-southwest (255°); in one case, the dip is toward east-northeast (075°; Table 11). Under the microscope, the foliation is marked by spinel with chlorite coronas that presumably have replaced plagioclase. Slightly elongate bastite pseudomorphs after pyroxene and relict exsolution lamellae within them are locally aligned parallel to the foliation, suggesting that the latter formed under high-temperature conditions. Because of pervasive serpentinization, no direct evidence exists for a progressive development of the foliation from the spinel into

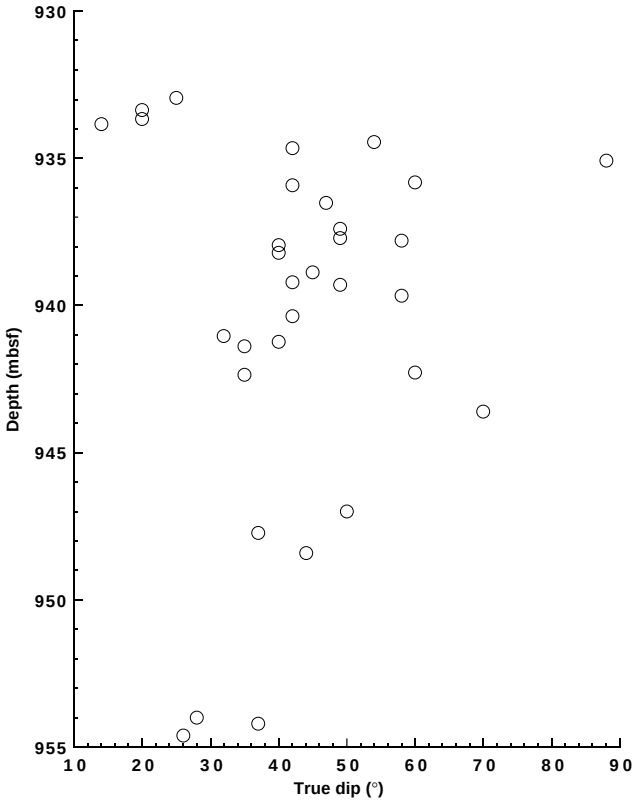

Figure 46. Dip of foliation vs. depth in the serpentinized peridotites of Subunit 1B.

the plagioclase stability field as described by Beslier et al. (1996) for ODP Leg 149 cores.

Veins

Veins bear various serpentine minerals, including chrysotile and lizardite, and talc (see "Igneous and Metamorphic Petrology" section, this chapter). Garnet and tochilinite occur in Unit 1 and in the lowermost part of Subunit IVC (see "Igneous and Metamorphic Petrology" section, this chapter). Several phases of veining are observed; however, only veins of the last phase, which are typically 2–10 mm wide, planar and filled with pale blue-green to white fine-grained serpentine, form a definable group. Their orientations, measured on a continuous section of core (Section 173-1068A-28R-1, Piece 4), are plotted in Figure 47. The poles to these veins form two clusters, which lie on a nearly vertical great circle. These clusters may be interpreted as representing a conjugate vein set formed in response to N-S extension (in the core reference frame).

The geometries of the earlier phases of veining are complex everywhere and record several stages of fluid migration coupled with deformation. These earlier veins are generally <0.1 mm wide and are composed of fibrous dark green chrysotile and/or platy dark green lizardite(?). They are often contained within the later pale blue-green to white fine-grained serpentine veins, within which they are significantly shortened. In many examples, early chrysotile veins show intense microfolding and early lizardite(?) veins are fragmented and show intense microthrusting (Fig. 48A). In other examples, early lizardite(?) veins are pulled apart into discrete laths that are suspended in the later vein infill (Fig. 48B). It is difficult to explain why these

Table 11. Structural and magnetic data from the basement Subunit 1B from Hole 1068A.

Core, section, interval (cm)	VRM component Declination (°)	VRM component Inclination (°)	Working azimuths and dips of foliation (°)	Angle of rotation (°)	Reconstructed azimuths and dips of foliation (°)
173-1068A-					
25R-1, 78	351	65	Not measured	(—)	(—)
25R-1, 111	15	65	090/20	(–) 15	75/20
26R-1, 77	278	52	239/49	(+) 82	321/49
26R-1, 107	313	70	270/40	(+) 47	317/40
26R-2, 92	244	57	154/49	(+) 116	270/49
28R-1, 61	46	64	308/50	(–) 46	262/50
28R-1, 121	29	60	284/37	(–) 29	255/37
28R-2, 62	21	65	302/44	(–) 21	281/44
29R-3, 48	156	51	090/28	(–) 156	294/28
29R-3, 57	166	51	090/37	(–) 166	284/37

Note: (+) = clockwise, (–) = anticlockwise. The declinations have been corrected post-cruise to account for an error in the cryogenic magnetometer software (see "Paleomagnetism" section, "Explanatory Notes" chapter, this volume).

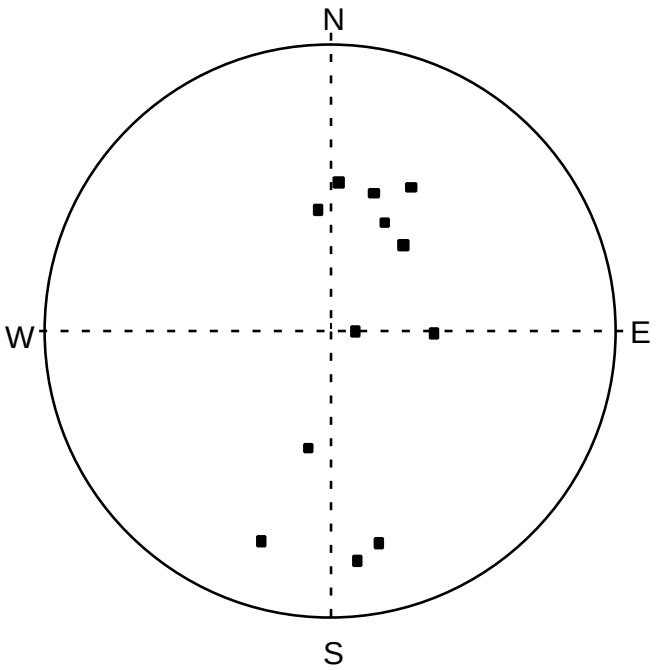

Figure 47. Stereographic, lower hemisphere equal-area plot of orientations (in the core reference frame) of late-phase serpentine veins measured on a continuous section of core (Section 173-1068A-28R-1 [Piece 4]).

veins exhibit both extension and compression, but it is not implausible that they should record the internal dynamics that result from the volume expansion inherent in serpentinization.

ORGANIC AND INORGANIC GEOCHEMISTRY

Concentrations of carbonate, organic carbon, and total nitrogen in sediments from Hole 1068A were measured on two to six samples per core throughout the cored interval (711.3–955.8 mbsf). Routine

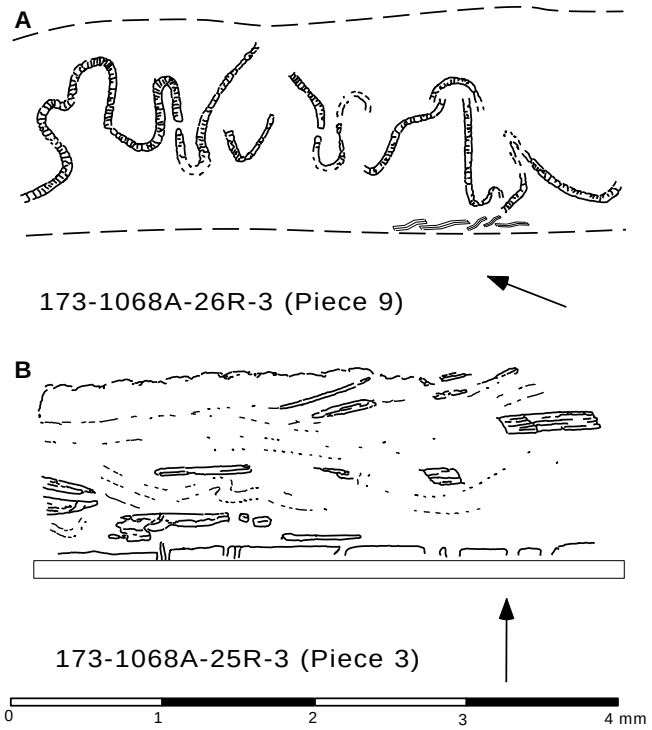

Figure 48. **A.** Early chrysotile veins showing intense microfolding, and early fragmented lizardite(?) veins (at the bottom of the vein) showing microthrusting (Section 173-1068A-26R-3 [Piece 9]. **B.** Early lizardite(?) veins are pulled apart into discrete laths that are suspended in the later vein infill (Section 1068A-25R-3 [Piece 3]). Arrows indicate upward direction.

measurements were also made of headspace gas compositions as part of the drilling safety program. Four interstitial water samples were squeezed from the sediments in the interval from 717.2 to 810.7 mbsf. Sediments from below this depth were too lithified to allow interstitial water sampling.

Inorganic and Organic Carbon

Concentrations of carbonate carbon in sediments at Site 1068 vary from 0.17% to 11.5%, equivalent to $CaCO_3$ concentrations (assuming that all the carbonate is present as pure calcite) of 1.4% to 96% (Table 12). All analyzed sediments belong to lithostratigraphic Unit II, which consists of upward-darkening units of basal siltstone/sandstone overlain by calcareous claystone, and capped by claystone (see "Lithostratigraphy" section, this chapter). Shown in Figure 49 are the $CaCO_3$ contents of sediments from these three different lithologic types within individual upward-darkening sequences. In general, the basal siltstone and sandstone layers are more carbonate rich (mostly 40%–70%) than the overlying calcareous claystone, although there is considerable overlap in carbonate contents. The dark claystones that typically form the caps of the upward-darkening sequences have even lower $CaCO_3$ contents, varying from 1.5% to nearly 20%. This pattern is consistent with the interpretation that the basal siltstone and sandstone and overlying calcareous claystone were deposited near or below the CCD by turbidity currents carrying carbonate-rich material from shallower depths, whereas the dark claystones represent hemipelagic sediments.

Concentrations of organic carbon are generally quite low (mostly <0.1%) in sediments from Subunit IIB, but values as high as 0.41% are present (Table 12). Nitrogen contents were near or below detection in all samples. The C/N ratios of samples with the highest organic C vary from 2.2 to 8.3, which indicates a predominantly marine source for the organic matter. The lower C/N ratios of the other samples are probably an artifact of organic C contents that are close to the detection limit.

Table 12. Carbonate, carbon, and nitrogen in sediments from Hole 1068A.

Core, section, interval (cm)	Depth (mbsf)	Inorganic C (wt%)	$CaCO_3$ (wt%)	Organic C (wt%)	N (wt%)	Organic C/N
173-1068A-						
1R-1, 52-54	711.82	2.07	17.3	—	0.05	—
1R-1, 57-58	711.87	3.59	29.9	—	0.04	—
1R-1, 68-69	711.98	5.16	43.0	—	—	
1R-3, 8-9	714.38	5.42	45.2	—	0.05	—
1R-5, 38-39	717.68	1.02	8.5	—	0.11	—
1R-5, 44-45	717.74	2.46	20.5	—	0.04	—
2R-1, 12-13	721.02	0.55	4.6	0.05	0.06	0.9
2R-1, 17-19	721.07	2.61	21.8	—	0.05	—
2R-1, 23-25	721.13	3.79	31.6	0.01	—	
2R-3, 35-37	724.25	3.57	29.7	0.14	0.04	3.6
3R-3, 36-37	733.46	0.77	6.4	0.02	0.08	0.2
3R-3, 41-42	733.51	1.92	16.0	0.03	0.05	0.5
3R-3, 49-50	733.59	6.70	55.8	—	0.04	—
3R-3, 54-55	733.64	6.33	52.8	—	0.04	—
4R-2, 36-38	742.16	6.80	56.6	—	0.03	—
4R-4, 42-44	745.22	3.22	26.8	0.09	0.05	1.8
4R-4, 61-63	745.41	3.04	25.3	0.11	0.04	2.7
4R-4, 71-73	745.51	4.98	41.5	0.11	0.03	3.7
4R-5, 22-24	746.52	6.28	52.3	—	—	
5R-5, 24-26	756.14	0.17	1.4	—	0.10	—
5R-5, 31-33	756.21	1.07	8.9	0.41	0.05	8.3
5R-5, 37-39	756.27	4.61	38.4	0.04	—	
5R-5, 49-51	756.39	5.02	41.8	—	—	
6R-3, 62-64	763.22	6.25	52.0	0.01	0.04	0.4
6R-3, 108-110	763.68	4.48	37.4	0.06	0.05	1.1
6R-3, 137-139	763.97	6.16	51.3	—	—	
7R-1, 67-68	769.97	0.21	1.7	0.11	0.05	2.2
7R-1, 74-75	770.04	2.88	24.0	—	0.04	—
7R-1, 81-82	770.11	8.18	68.2	—	0.03	—
7R-2, 30-31	771.10	7.07	58.9	—	—	
8R-1, 110-111	780.00	0.75	6.2	—	0.05	0.1
8R-1, 131-132	780.21	1.16	9.6	0.02	0.05	0.5
8R-CC, 2-3	788.55	11.53	96.1	—	—	
9R-3, 138-139	792.88	8.00	66.7	0.09	—	
9R-5, 53-55	795.03	0.48	4.0	0.02	0.08	0.3
9R-5, 67-69	795.17	5.75	47.9	0.06	0.03	1.9
9R-5, 87-89	795.37	8.11	67.5	—	—	
10R-1, 38-39	798.48	0.24	2.0	0.05	0.09	0.6
10R-1, 53-54	798.63	7.32	60.9	0.18	—	
10R-2, 42-43	800.02	7.10	59.1	0.04	—	
11R-2, 13-15	809.33	0.21	1.8	0.05	0.05	0.9
11R-2, 24-26	809.44	6.04	50.3	0.06	—	
11R-2, 35-36	809.55	7.14	59.5	0.09	—	
12R-2, 99-100	819.79	0.73	6.1	0.04	0.05	0.7
12R-2, 101-102	819.81	0.83	6.9	0.02	0.05	0.5
12R-2, 104-106	819.84	1.03	8.6	—	0.04	—

Note: — = concentration below detection limit.

Headspace Gas Measurements

In Hole 1068A, methane concentrations in headspace gases from sediments in Unit II were low in the interval from 717.3 to 769.3 mbsf and then gradually increase with depth to the contact with the underlying lithified breccia (Unit IV; see Table 13; Fig. 50). No headspace samples were taken from the breccia, but samples were taken from the underlying serpentinite breccias (basement Unit 1 in Fig. 50). Methane concentrations in the headspace gases from the serpentinites are very high, varying from 2150 to 6000 ppm, and show a general decrease with increasing depth. Such high methane concentrations are probably caused by the reduction of seawater-dissolved inorganic carbon during the process of serpentinization. Given the very low organic carbon concentrations in the sediments of Unit II overlying the breccia, the downward-increasing methane concentra-

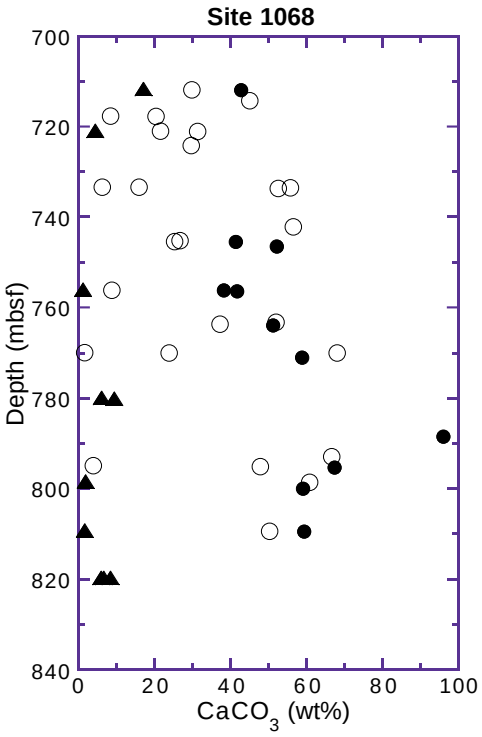

Figure 49. Downhole plot of $CaCO_3$ in sediments from Hole 1068A. Basal siltstone and sandstone layers from individual upward-darkening sequences are shown as solid circles, overlying calcareous claystones as open circles, and hemipelagic claystone as solid triangles.

tions in the sediment headspace gases are probably caused by upward diffusion of methane through the Unit IV breccias from the underlying serpentinites (Fig. 50).

Interstitial Water

Interstitial water samples collected from Hole 1068A have cation and anion concentrations (Table 14) that are generally similar to those in interstitial water collected from a similar depth (721.5 mbsf) at Site 900 (Shipboard Scientific Party, 1994c). At the latter site, a complete profile of interstitial water compositions was determined from 12.6 to 721.5 mbsf.

PHYSICAL PROPERTIES

Introduction

For all lithologies of Hole 1068A, physical properties were measured on both split cores and discrete samples. Because of voids between cores and core liners as well as discontinuity of recovery, GRAPE and compressional-wave velocity measurements were not conducted on the multisensor track (MST). MST measurements of magnetic susceptibility and natural gamma radiation were made on all sedimentary cores in Hole 1068A as well as on competent basement whole rounds greater than 20 cm in length. The sampling interval was 3 cm for magnetic susceptibility and 10 cm for natural gamma radiation measurements. Core-size variation resulted in scatter in magnetic susceptibility and natural gamma radiation measurements, but the data are useful for semi-quantitative correlation with other properties measured at Hole 1068A as well as with MST records from Hole 1067A. Compressional-wave velocities were measured

Table 13. Methane and ethane concentrations in headspace gas samples from Hole 1068A.

Core, section, interval (cm)	Depth (mbsf)	Methane (ppm)	Ethane (ppm)
173-1068A-			
1R-5, 0-2	717.30	2	
2R-4, 0-5	725.40	3	
3R-2, 149-150	733.09	3	
4R-3, 0-5	743.30	4	
5R-5, 99-100	756.89	4	
6R-7, 69-70	769.29	8	
7R-2, 148-150	772.28	12	
8R-4, 0-5	783.40	23	
9R-1, 149-150	789.99	37	
10R-2, 0-5	799.60	69	
11R-1, 149-150	809.19	102	
12R-2, 149-150	820.29	850	
13R-1, 149-150	828.39	241	
14R-3, 149-150	841.09	314	
15R-2, 134-135	849.14	227	
21R-2, 149-150	896.20	5950	1.2
23R-1, 129-130	915.09	5157	1
24R-1, 7-10	923.27	3313	
25R-3, 91-93	936.22	3291	0.7
26R-2, 0-5	938.37	5289	1.1
27R-1, 92-93	942.82	2151	
28R-4, 108-113	951.64	2749	
29R-2, 55-57	953.19	3739	0.7

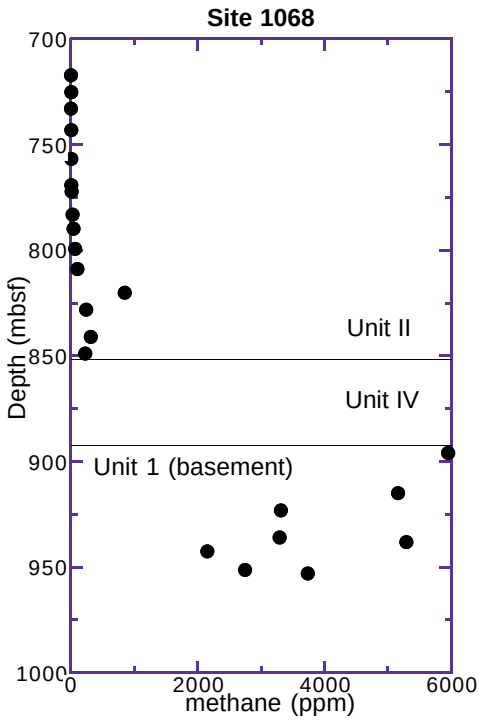

Figure 50. Methane concentrations in headspace gas samples from Hole 1068A. No gas samples were taken from the breccias of Unit IV.

with the Hamilton Frame Velocimeter using split cores and discrete minicore samples. Thermal conductivity measurements were made only on basement samples because split core sediment samples were not competent enough for polishing. Index properties determined for minicore samples include porosity, grain and bulk density, void ratio, and water content. For convenience, physical property data are discussed in two sections: sediments and basement.

Table 14. Interstitial water chemistry data for Hole 1068A.

Core, section, interval (cm)	Depth (mbsf)	SO_4^{2-} (mM)	K^+ (mM)	Cl^- (mM)	Ca^{2+} (mM)	Sr^{2+} (mM)	Mg^{2+} (mM)	Na^+ (mM)	Li^+ (mM)
173-1068A-									
1R-4, 140-150	717.20	2.3	1.73	544	40.2	NA	26.2	410.1	NA
4R-5, 0-11	746.30	2.7	1.6	496	37.3	374	23.4	395.3	535
7R-2, 135-150	772.15	2.8	1.55	541	43.3	416	25.1	424.4	286
11R-3, 0-15	810.70	3.5	1.28	497	43.4	388	19.5	387.4	186

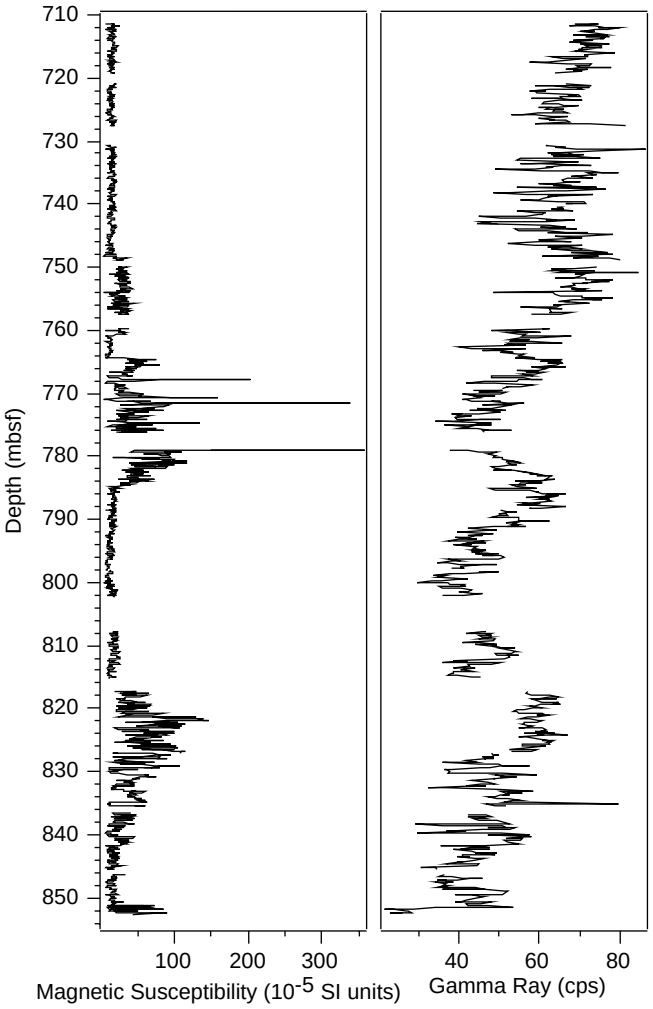

Figure 51. Magnetic susceptibility and natural gamma ray vs. depth in Hole 1068A.

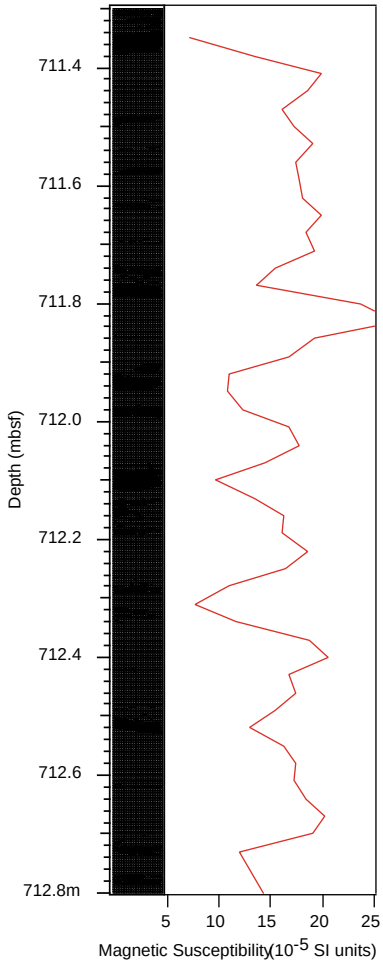

Figure 52. Comparison of magnetic susceptibility and presence of sand layers in Section 173-1068A-1R-1. Sand layers were identified by color from a scanned image of the split core and appear as black patches on the scanned image.

Sediments

Multisensor Track

The magnetic susceptibility and natural gamma radiation of sedimentary rock cores from Hole 1068A are displayed in Figure 51 and listed in Tables 15 and 16 on CD-ROM (back pocket, this volume). Magnetic susceptibility is ~20×10^{-5} SI units above 749 mbsf and increases to ~40×10^{-5} SI units between 749 and 762 mbsf. A thin (3.45 m) local minimum lies above an interval of increased and variable susceptibility between 764 and 785 mbsf. Three peaks within this interval reach greater than 200×10^{-5} SI units. Comparison of individual section susceptibility records with the split core showed that these peaks coincide with very dark brown sediment layers that are on the order of a few centimeters thick. Below 785 mbsf, magnetic susceptibility is again ~20×10^{-5} SI units until an increase at 817 mbsf, coincident with an increase in the abundance of dark brown clay. Magnetic susceptibility returns to lower values below 840 mbsf, with a thin interval of higher values in clays just above basement at 853 mbsf.

Variability of magnetic susceptibility on the scale of the entire cored sediment interval appears to roughly correlate with the abundance of brown (vs. green) clay and claystone. There is also a strong local correlation between magnetic susceptibility and the occurrence of calcareous sandstone layers in the cores. The magnetic susceptibility trace of Section 173-1068A-1R-1 (711.3–712.8 mbsf) is plotted next to a scanned image of the section that has been processed to

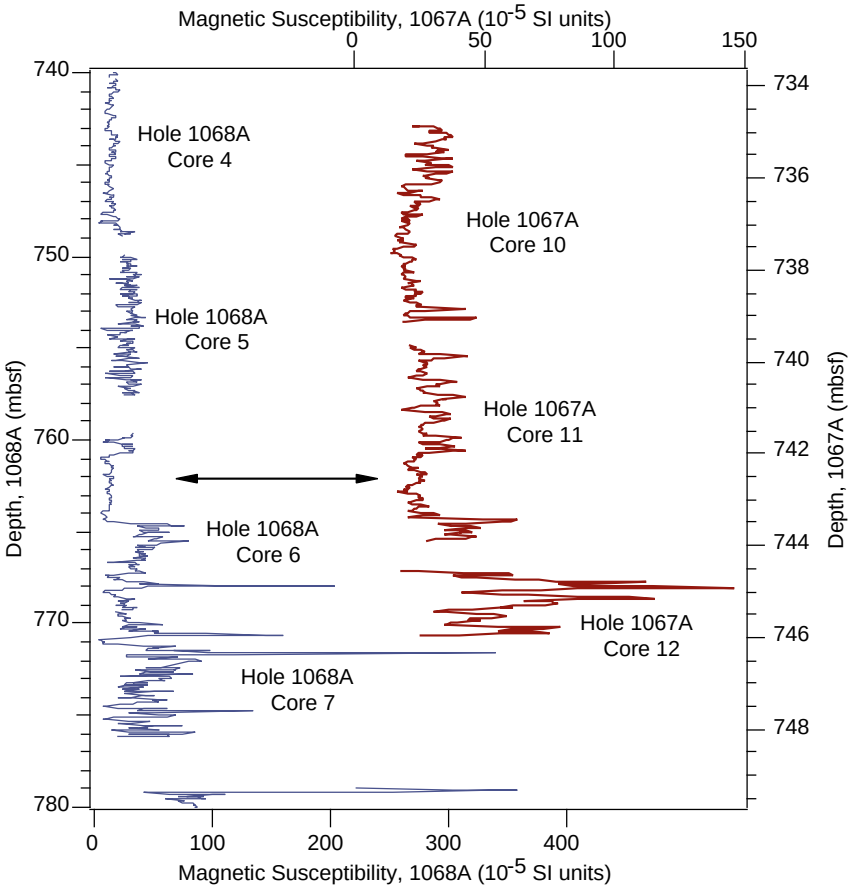

Figure 53. Sections of magnetic susceptibility traces from Hole 1068A and Hole 1067A. Note the different depth and susceptibility scales: Hole 1067A right and top, Hole 1068A left and bottom. Arrow suggests correlation between minima at the 2 sites. Minimum is 3.8 m thick at Site 1068 and 1.4 m thick at Site 1067.

identify light-colored (sandstone) layers in Figure 52, where it can be seen that susceptibility minima generally correlate with sandstone layers (in black on the scanned image).

Magnetic susceptibility traces are also useful in correlating sedimentary intervals between Sites 1068 and 1067. Records from Cores 173-1067A-10R, 11R, and 12R are plotted beside Hole 1068A data in Figure 53. Note that the Hole 1067A depth scale is expanded relative to the depth scale of Hole 1068A to compensate for a higher sedimentation rate at Site 1068 than at Site 1067. The 3.8-m-thick local minimum occurring around 763 mbsf at Site 1068 correlates well with a 1.4-m-thick interval at Hole 1067A centered about 742.5 mbsf (see Fig. 53), suggesting that the sedimentation rate at Site 1068, at least for a particular instant in time, was more than twice that at Site 1067. Other correlations are somewhat less certain, but probable.

Gamma-ray activity shows a general decrease with depth over the cored sediment interval, from values around 70 counts per second (cps) at 711 mbsf to 45 cps above the basement at 852 mbsf (Fig. 51). This trend is probably a reflection of an overall gradual increase in carbonate content with depth (see "Organic and Inorganic Geochemistry" section, this chapter). A local minimum in activity appears to correlate with the interval of increased magnetic susceptibility between 765 and 785 mbsf. Below 800 mbsf, in a reversal of the relationship, 2 local minima and a local maximum in natural gamma radiation coincide with magnetic susceptibility peaks and troughs.

Index Properties

Sediment lithology for the entire cored sediment interval can generally be described as a series of repeating sequences of calcareous

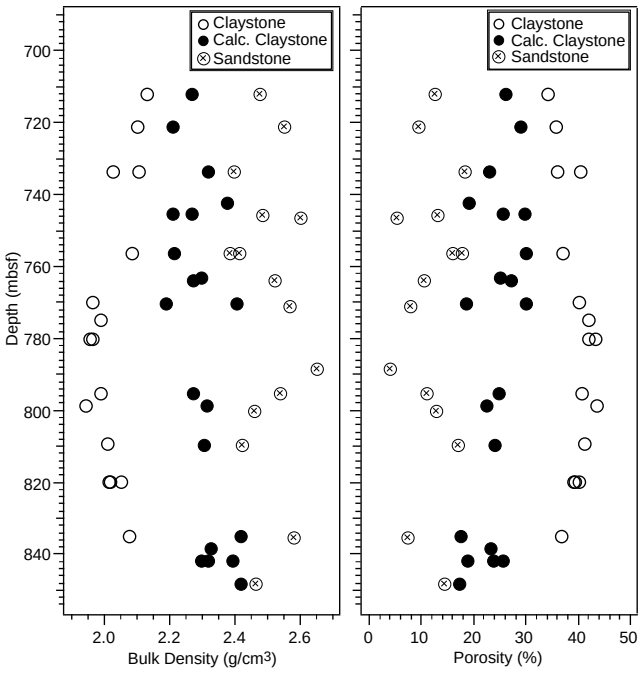

Figure 54. Sedimentary rock bulk density and porosity vs. depth in Hole 1068A.

Table 17. Index properties from Hole 1068A.

Core, section, interval (cm)	Depth (mbsf)	Bulk density (g/cm^3)	Grain density (g/cm^3)	Porosity (%)	Water content (% dry mass)	Lithology
173-1068A-						
Sediments						
1R-1, 51-53	711.81	2.13	2.70	34	16	Claystone
1R-1, 59-61	711.89	2.27	2.70	26	12	Calcareous claystone
1R-1, 63-65	711.93	2.48	2.68	12	5	Sandstone
2R-1, 13-15	721.03	2.10	2.70	36	17	Claystone
2R-1, 19-21	721.09	2.21	2.69	29	13	Calcareous claystone
2R-1, 23-25	721.13	2.55	2.71	9	4	Sandstone
3R-3, 35-37	733.45	2.02	2.70	40	20	Claystone
3R-3, 42-44	733.52	2.11	2.71	36	18	Claystone
3R-3, 50-52	733.60	2.32	2.70	23	10	Calcareous claystone
3R-3, 56-58	733.66	2.40	2.70	18	8	Sandstone
4R-2, 36-38	742.16	2.38	2.69	19	8	Calcareous claystone
4R-4, 42-44	745.22	2.21	2.71	30	14	Calcareous claystone
4R-4, 61-63	745.41	2.27	2.69	26	12	Calcareous claystone
4R-4, 71-73	745.51	2.48	2.70	13	5	Sandstone
4R-5, 22-24	746.52	2.60	2.68	5	2	Sandstone
5R-5, 24-26	756.14	2.09	2.71	37	18	Claystone
5R-5, 31-33	756.21	2.21	2.72	30	14	Calcareous claystone
5R-5, 37-39	756.27	2.41	2.67	16	7	Sandstone
5R-5, 49-51	756.39	2.38	2.68	18	8	Sandstone
6R-3, 62-64	763.22	2.30	2.72	25	11	Chalk
6R-3, 108-110	763.68	2.27	2.73	27	12	Chalk
6R-3, 137-139	763.97	2.52	2.69	10	4	Sandstone
7R-1, 66-68	769.96	1.96	2.59	40	21	Claystone
7R-1, 76-78	770.06	2.19	2.68	30	14	Calcareous claystone
7R-1, 83-85	770.13	2.40	2.72	18	8	Calcareous claystone
7R-2, 30-32	771.10	2.57	2.70	8	3	Sandstone
7R-4, 86-88	774.66	1.99	2.68	42	22	Claystone
8R-1, 108-110	779.98	1.95	2.66	43	23	Claystone
8R-1, 130-132	780.20	1.96	2.64	42	22	Claystone
8R-CC, 2-4	788.55	2.65	2.72	4	2	Sandstone
9R-5, 53-55	795.03	1.99	2.65	41	21	Claystone
9R-5, 67-69	795.17	2.27	2.68	25	11	Calcareous claystone
9R-5, 87-89	795.37	2.54	2.72	11	4	Sandstone
10R-1, 40-42	798.50	1.94	2.64	43	23	Claystone
10R-1, 50-52	798.60	2.31	2.68	22	10	Calcareous claystone
10R-2, 38-40	799.98	2.46	2.67	13	5	Sandstone
11R-2, 15-17	809.35	2.01	2.70	41	21	Claystone
11R-2, 26-28	809.46	2.31	2.71	24	11	Calcareous claystone
11R-2, 37-39	809.57	2.42	2.71	17	7	Sandstone
12R-2, 96-98	819.76	2.02	2.68	40	20	Claystone
12R-2, 100-102	819.80	2.05	2.71	39.1	20	Claystone
12R-2, 104-106	819.84	2.01	2.65	39.3	20	Claystone
13R-6, 52-52	834.92	2.08	2.68	36.6	18	Claystone
13R-6, 68-70	835.08	2.42	2.71	17.5	7	Calc. claystone
13R-6, 81-83	835.21	2.58	2.70	7.2	3	Sandstone
14R-2, 39-41	838.49	2.33	2.72	23.2	10	Calcareous claystone
14R-4, 57-59	841.67	2.30	2.73	25.4	11	Calcareous claystone
14R-4, 67-69	841.77	2.32	2.72	23.7	11	Calcareous claystone
14R-4, 74-76	841.84	2.39	2.71	18.8	8	Calcareous claystone
15R-2, 42-44	848.22	2.42	2.71	17.3	7	Calcareous claystone
15R-2, 51-53	848.31	2.46	2.70	14.4	6	Sandstone
173-1068A-						
Acoustic basement						
16R-6,78	863.50	2.64	2.72	4.8	2	Subunit IVA
17R-1, 26	865.86	2.70	2.77	4.2	2	Subunit IVA
18R-2, 103	871.55	2.64	2.80	8.6	3	Subunit IVA
19R-3, 76	878.38	2.49	2.76	15.3	6	Subunit IVA
19R-4, 6	879.18	2.52	2.72	11.8	5	Subunit IVB
20R-2, 47	886.23	2.47	2.61	8.9	4	Subunit IVB
21R-2, 100	895.71	2.21	2.58	23.8	11	Subunit 1B
22R-1, 82	905.02	2.28	2.59	19.8	9	Subunit 1B
23R-1, 41	914.21	2.43	2.62	12.1	5	Subunit 1B
24R-1, 65	923.85	2.38	2.58	12.6	5	Subunit 1B
25R-2, 92	935.02	2.37	2.60	15	7	Subunit 1B
26R-1, 112	938.12	2.45	2.54	5.3	2	Subunit 1B
26R-2, 66	939.03	2.37	2.60	14.4	6	Subunit 1B
28R-2, 56	948.42	2.47	2.60	7.7	3	Subunit 1B
29R-3, 94	954.45	2.45	2.57	7.6	3	Subunit 1B

sandstone overlain by calcareous claystone (sometimes chalk), and ultimately topped by a low-carbonate claystone (see "Lithostratigraphy" section, this chapter). As mentioned above, color (red or green) of the calcareous claystones and claystones appears to have some relation to magnetic susceptibility over the total interval, but does not seem to correlate with differences in sediment index properties. Accordingly, we have divided our samples into the three lithologic types for purposes of discussion, regardless of color, keeping in mind that in general the boundaries between each rock type are gradational.

Profiles of sample wet bulk density and porosity are plotted vs. depth below seafloor in Figure 54 and are listed in Table 17. The three lithologies at each depth exhibit a regular relationship, with the claystones having the lowest density and greatest porosity, while the sandstones have the highest densities and the lowest porosities. Claystone porosity appears to increase slightly with depth, from around 35% at the top of the drilled interval to 40% or more just above basement. Density of the claystones correspondingly decreases, from 2.15 g/cm^3 at the top of the section to 1.95 g/cm^3 near the bottom. Calcar-

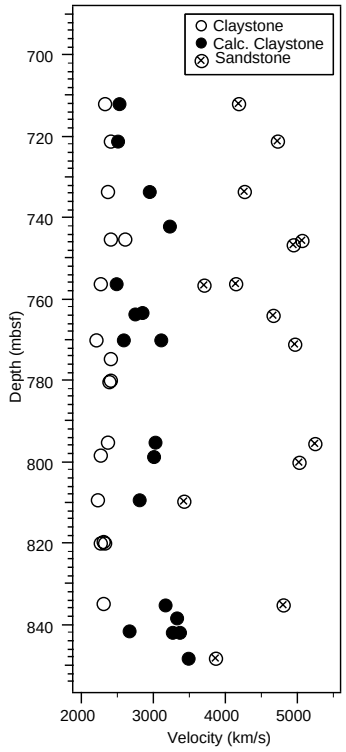

Figure 55. Sedimentary rock compressional-wave velocity vs. depth in Hole 1068A.

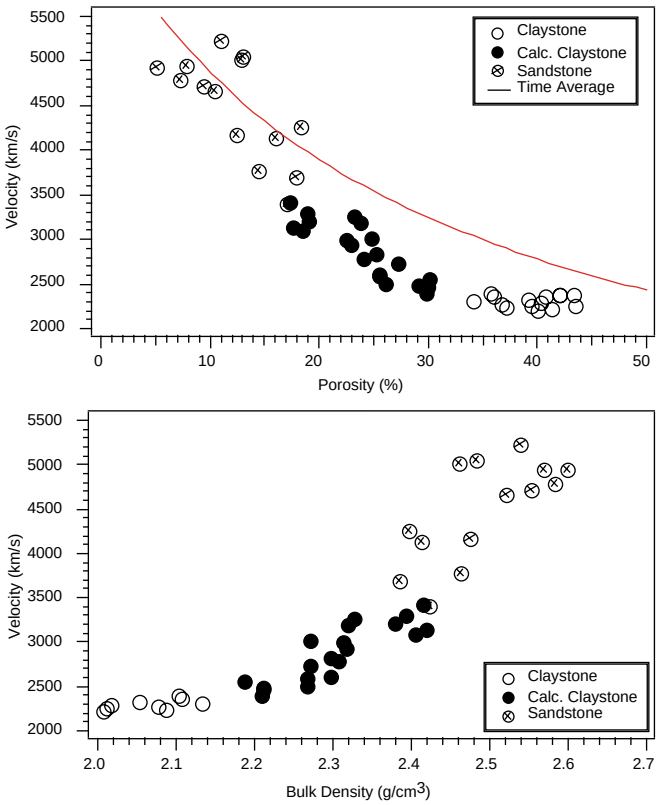

Figure 56. Bulk density and porosity vs. compressional-wave velocity for sedimentary rock at Hole 1068A.

Table 18. Compressional wave velocities from Hole 1068A.

Core, section, interval (cm)	Depth (mbsf)	Velocity (m/s)	Lithology
173-1068A-			
Sediments			
1R-1, 51	711.81	2307	Claystone
1R-1, 59	711.89	2500	Claystone
1R-1, 63	711.93	4144	Sandstone
2R-1, 13	721.03	2393	Claystone
2R-1, 19	721.09	2488	Claystone
2R-1, 23	721.13	4687	Sandstone
3R-3, 42	733.52	2355	Claystone
3R-3, 50	733.60	2922	Calc. claystone
3R-3, 56	733.66	4231	Sandstone
4R-2, 36	742.16	3200	Calcareous claystone
4R-4, 42	745.22	2398	Claystone
4R-4, 61	745.41	2584	Calcareous claystone
4R-4, 71	745.51	5008	Sandstone
4R-5, 22	746.52	4892	Sandstone
5R-5, 24	756.14	2242	Claystone
5R-5, 31	756.21	2466	Calcareous claystone
5R-5, 37	756.27	4118	Sandstone
5R-5, 49	756.39	3674	Sandstone
6R-3, 62	763.22	2822	Chalk
6R-3, 108	763.68	2725	Chalk
6R-3, 137	763.97	4629	Sandstone
7R-1, 66	769.96	2200	Claystone
7R-1, 76	770.06	2558	Calcareous claystone
7R-1, 83	770.13	3084	Calcareous claystone
7R-2, 30	771.10	4905	Sandstone
7R-4, 86	774.66	2378	Claystone
8R-1, 108	779.98	2385	Claystone
8R-1, 130	780.20	2371	Claystone
9R-5, 53	795.03	2352	Claystone
9R-5, 67	795.17	3001	Calcareous claystone
9R-5, 87	795.37	5192	Sandstone
10R-1, 40	798.50	2256	Claystone
10R-1, 50	798.60	2991	Calcareous claystone
10R-2, 38	799.98	4988	Sandstone
11R-2, 15	809.35	2219	Claystone
11R-2, 26	809.46	2787	Calcareous claystone
11R-2, 37	809.57	3392	Sandstone
12R-2, 96	819.76	2288	Claystone
12R-2, 100	819.80	2319	Claystone
12R-2, 104	819.84	2256	Claystone
13R-6, 52	834.92	2292	Claystone
13R-6, 68	835.08	3154	Calcareous claystone
13R-6, 81	835.21	4802	Sandstone
14R-2, 39	838.49	3322	Calcareous claystone
14R-4, 57	841.67	2655	Claystone
14R-4, 67	841.77	3256	Calcareous claystone
14R-4, 74	841.84	3365	Calcareous claystone
15R-2, 42	848.22	3485	Calcareous claystone
15R-2, 51	848.31	3862	Sandstone
173-1068A-			
Acoustic basement			
16R-1, 57	856.47	5953	Subunit IVA
16R-2, 42	857.71	5739	Subunit IVA
16R-2, 42	857.71	4961	Subunit IVA
16R-3, 103	859.76	6443	Subunit IVA
16R-4, 40	860.25	4584	Subunit IVA
16R-6, 76	863.48	5114	Subunit IVA
16R-6, 76	863.48	5114	Subunit IVA
16R-6, 96	863.68	5313	Subunit IVA
17R-1, 63	866.23	5358	Subunit IVA
17R-2, 32	867.28	5304	Subunit IVA
17R-4, 70	869.30	4742	Subunit IVA
17R-4, 70	869.30	5604	Subunit IVA
19R-1, 70	875.90	5420	Subunit IVA
19R-4, 6	879.18	4467	Subunit IVB
20R-2, 47	886.23	5013	Subunit IVB
20R-6, 35	890.93	5588	Subunit IVB
21R-2, 97	895.68	2664	Subunit 1B
22R-1, 51	904.71	2680	Subunit 1B
22R-1, 86	905.06	2867	Subunit 1B
22R-1, 88	905.08	2913	Subunit 1B
22R-2, 22	905.92	2786	Subunit 1B
22R-2, 65	906.35	3120	Subunit 1B
23R-1, 44	914.24	3368	Subunit 1B
23R-1, 84	914.64	3490	Subunit 1B
24R-1, 92	924.12	3630	Subunit 1B
24R-2, 51	924.92	3693	Subunit 1B
25R-1, 107	933.67	3677	Subunit 1B
25R-2, 92	935.02	3542	Subunit 1B
25R-2, 107	935.17	3529	Subunit 1B
25R-3, 47	935.78	4469	Subunit 1B
26R-1, 115	938.15	4490	Subunit 1B
26R-2, 65	939.02	5289	Subunit 1B
26R-2, 92	939.29	3787	Subunit 1B
26R-2, 116	939.53	3309	Subunit 1B
26R-4, 27	941.20	3584	Subunit 1B

eous claystone densities generally vary between 2.2 and 2.4 g/cm^3 while sandstone densities vary between 2.4 and 2.6 g/cm^3. Porosities range from 2% to 18% in sandstones and from 18% to 30% in the claystones. Neither lithology appears to have any particular trend of density or porosity change with depth. Grain densities are clustered around 2.7 g/cm^3 (Table 17).

Acoustic Velocity

Compressional-wave velocity is plotted vs. depth below seafloor in Figure 55 and listed in Table 18. Neither the sandstones nor the claystones exhibit any obvious trend with depth, while the calcareous claystone profile suggests a slight increase in velocity towards the bottom of the drilled interval. Velocity plotted vs. density and porosity (Fig. 56) reveals regular relationships of increasing velocity with increasing density and decreasing porosity. Compressional-wave velocity of the claystones shows little variability, with values tightly grouped between 2300 and 2500 m/s. Calcareous claystones range from 2400 to 3400 m/s while sandstones have the highest and most variable velocity between 3400 and 5300 m/s. The superimposed time average line represents the velocity-porosity relationship expected from well-cemented calcareous sandstones or claystones (Wyllie et al., 1956). The line was calculated using calcite as a matrix material. Data falling well below the curve are most easily interpreted as poorly cemented aggregates of grains/sediments rather than rocks.

Acoustic Basement

Multisensor Track and Thermal Conductivity

Magnetic susceptibility was measured on basement lithologies starting with 173-1068A-15R-5 (Subunit IVA). For a comprehensive discussion of magnetic susceptibility results, see "Paleomagnetism" section (this chapter). Natural gamma radiation was also measured on basement lithologies. The data reflect very low concentrations of Th, K, and U with amplitudes between 20 and 40 cps in the sedimentary breccias (Unit IV) and below 20 cps in the serpentinized peridotites (Unit 1; Fig. 57). These values are as much as 75% lower than those of the overlying sedimentary units.

Thermal conductivities were measured only on five samples from basement lithologies in Hole 1068A (Table 19 on CD-ROM, back pocket, this volume). Breccia units were sampled once every other core, and conductivities were measured on two serpentinized peridotite samples. The incompetence of serpentinized peridotites in Subunits 1A and 1B prohibited a lesser sampling interval. The serpentinized peridotites show the lowest values (1.57 W/[m·K] and 1.656 W/[m·K]) of thermal conductivity in basement units at this site. The breccias of Subunit IVA show somewhat higher conductivities with a range of 1.754 W/(m·K) to 1.804 W/(m·K).

Index Properties

The acoustic basement cores at Hole 1068A comprise Unit IV and Unit 1. Unit IV comprises Subunits IVA, IVB, and IVC (see "Lithostratigraphy" section, this chapter). These subunits are dominated by sedimentary breccias containing abundant igneous and metamorphic clasts. For the purpose of index properties measurements, only the most fine-grained breccias were discretely sampled. This sampling procedure was followed to ensure accurate measurements of complete lithologies (the whole medium) and to avoid measuring properties of clasts alone. Below sedimentary Subunits IVA, IVB, and IVC, serpentinized peridotite dominates. This basement lithology is subdivided into Subunits 1A and 1B (see "Igneous and Metamorphic Petrology" section, this chapter). In Subunits 1A and 1B, only the most competent sections were sampled for index properties.

Bulk density and porosity values for basement lithologies are summarized in Table 17 and Figure 58. Porosities for all three basement units are comparable and range from approximately 5% to 24%. Bulk densities are distributed less uniformly across lithologic boundaries. The serpentinized peridotites of Subunits 1A and 1B have slightly lower bulk densities (2.21 to 2.45 g/cm^3) than the overlying breccia units, which have densities that range from 2.47 to 2.70 g/cm^3. The low bulk densities of the serpentinized peridotite units re-

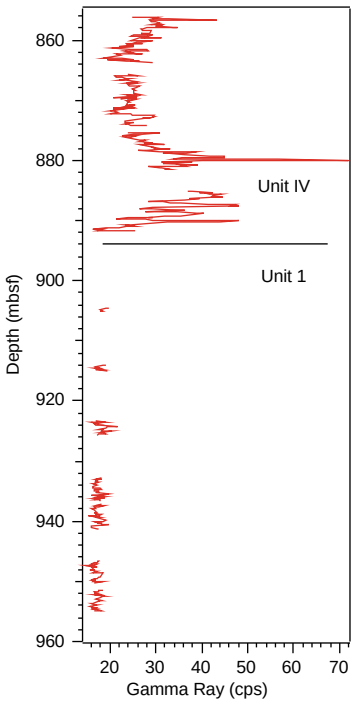

Figure 57. Basement natural gamma ray data vs. depth in Hole 1068A.

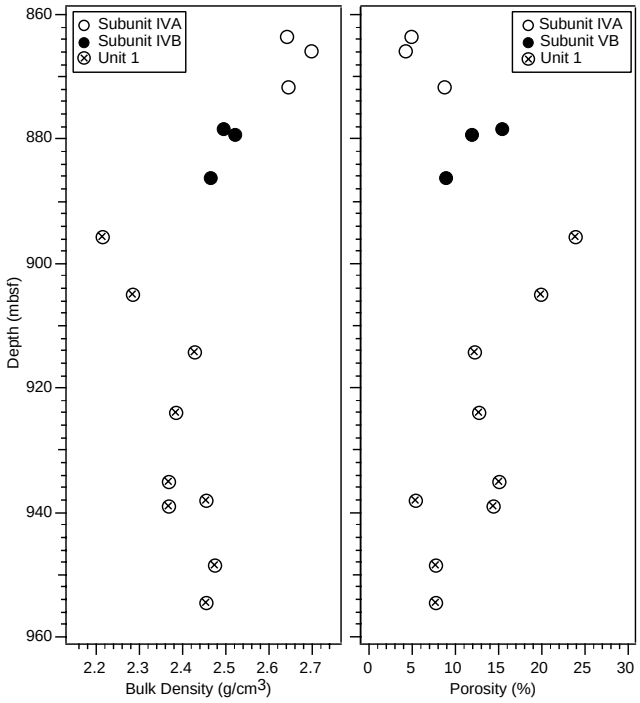

Figure 58. Basement bulk density and porosity vs. depth in Hole 1068A.

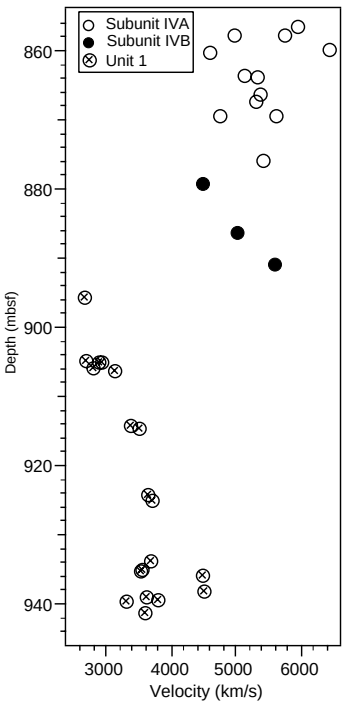

Figure 59. Basement compressional-wave velocity vs. depth in Hole 1068A.

flect a lower grain density than the overlying breccia units. The grain densities average 2.73 g/cm^3 for the Unit IV breccias compared to an average of 2.59 g/cm^3 for the underlying serpentinized peridotites.

Acoustic Velocities

The relationship between velocity and depth is illustrated in Figure 59 and Table 18. Basement lithologies show a decrease in velocity at a depth of 896 mbsf. This acoustic boundary (5588 m/s above to 2664 m/s below) coincides with the onset of serpentinized peridotite in Core 173-1068A-21R-2. The lower velocities of the serpentinized peridotites in Subunits 1A and 1B are most likely a result of their high fracture porosity and not their degree of serpentinization. The compressional-wave velocity of pure (100%) serpentinite is approximately 5000 m/s; however, no velocity near 5000 m/s was measured for Unit 1. This further substantiates the dependence of velocities on the degree of fracturing. Bulk density and porosity are plotted vs. velocity in Figure 60. The data show the expected correlations with velocity increasing with increasing bulk density and decreasing porosity. One outlier, labeled "A" in Figure 60, is a result of sampling a massive unfractured serpentinized peridotite from Subunit 1B.

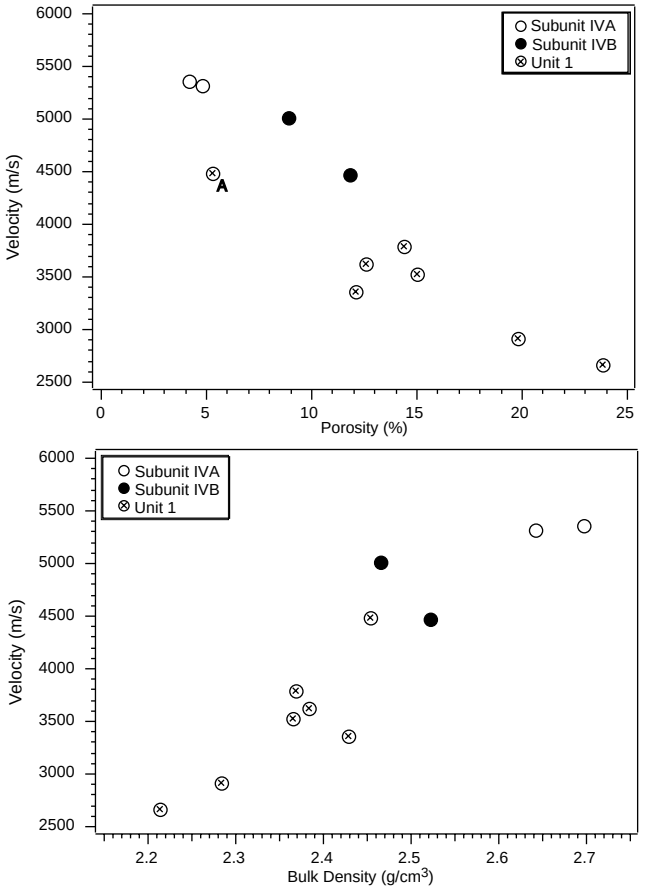

Figure 60. Bulk density and porosity vs. compressional-wave velocity for basement rocks from Hole 1068A. A = massive and unfractured serpentinized peridotite from Subunit 1B.

Table 20. Logging operations at Site 1068.

Tool run	Operation depth	Depth (mbrf)
1	Driller's depth	6010.8
	Depth reached by tool	5562
	Driller's pipe	5169
	Logger's pipe	5169
	Driller's seafloor	5055
	Logger's seafloor	5045
2	Driller's depth	6010.8
	Depth reached by tool	5823
	Driller's pipe	5669
	Logger's pipe	5669

DOWNHOLE MEASUREMENTS

After drilling and coring Hole 1068A to a total depth (TD) of 6010.8 mbrf (955.8 mbsf) using an RCB coring system, a complete wiper trip was made to condition the hole for logging. Additional cuttings were removed from the borehole by circulating sepiolite mud (see "Operations" section, this chapter).

Wireline logging operations began in Hole 1068A at 04:00 on 21 May 1997. All logging operations were completed 17 hr later. Only one logging tool string, the triple combination (see "Downhole Measurements" section, "Explanatory Notes" chapter, this volume), was used at Site 1068 because of bridging complications and time constraints. Because bridges were present, the hole was logged in two different runs: the first run from 507 to 114 mbsf and the second run from 768 to 614 mbsf. For the second run, the pipe was lowered below the bridge encountered during the first run at 530 mbsf (see Table 20 for logging and drilling depth information). The triple combination tool was run at a speed of ~600 m/hr during both logging runs. An overview of the logging operations can be seen in Table 21.

The triple combination tool string included, from top to bottom, the telemetry cartridge, HNGS, APS, HLDT, DIT, and the TLT. The data collected by the triple combination are of good quality. From the caliper log (11 to 15 in), the borehole was considered to be in good condition, except between 360 and 440 mbsf (6 to 13 in). All logging data were shifted from meters below rig floor (mbrf) to meters below seafloor (mbsf) using the driller's water depth for preliminary shipboard analysis.

Table 21. Depth parameters at Site 1068 from log and drilling operations.

Date	Time (GMT)	Activity
5/21/97	4:00	Rig up wireline and triple combination tool string
	6:00	Run in hole with triple combination (TLT/DIT/HLDT/APS/HNGS)
	9:15	Began upward log from total depth (TD) (5562 mbrf)
	10:00	Pipe depth (PD; 5169 mbrf) reached; tool is run to seafloor with HNGS running
	12:30	Tool out of drill string and rig down
	13:30	Lower pipe to below bridge (new PD 5669 mbrf)
	14:30	Rig up triple combination for the second run
	14:30	Run in hole to TD (bridge encountered at 5823 mbrf)
	17:45	Log up to PD
	18:05	Tool enters pipe
	20:30	Tool out of drill string
	21:00	Rig down finished; end of logging operation

Geophysical Logging Data

Downhole measurements from Hole 1068A provide geophysical and geochemical (U, Th, K) data, covering the intervals from 614 to 768 mbsf and from 114 to 507 mbsf (Figs. 61, 62). The upper run covered Miocene and Oligocene sediments previously cored and described at Site 900 as lithostratigraphic Subunits IC, IIA and IIB (see Shipboard Scientific Party, 1994c; see Fig. 1, "Lithostratigraphy" section, this chapter). Subunit IC, which is described as a nannofossil claystone, claystone, nannofossil ooze sequence, may be identified in the logs above 160 mbsf. This sequence shows natural gamma-ray values fluctuating mostly between 50 and 75 API units, an increasing density with depth from 1.5 to 1.8 g/cm^3 and a relatively stable resistivity around 1 Ωm (Fig. 62). These values, coupled with a low Th concentration, are consistent with the relatively unconsolidated nannofossil-rich sequence described during Leg 149. A transition to Subunit IIA (53 m thick at Site 900) can be inferred below 160 m from the log data, which shows relatively constant values of density (1.8–1.9 g/cm^3), resistivity (1.4 Ωm) and the photoelectric effect factor (3.3 barn/e$^-$; see Fig. 62). Subunit IIA was described as a sequence of nannofossil claystone and nannofossil chalk. The logging data are consistent with these lithologies, especially the low Th values, and suggest a high nannofossil/pelagic input to this sequence. Below 260 mbsf, a distinct increase can be seen in the natural gamma-ray log to 85–90 API units, which is mostly a response to increased Th (see Fig. 61). This supports the transition to lithostratigraphic Subunit IIB described at Site 900 as a 515-m-thick silty claystone to clayey siltstone, nannofossil claystone, and claystone sequence and, at Sites 1065, 1067, and 1068 during Leg 173, as a nannofossil chalk (dominant) and nannofossil clay lithology. Logging data show an increasing density and resistivity throughout this subunit, with some local variations, probably caused by distinct changes in lithology or in borehole environment, such as, for example, the borehole diameter (see caliper curve between 350 and 450 mbsf, Fig. 61).

The lower run (768 to 614 mbsf) partially covers the cored interval at this site. The interval contains Eocene sediments, described as lithostratigraphic Subunits IIB and IIC (see "Lithostratigraphy" section, this chapter), which have variable amounts of claystone, calcareous claystone, nannofossil chalk, and calcareous sandy siltstones, and represent recurring contourite, turbidite, and hemipelagic depositional episodes. No clear boundary could be identified from the logging data at 730 mbsf, corresponding to the contact of Subunit IIB/Subunit IIC described from the cores (see Fig. 2, "Lithostratigraphy" section, this chapter). However, from the logging data a lithologic boundary is proposed at 710 mbsf where increases in resistivity and density coincide with a reduced porosity. These changes may be a result of the increased proportion of sedimentary Motif 4 (see "Lithostratigraphy" section, this chapter), which includes indurated calcareous fine-medium quartz sand, foraminifer/quartz sand, lithoclast sand, and conglomerate facies.

During Leg 149, gamma-ray and resistivity logging data were recorded in Hole 900A between 238 and 137 mbsf and between 451 and 330 mbsf (Shipboard Scientific Party, 1994c). Preliminary comparison of total gamma-ray counts and deep resistivity logging data from Holes 900A and 1068A suggests a good lithologic correlation (Fig. 63). Accepting these correlations and comparing both sets of data from both holes show that the sedimentation rates are different in Holes 900A and 1068A. However, some comparable intervals show similar rates of sedimentation. In the upper logged interval (Hole 900A depths: 135–205 mbsf), a slightly more condensed section for Hole 1068A is seen, with a reduced section of sediment at about 160 mbsf. The sedimentation rates for the lower logged interval are very similar; however, these sections are offset by approximately 35 m, and this sedimentary section is shallower in Hole 1068A. De Kaenel and Villa (1996) proposed the presence of a condensed sedimentary section at Hole 900A at about 230 mbsf. Comparing similar sequences allows us to suggest that, between 190 and 300 mbsf in Hole 1068A, the sedimentary sequence is more condensed or that the sedimentation rate was lower than in Hole 900A.

Borehole Temperature

Figure 64 shows the temperature vs. depth profile for the two runs of the triple combination tool string. The temperature gradient is relatively constant over the complete logged interval; however, these data indicate a lower geothermal gradient than expected: 15°C/km from 385 mbsf to the pipe depth for the first uplog run, and 17.5°C/km out of the pipe for the second uplog run. Such low gradients are probably caused by fluid circulation during drilling operations which has prevented the borehole from reaching thermal equilibrium.

SUMMARY AND CONCLUSIONS

Summary

The history of this site began with the formation of the 71-m-thick peridotite section, which is now almost entirely serpentinized, and of the overlying intrusive meta-igneous rocks, inferred to exist from the breccia clasts and from our knowledge of cores from Sites 900 and 1067. It is difficult at this stage to decipher the entire sequence of events that the peridotite and meta-igneous rocks have experienced. In the following, only the current state of these rocks, and the most obvious inferences about how they reached that state, are summarized.

The former composition and texture of the peridotites are hardly recognizable because of the strong serpentinization of the rocks (up to 99%). Only some original spinels and a few relicts of clinopyroxene are preserved. Serpentine replaces the olivine and pyroxene crystals, and chlorite patches around spinels may be derived from former plagioclase. These observations indicate that the mantle rocks were,

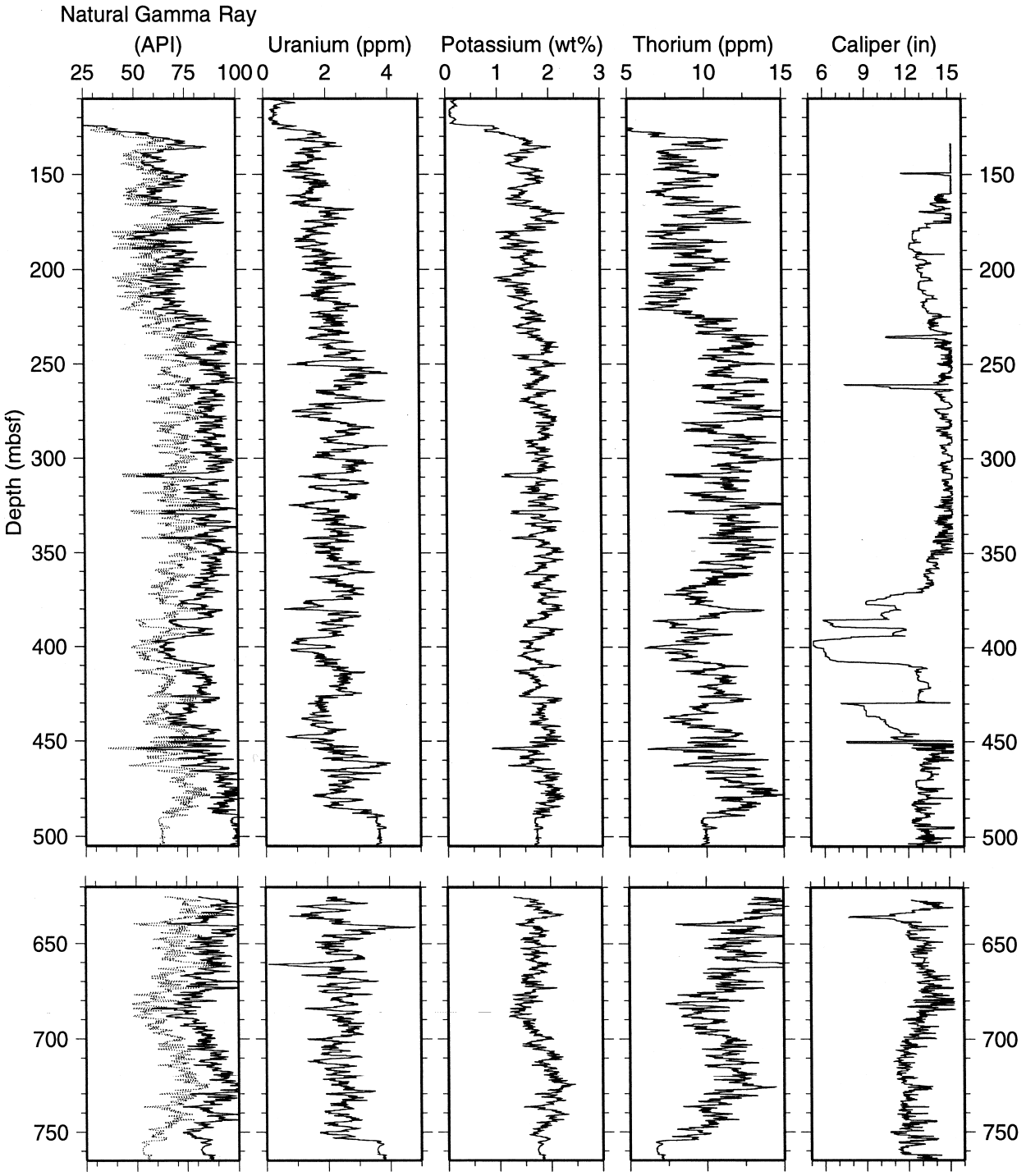

Figure 61. Downhole logs from the HNGS natural gamma-ray tool and caliper from the HLDT, recorded during the two runs of the triple combination tool string. Depths are in mbsf: natural gamma ray (continuous line = total gamma-ray; dotted line = computed gamma-ray [total gamma-ray minus uranium]), uranium, potassium, and thorium.

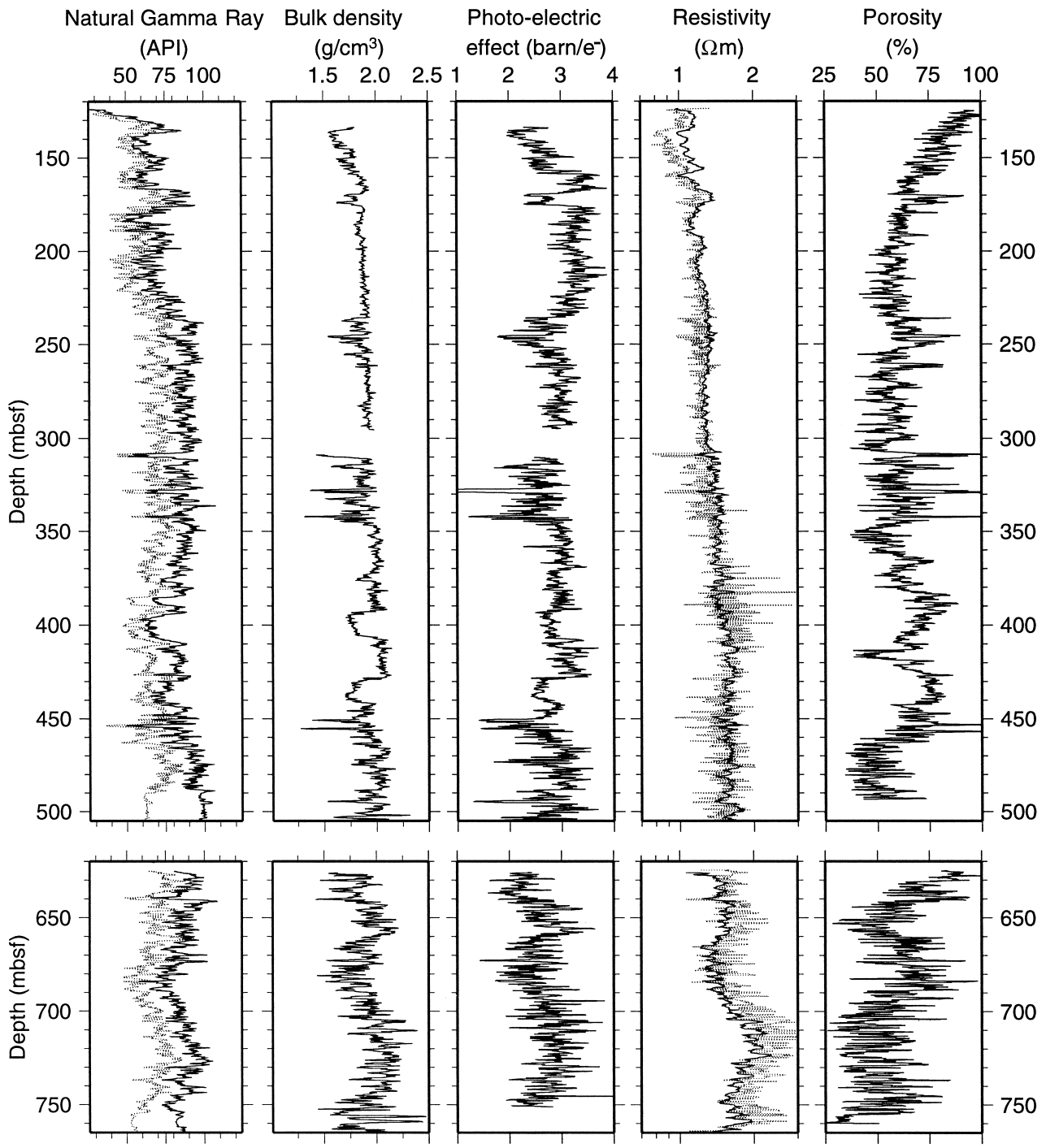

Figure 62. Downhole logs of natural-gamma ray (continuous line = total gamma-ray; dotted line = computed gamma-ray [total gamma-ray minus uranium]), bulk density, photo-electric effect factor, resistivity (ILD = continuous line and SFLU = dotted line) and porosity recorded during the two runs of the triple combination tool string.

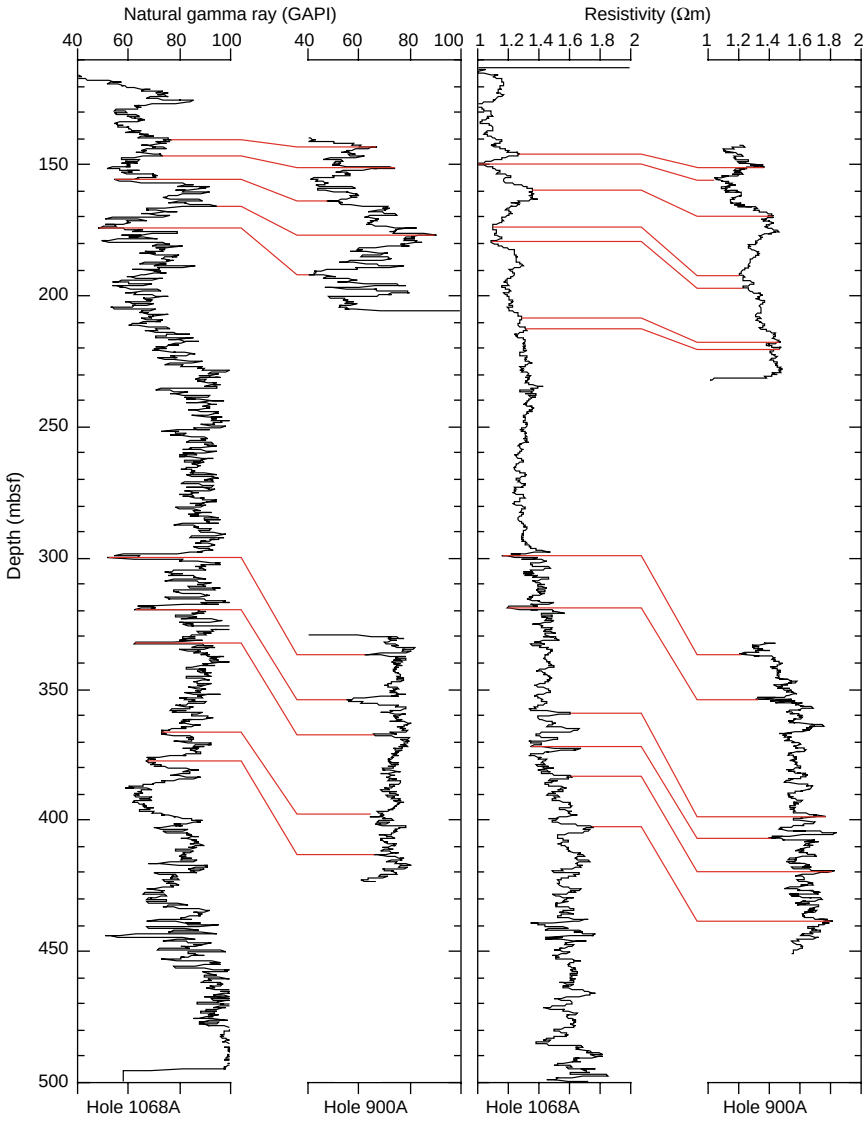

Figure 63. Comparison between total natural gamma-ray and deep resistivity logging data from Holes 900A and 1068A.

at least locally, plagioclase and spinel-bearing lherzolite. The proportion of ghost pyroxenes is highly variable in the rocks, indicating a high heterogeneity of the mantle, from harzburgite and/or lherzolite to olivine pyroxenite and dunite. A high-temperature foliation is defined in most of the cored section, mainly by the alignment of elongated spinels and rims of chlorite. No evidence for mylonitic deformation can be observed in the cored section. The widespread and very pervasive serpentinization, contemporaneous with an intense serpentine veining of the rocks, was the latest event during the evolution of the rocks. It is presumed to have occurred as the lithospheric thinning that accompanied rifting brought the mantle peridotite near the surface within reach of hydrothermally driven circulating seawater. According to these observations, the mantle rocks at Site 1068 seem to be comparable to those cored at Site 897 (Leg 149), the evolution of which is compatible with uplift under a rift zone (Agrinier et al., 1996; Beslier et al., 1996; Cornen et al., 1996b; Milliken et al., 1996):

1. Limited partial melting under spinel facies conditions that was followed by some impregnation by melt products during the last stages of a high-temperature (around 900°C) shear deformation event;
2. Subsolidus re-equilibration during ongoing ductile shear deformation under lithospheric conditions, which ceased at a temperature close to 735°C (this deformation stage has not been observed so far in Site 1068 peridotite); and
3. A complex and intense deformation, which occurred under subsurface conditions during the serpentinization of the rocks.

The other basement lithologies occur as clasts in the overlying breccia, mainly as metagabbro, amphibolite, and less abundant meta-anorthosite and tonalite gneiss. The preliminary shipboard geochemical results show that the protoliths for the metagabbro and amphibolite formed from differentiated mafic magmas with incompatible trace element abundances between those in normal and enriched MORB. Their compositions appear to lie within a continuum of compositional variation defined by the primitive Site 900 metagabbro and the evolved Site 1067 amphibolite. These compositions are most similar to that of the Site 899 metamicrogabbro, which was sampled as clasts of a mass-flow deposit (Cornen et al., 1996a; Shipboard Scientific Party, 1994b). The meta-igneous rocks all experienced a retrometamorphic evolution from an upper amphibolite facies to greenschist facies conditions. The metagabbro displays textural attributes that suggest that granulite facies pyroxene-bearing assem-

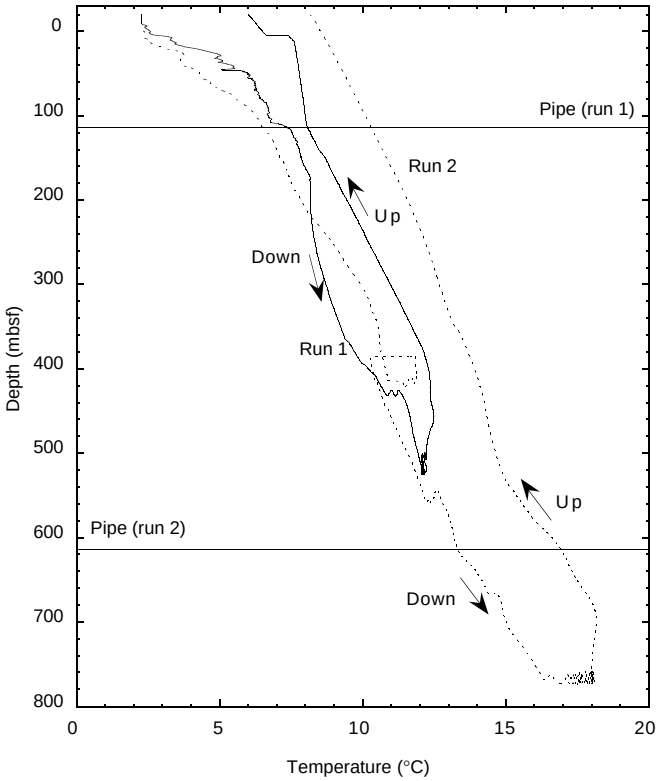

Figure 64. Temperature logs from the TLT, recorded during the two runs of the triple combination tool string (run 1 = continuous line, run 2 = dashed line). The horizontal lines represent the pipe depths for each run.

blages, similar to those encountered at Site 900 (Leg 149; Cornen et al., 1996a), were overprinted during the lower grade metamorphic stages. The amphibolites are comparable to those of the lower part of the section cored at Site 1067, but display a clear foliation and textures, both suggesting a higher grade of metamorphism and a more intense ductile deformation at this site. The magmatic texture observed in other clasts suggests, however, that this deformation was heterogeneous. The latest nonpervasive, more or less static, greenschist facies overprint is comparable in all the meta-igneous rocks.

At some stage in the rifting process extensional tectonics in the upper lithosphere brought the peridotite and meta-igneous rocks close to the seabed. A normal fault delimited the west flank of the Hobby High (the basement high on which Sites 900, 1067, and 1068 lie has been named after a pair of hobbies, or sparrow hawks, that joined the ship while we were drilling Sites 1067 and 1068). It uplifted and exposed the meta-igneous rocks that constitute the breccia clasts and tectonized the peridotite to generate the peridotite breccia, which subsequently became lithified fault gouge.

The sedimentary history of this site began with the deposition of the 27.5-m-thick talus or rockfall deposits that make up lithostratigraphic Subunits IVC and IVB. Judging by the clasts, these deposits must have been intimately involved in the tectonic exposure at the seabed, and brittle deformation, of the mafic and ultramafic rocks that constitute the Hobby High. The location of Site 1068 on the upper west flank of the high, the north-northeast–south-southwest orientation of the high, and the form of the seismic section over the site (Fig. 10, "Introduction" chapter, this volume; Fig. 1, "Site 1067" chapter, this volume) suggest that the site lay over a fault scarp exposing the footwall of a west-dipping normal fault. The base of Subunit IVC appears to be separated from the underlying serpentinized peridotite by a tectonic contact. This interpretation is supported by the observations that Subunit IVC exhibits decreasing signs of brittle deformation upward and away from its base and that at the base there is a weak foliation defined by elongate and sheared clasts.

The breccia clasts are typically angular and up to 1–6 cm in diameter. Thus, the metagabbro and meta-anorthosite clasts of lithostratigraphic Subunit IVC and the predominant, variably foliated amphibolite, micro-amphibolite, and metagabbro clasts of Subunit IVB probably represent fragments of rocks exposed higher up the fault scarp. More than one depositional event may have been responsible for the deposition of Subunit IVB, which consists of clast-supported breccias. The matrix of Subunit IVC consists of a variably cataclastic fine-grained matrix of chlorite, albite, and calcite and that of Subunit IVB is a calcareous mud with fine-grained rock fragments. The percentage of matrix is variable but generally decreases upward from 70% at the top of Subunit IVC to 20%–30% at the top of Subunit IVB (and in Subunit IVA). The breccias of Subunit IVC and towards the base of Subunit IVB were subsequently exposed to fluid-rock interaction and those of Subunit IVC have been subjected to significant hydrothermal alteration and cataclasis, probably concurrently and during the later stages of serpentinization of the underlying peridotite.

A 14-m-thick series of debris flows (Subunit IVA) was deposited on top of the breccias. There were at least three flows as suggested by differences in the composition of the depositional matrix of Early Cretaceous (tentatively Valanginian to Barremian) calcareous chalk. The breccias are matrix to clast supported. A few clasts (of Late Jurassic to earliest Cretaceous calpionellid limestone and biotite schist) that occur near the top of Subunit IVA appear to have come from a source more distant than the Hobby High. Other clasts are angular fragments of variably foliated amphibolite, metagabbro, and meta-anorthosite, presumably of a more local origin. Several explanations can be proposed for the lack of the hydrothermal overprint, which affects Subunit IVC and the base of Subunit IVB, on the upper part of Subunit IVB and all of Subunit IVA. First, hydrothermal activity could have ceased before the deposition of the upper Subunit IVB breccias. Second, hydrothermal activity may simply have failed to extend far enough away from the fault zone to affect Subunit IVA and upper Subunit IVB.

The different mechanisms that have been proposed to produce lithostratigraphic Subunit IVA and Subunits IVB and IVC imply an angular unconformity between them. Talus and rockfall deposits, such as Subunits IVC and IVB, are essentially local deposits, with a relatively steep angle of repose, whereas the Subunit IVA debris flow is more likely to have come to rest at the margin of the north-south sedimentary basin flanking the Hobby High to the west (but see next paragraph).

A hiatus of about 50 m.y. then followed between deposition of the Valanginian(?)–Barremian(?) debris flows and the onset of the Maastrichtian to Cenozoic turbidite/hemipelagite sequence. This long interval is hard to explain if in fact Subunit IVA was deposited on the flank of Hobby High where abyssal plain sediments abutted the high. In this case, one has to postulate the deposit having been laid down above the plain by the debris flow running up some tens of meters above the plain; for example, a run up of 30 meters would have required an average sedimentation rate of 0.6 mm/yr for Subunit IVA to have remained unburied for the following 50 m.y. Alternatively, the debris flows may have traveled downhill from elsewhere on the Hobby High. In doing so they may have filled local depressions and smoothed the surface of the slope to the extent that stable and permanent accumulations of pelagic drape could not form. However, under this scenario the incorporation of rare clasts of limestone and schist is then harder to explain.

The onset of sedimentation in the Maastrichtian heralded the beginning of sedimentation in a continental rise/abyssal plain environment that lasted more or less continuously until the present. These Subunit IIC sediments are a mixture of lighter colored, more carbonate-rich chalk, claystone, and silty claystone turbidite material (in

beds up to 45 cm thick) that typically get darker upward as the sediment grades into brown to dark greenish gray hemipelagic claystones. This sequence is repeated many times on a scale of tens of centimeters. The sediments contain quite complex permutations of a number of lithologic "motifs". There are also occasional beds, up to 13 cm thick and with sharp tops, of sandy siltstone and sandstone. Some of these are composed of coarse lithic sandstone and conglomerate with clasts of shallow-water limestone, chalk, and continental basement rocks clearly pointing to exposed source regions of such material, perhaps in the area around Vasco da Gama Seamount or on the continental slope of Portugal. Winnowing and re-working by contour currents may have been responsible for the sharp tops to the sandstone beds. Soon after the beginning of the middle Eocene the turbidite sediments became finer grained, predominantly clay sized, and the typical turbidite/hemipelagite motif is of claystone overlying calcareous nannofossil claystone and nannofossil chalk. This may simply reflect the increasing distance to the turbidite sources, that is, the deposits became more distal, as the abyssal plain and continental rise sediments submerged the basement highs and caused the base of the continental slope to effectively 'retreat' landward. At the same time, the proportion of nannofossil claystone and nannofossil chalk decreased. The dip of the bedding decreases slightly upwards in the cored section, possibly indicating the effects of differential compaction between the flanks and crest of Hobby High.

Remarkable, but as yet unexplained, peaks in magnetic susceptibility and magnetic intensity occurred near the late Paleocene/early Eocene boundary. These peaks correlate with blebs of black material, possibly magnetite rich or containing iron-manganese nodules, in a dark brown claystone, and have been noticed at approximately, if not precisely, the same chronostratigraphic horizon at all southern Iberia Abyssal Plain sites that cored sediment of this age.

The claystones, calcareous claystones, and sandstones have systematically different physical properties. Densities and velocities lie in the ranges 1.95–2.15 g/cm^3 and 2.3–2.5 km/s, 2.2–2.4 g/cm^3 and 2.4–3.4 km/s, and 2.4–2.6 g/cm^3 and 3.4–5.3 km/s, respectively.

Conclusions

Many important conclusions about this site, such as answering the question whether the mafic rocks are the product of synrift or prerift partial melting of the upper mantle, will depend on the results of shore-based work, particularly geochronological dating. The principal conclusion, however, is that although differences in the early metamorphic evolution do exist between the three sites located on Hobby High (Sites 900, 1067, and 1068), the different lithologies are unlikely to be genetically divorced in origin. As the tectono-metamorphic evolution of the Site 900 metagabbro is clearly associated with the rifting event (high-temperature intense shear deformation that ended at 136 Ma, followed by a mainly static retrometamorphism and a late deformation in greenschist facies conditions), all these meta-igneous rocks may be products of synrift partial melting of the upper mantle that partly impregnated, and were intruded above, the peridotite. It is also salutary to recognize the amount of petrological heterogeneity that can exist within the ocean/continent transition, both laterally over a scale 1400 m (the distance between Sites 1068 and 1067) and vertically within a few tens of meters (as at Site 1067).

A second clear conclusion is that the upper H reflector is probably the crust/mantle boundary as it apparently separates peridotite (mantle rocks) from the overlying series of meta-igneous rocks cored at Sites 900, 1067, and 1068 (crustal rocks). The very intense ductile synrift shear deformation observed in the Site 900 metagabbro strongly suggests that this contact is tectonic. If dating of Site 1067 amphibolites confirms the synrift age of the mafic rocks overlying the H reflector, the Leg 173 samples offer the first opportunity to investigate the synrift crust/mantle boundary under a rift zone.

Lastly, the recovery of mantle rocks at Site 1068 within the ocean/continent transition demonstrates that mantle rocks outcrop only 25 km west of Site 1065, where basement is most probably made of continental crust. This indicates that mantle rocks were unroofed in the continental breakup zone very close to the landward edge of the ocean/continent transition, and that basement in the ocean/continent transition of the southern Iberia Abyssal Plain is made, at least sporadically, of mantle rocks over a width of at least 95 km at this latitude.

REFERENCES

Agrinier, P., Cornen, G., and Beslier, M.-O., 1996. Mineralogical and oxygen isotopic features of serpentinites recovered from the ocean/continent transition in the Iberia Abyssal Plain. *In* Whitmarsh, R.B., Sawyer, D.S., Klaus, A., and Masson, D.G. (Eds.), *Proc. ODP, Sci. Results,* 149: College Station, TX (Ocean Drilling Program), 541–552.

Berggren, W.A., Kent, D.V., Swisher, C.C., III, and Aubry, M.-P., 1995. A revised Cenozoic geochronology and chronostratigraphy. *In* Berggren, W.A., Kent, D.V., Aubry, M.-P., and Hardenbol, J. (Eds.), *Geochronology, Time Scales and Global Stratigraphic Correlation.* Spec. Publ.—Soc. Econ. Paleontol. Mineral., 54:129–212.

Beslier, M.-O., Cornen, G., and Girardeau, J., 1996. Tectono-metamorphic evolution of peridotites from the ocean/continent transition of the Iberia Abyssal Plain margin. *In* Whitmarsh, R.B., Sawyer, D.S., Klaus, A., and Masson, D.G. (Eds.), *Proc. ODP, Sci. Results,* 149: College Station, TX (Ocean Drilling Program), 397–412.

Cannat, M., Karson, J.A., Miller, D.J., et al., 1995. *Proc. ODP, Init. Repts.*, 153: College Station, TX (Ocean Drilling Program).

Charlou, J.-L., and Douval, J.-P., 1993. Hydrothermal methane venting between 12°N and 26°N along the mid-Atlantic ridge. *J. Geophys. Res.*, 98:9625–9642.

Comas, M.C., Sánchez-Gómez, M., Cornen, G., and de Kaenel, E., 1996. Serpentinized peridotite breccia and olistrostrome on basement highs of the Iberia Abyssal Plain: implications for tectonic margin evolution. *In* Whitmarsh, R.B., Sawyer, D.S., Klaus, A., and Masson, D.G. (Eds.), *Proc. ODP, Sci. Results,* 149: College Station, TX (Ocean Drilling Program), 577–591.

Cornen, G., Beslier, M.-O., and Girardeau, J., 1996a. Petrology of the mafic rocks cored in the Iberia Abyssal Plain. *In* Whitmarsh, R.B., Sawyer, D.S., Klaus, A., and Masson, D.G. (Eds.), *Proc. ODP, Sci. Results,* 149: College Station, TX (Ocean Drilling Program), 449–469.

————, 1996b. Petrologic characteristics of the ultramafic rocks from the ocean/continent transition in the Iberia Abyssal Plain. *In* Whitmarsh, R.B., Sawyer, D.S., Klaus, A., and Masson, D.G. (Eds.), *Proc. ODP, Sci. Results,* 149: College Station, TX (Ocean Drilling Program), 377–395.

de Kaenel, E., and Villa, G., 1996. Oligocene–Miocene calcareous nannofossils biostratigraphy and paleoecology from the Iberia Abyssal Plain. *In* Whitmarsh, R.B., Sawyer, D.S., Klaus, A., and Masson, D.G. (Eds.), *Proc. ODP, Sci. Results,* 149: College Station, TX (Ocean Drilling Program), 79–145.

Deer, W.A., Howie, R.A., and Zussman, J., 1982. *Zircon: Rock-forming Minerals* (Vol. 1A): *Orthosilicates* (2nd ed.): London (Longman), 412–442.

————, 1993. *Apatite: The Rock-forming Minerals* (3rd ed.): London (Longman), 663–669.

Galdeano, A., Moreau, M.G., Pozzi, J.P., Berthou, P.Y., and Malod, J.A., 1989. New paleomagnetic results from Cretaceous sediments near Lisboa (Portugal) and implications for the rotation of Iberia. *Earth Planet. Sci. Lett.*, 92:95–106.

Gibson, I.L., Milliken, K.L., and Morgan, J.K., 1996a. Serpentinite-breccia landslide deposits generated during crustal extension at the Iberia Margin. *In* Whitmarsh, R.B., Sawyer, D.S., Klaus, A., and Masson, D.G. (Eds.), *Proc. ODP, Sci. Results,* 149: College Station, TX (Ocean Drilling Program), 571–575.

Gibson, I.L., Beslier, M.-0., Cornau, G., Milliken, K.L., and Seifert, K.E., 1996b. Major- and trace-element seawater alteration profiles in serpentinite formed during the development of the Iberia margin, Site 897. *In* Whitmarsh, R.B., Sawyer, D.S., Klaus, A., and Masson, D.G. (Eds.), *Proc. ODP, Sci. Results,* 149: College Station, Texas (Ocean Drilling Program), 519–527.

Girardeau, J., and Gil-Ibarguchi, J.-I., 1991. Pyroxenite-rich peridotite of the Cabo Ortegal Complex (north western Spain): evidence for large scale upper mantle heterogeneity. *J. Petrol.*, 32:135–154.

Graham, J.W., 1949. The stability and significance of magnetism in sedimentary rock. *J. Geophys. Res.*, 54:131–167.

Krawczyk, C.M., Reston, T.J., Beslier, M.-O., and Boillot, G., 1996. Evidence for detachment tectonics on the Iberia Abyssal Plain rifted margin. *In* Whitmarsh, R.B., Sawyer, D.S., Klaus, A., and Masson, D.G. (Eds.), *Proc. ODP, Sci. Results*, 149: College Station, TX (Ocean Drilling Program), 603–615.

Martini, E., 1971. Standard Tertiary and Quaternary calcareous nannoplankton zonation. *In* Farinacci, A. (Ed.), *Proc. 2nd Int. Conf. Planktonic Microfossils Roma:* Rome (Ed. Tecnosci.), 2:739–785.

Milliken, K.L., Lynch, F.L., and Seifert, K.E., 1996. Marine weathering of serpentinites and serpentinite breccias, Site 897 and 899, Iberia Abyssal Plain. *In* Whitmarsh, R.B., Sawyer, D.S., Klaus, A., and Masson, D.G. (Eds.), *Proc. ODP, Sci. Results*, 149: College Station, TX (Ocean Drilling Program), 529–540.

Okada, H., and Bukry, D., 1980. Supplementary modification and introduction of code numbers to the low-latitude coccolith biostratigraphic zonation (Bukry, 1973; 1975). *Mar. Micropaleontol.*, 5:321–325.

Passchier, C.W., and Trouw, R.A.J., 1996. *Microtectonics:* Berlin (Springer-Verlag).

Perch-Nielsen, K., 1985. Mesozoic calcareous nannofossils. *In* Bolli, H.M., Saunders, J.B., and Perch-Nielsen, K. (Eds.), *Plankton Stratigraphy:* Cambridge (Cambridge Univ. Press), 329–426.

Pickering, K.T., Hiscott, R., and Hein, F.J., 1989. *Deep-marine Environments: Clastic Sedimentation and Tectonics:* London (Unwin Hyman).

Pospichal, J.J., and Wise, S.W., Jr., 1990. Calcareous nannofossils across the K/T boundary, ODP Hole 690C, Maud Rise, Weddell Sea. *In* Barker, P.F., Kennett, J.P., et al., *Proc. ODP, Sci. Results*, 113: College Station, TX (Ocean Drilling Program), 515–532.

Ramdohr, P., 1980. *The Ore Minerals and their Intergrowths* (2nd ed.): New York (Pergamon).

Ringwood, A.E., 1977. Petrogenesis in island arc systems. *In* Talwani, M., and Pitman, W.C. (Eds.), *Island Arcs, Deep Sea Trenches and Back-Arc Basins.* Am. Geophys. Union, Maurice Ewing Ser., 1:311–324.

Robinson, P.T., Von Herzen, R., et al., 1989. *Proc. ODP, Init. Repts.*, 118: College Station, TX (Ocean Drilling Program).

Rothwell, R.G., 1989. *Minerals and Mineraloids in Marine Sediments: An Optical Identification Guide:* Basking, UK (Elsevier Appl. Sci. Publ.).

Sammis, C.G., Osborne, R.H., Anderson, J.L., Banerdt, M., and White, P., 1986. Self-similar cataclasis in the formation of fault gouge. *Pure Appl. Geophys.*, 124:55–77.

Sawyer, D.S., Whitmarsh, R.B., Klaus, A., et al., 1994. *Proc. ODP, Init. Repts.*, 149: College Station, TX (Ocean Drilling Program).

Schärer, U., Kornprobst, J., Beslier, M.O., Boillot, G., and Girardeau, J., 1995. Gabbro and related rock emplacement beneath rifting continental crust: U-Pb geochronological and geochemical constraints for the Galicia passive margin (Spain). *Earth Planet. Sci. Lett.*, 130:187–200.

Seifert, K., and Brunotte, D., 1996. Geochemistry of serpentinized mantle peridotite from Site 897 in the Iberia Abyssal Plain. *In* Whitmarsh, R.B., Sawyer, D.S., Klaus, A., and Masson, D.G. (Eds.), *Proc. ODP, Sci. Results*, 149: College Station, TX (Ocean Drilling Program), 413–424.

Seifert, K., Gibson, I., Weis, D., and Brunotte, D., 1996. Geochemistry of metamorphosed cumulate gabbros from Hole 900A, Iberia Abyssal Plain. *In* Whitmarsh, R.B., Sawyer, D.S., Klaus, A., and Masson, D.G. (Eds.), *Proc. ODP, Sci. Results*, 149: College Station, TX (Ocean Drilling Program), 471–488.

Shipboard Scientific Party, 1994a. Site 897. *In* Sawyer, D.S., Whitmarsh, R.B., Klaus, A., et al., *Proc. ODP, Init. Repts.*, 149: College Station, TX (Ocean Drilling Program), 41–113.

————, 1994b. Site 899. *In* Sawyer, D.S., Whitmarsh, R.B., Klaus, A., et al., *Proc. ODP, Init. Repts.*, 149: College Station, TX (Ocean Drilling Program), 147–209.

————, 1994c. Site 900. *In* Sawyer, D.S., Whitmarsh, R.B., Klaus, A., et al., *Proc. ODP, Init. Repts.*, 149: College Station, TX (Ocean Drilling Program), 211–262.

————, 1994d. Site 901. *In* Sawyer, D.S., Whitmarsh, R.B., Klaus, A., et al., *Proc. ODP, Init. Repts.*, 149: College Station, TX (Ocean Drilling Program), 263–268.

Stow, D.A.V., 1994. Deep sea processes of sediment transport and deposition. *In* Pye, K. (Ed.), *Sediment Transport and Depositional Processes:* London (Blackwell), 257–291.

Van der Voo, R., 1969. Paleomagnetic evidence for the rotation of the Iberia peninsula. *Tectonophysics*, 7:5–56.

Wyllie, M.R.J., Gregory, A.R., and Gardner, L.W., 1956. Elastic wave velocities in heterogeneous and porous media. *Geophysics*, 21:41–70.

Ms 173IR-106

Prior Chapter Contents Next Chapter